The impact of transient mitigation schemes on the MAST edge plasma

Andrew Thornton

Thesis submitted for the award of Doctor of Philosophy

University of York

Department of Physics

January 2011

Supervised by;

Dr. K.J. Gibson
Department of Physics, University of York, Heslington, York, YO10 5DD

Dr. A. Kirk
Culham Centre for Fusion Energy (CCFE), Culham Science Centre, Abingdon, Oxon, OX14 3DB

Abstract

A disruption is the sudden and uncontrolled loss of plasma confinement in a tokamak. Disruptions on the Mega Amp Spherical Tokamak (MAST) are characterised in terms of thermal quench timescales, energy balance and pre disruption energy loss. Analysis of the energy balance during disruptions on MAST has shown that approximately 10% of the stored energy is radiated during a disruption and 80% is deposited onto the divertor. The energy loss prior to the thermal quench is found to be 50% of the maximum energy in the plasma, which is half the value assumed for the ITER design.

Disruptions occur when operational boundaries, in terms of current, pressure and density, are exceeded. An analysis of the operational boundaries in MAST shows that the frequency of disruptive events increases as the density is raised to 1.5 times the Greenwald density limit and that the pressure limit is consistent with empirical scalings. The current limit on MAST is triggered before the expected value of q_{95} is reached. Further analysis of the disrupting discharges in MAST shows that there is substantial energy loss prior to the thermal quench of up to 50%, however, disruptions at full performance are frequent.

Disruption mitigation on MAST, via massive gas injection, has been performed using 0.32 bar litres ($7.7\text{x}10^{21}$ particles, 10 times the plasma inventory) of a 90% helium and 10% argon mixture. The evolution of the plasma during mitigation is followed using high speed (up to 50kHz) imaging and high temporal (0.2ms) resolution Thomson scattering. High speed imaging of the plasma shows that the neutral impurities are confined to the plasma periphery. Impurity ions penetrate to the q=2 surface and mix with the bulk plasma during the thermal quench. Thomson scattering data shows significant (double the initial core density) build of density on rational surfaces, specifically q=2, prior to the thermal quench.

Analysis of the power load to the divertor during mitigated disruptions shows reductions of 60% in peak power loadings compared to unmitigated. The energy balance during mitigated disruptions shows an increase in the radiated energy to 40% of the total stored energy and a decrease in the energy to the divertor of 40%. The effect of mitigation is to increase the current quench time and decrease the magnitude of halo currents by 80%.

Contents

List of Figures

List of Tables

Acknowledgements

Firstly, I would like to thank Kieran Gibson, for directing me along the path that lead to the production of this thesis and for his supervision during it. Steve Lisgo, Richard Martin and Andrew Kirk have also been a great source of assistance with the DMV installation, experiments and supervision during my time at Culham and York. James Harrison has been a source of constant help and good humour for the last three years or so. During my time at York, Tom Hayward was invaluable for computing help and for a second opinion.

I am grateful for the assistance of all those involved in the DMV installation, especially Andy Cullen who looked after the vacuum and installation which took a great deal off my mind during the final few months.

Finally, I would like to say thank you to my parents for their support and encouragement throughout.

Declaration

I declare that the work presented in this thesis, other than contributions cited or acknowledged in the text, is my own.

Andrew Thornton, January 2011.

Chapter 1

Introduction

The production of energy via fusion is a key means of satisfying the energy needs of the future. In order to produce energy from fusion it is necessary to confine the plasma for long enough to allow the fusion reaction to take place. The confinement is achieved by using magnetic fields, in a device known as a tokamak.

In certain circumstances, the confinement of the plasma in a tokamak can be lost. The sudden and uncontrolled loss of plasma confinement, which is known as a disruption, produces significant heat fluxes and structural stresses on the components inside the tokamak. Disruptions occur as a result of exceeding certain operational boundaries which are defined in terms of the current, density and pressure of the plasma being confined.

The mitigation of a disruptions can be achieved using massive gas injection. Massive gas injection involves the injection of approximately 10 to 100 times the plasma inventory of neutral gas into the vacuum vessel. The neutral gas then acts to radiate away the energy stored in the plasma, bringing about a controlled termination. Several issues must be addressed before massive gas injection can be used on the next generation of tokamaks such as ITER and DEMO. The issues to be addressed include the plasma evolution, in terms of density and temperature, after massive gas injection. At present, few tokamaks are equipped with diagnostics to measure the evolution of the temperature and density with sufficient temporal and spatial resolution to understand the processes occuring during mitigation. The Mega Ampere Spherical Tokamak (MAST) is ideally suited to disruption studies as a result of the excellent imaging and diagnostic access. The world leading Thomson scattering system and high speed imaging on MAST enable the penetration and mixing of the impurities injected during massive gas injection to be followed with unprecedented detail. This level of detail allows the extraction of the key physical processes at work during a mitigation event, such as vessel surface heat load reduction, energy balance and density profile evolution. The knowledge obtained can then be used to extrapolate the requirements of an ITER massive gas injection scheme.

Secondly, the effect of mitigation on the heat loads and vessel forces delivered to the vessel components must be monitored and assessed. All present day experiments are concerned with mitigation in conventional tokamaks, in the future compact tokamaks, known as spherical tokamaks (such as MAST), may be used as the basis of a component testing facility. It is therefore important to understand the effect of mitigation in present day spherical tokamaks. These questions and areas of study form the basis of this work.

1.1 Nuclear Fusion

The production of energy from nuclear fission relies on the breaking up of heavier nuclei into lighter, more stable ones. The energy released comes in the form of increased binding energy which is manifest in a difference in the masses of the constituent parts when compared to whole nuclei. The process of nuclear fission is driven by the decay of elements down in mass to approach iron. However, it is also possible for energy to be released by combining elements to form heavier elements. It is this process that is known as nuclear fusion. The release of energy by nuclear fusion is demonstrated everyday at sunrise, as it is the process by which the Sun produces its energy. The Sun uses the fusion of hydrogen to helium by using deuterium as an intermediary [1].

The fusion of two isotopes of hydrogen, deuterium (D) and tritium (T), is as follows [1];

$$^{2}_{1}D +^{3}_{1} T \rightarrow^{4}_{2} He[3.5MeV] +^{1}_{0} n[14.1MeV] \tag{1.1}$$

The fusion of deuterium and tritium is a favourable reaction in terms of cross section and energy released when compared to the reactions which take place on the Sun, hence the use of this reaction for fusion power. The 17.6 MeV released by this reaction is carried in the form of kinetic energy by the reaction products. The released kinetic energy can be used to both heat the deuterium and tritium (via the alpha particle), thereby sustaining the reaction, and to provide a source of heat for generating steam (via the neutron). In addition, the capture of the neutron released from the reaction by lithium can be used to generate tritium, which can then be separated and used as fuel. In order for fusion to take place, the Coulomb repulsion between the two reacting nuclei must be overcome. The cross section for fusion reactions reaches acceptable values ($\approx 10^{-21}\mathrm{m}^3\mathrm{s}^{-1}$) when the temperature of the reactants exceeds 10 keV. Matter at these temperatures breaks down to form a plasma, which consists of free ions and electrons. Due to the high temperatures required for fusion, a suitable means of containing the plasma for long enough for them to react must be found.

1.2 Tokamaks

In order for fusion to occur, the high temperature fusion plasma must be confined. The temperatures required for fusion mean that any material that comes into contact with the plasma will be destroyed. As has been previously discussed, the solution to confining a plasma is to used magnetic fields and the leading type of magnetic confinement fusion (MCF) device is the tokamak. At present, the largest tokamak in operation is the Joint European Torus (JET) located at the Culham Centre for Fusion Energy in Oxfordshire. The next generation of tokamak, ITER, is presently under construction in Cadarache, France and it is expected that first plasma operation will occur in 2018. The two devices are on significantly different scales, with ITER being around twice as large as JET in terms of radius, but the basic operation of both devices is the same. The tokamak uses a combination of magnetic fields to confine a plasma against the effects of plasma pressure and particle drifts.

The tokamak consists of a torus shaped vacuum vessel which is surrounded by magnetic field coils. Through the centre of the torus there is a solenoid as shown in figure 1.1. The geometry of the tokamak is described using the toroidal and poloidal directions. The toroidal direction is around the torus in the x-z plane and the poloidal direction is the location around a cross section of one half of the torus in the x-y plane.

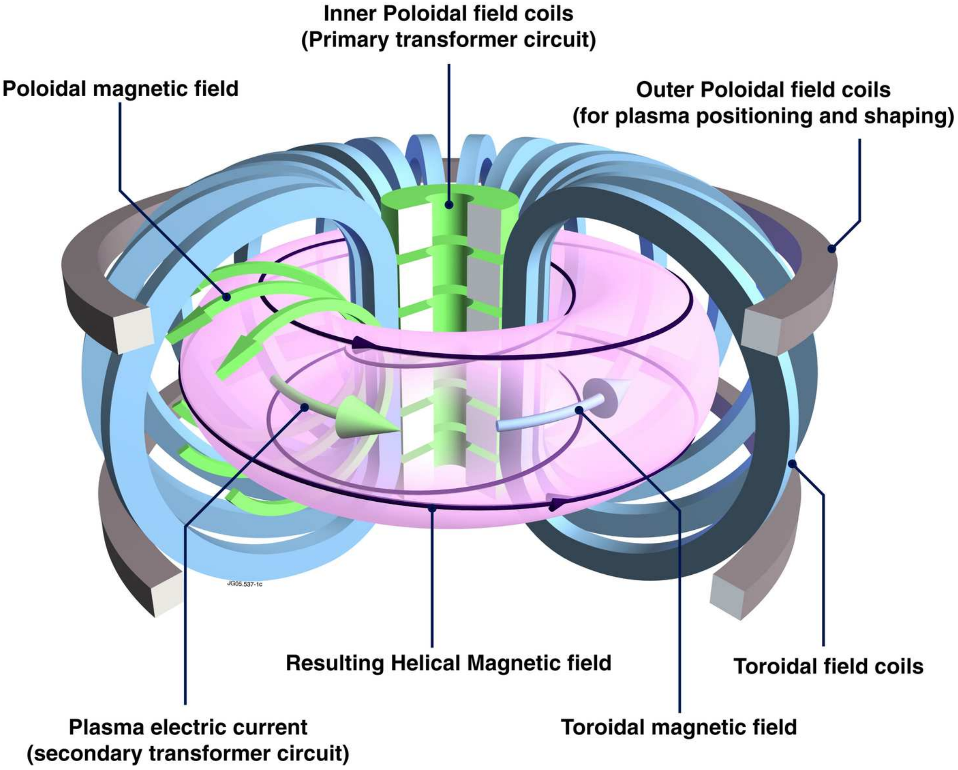

Figure 1.1: The tokamak [2]

1.2.1 Equilbrium

The production of an equilibrium in which the plasma is confined requires a combination of magnetic fields. Figure 1.1 illustrates the magnetic field coils, magnetic fields and currents that are required to confine a fusion plasma. The strongest magnetic field used is the toroidal field, which is generated by the toroidal magnetic field coils located outside the vacuum vessel. The simplest form of magnetic confinement on closed field lines would be a device where there is only a toroidal magnetic field. Indeed, such devices were originally constructed and were known as toroidal pinches [3]. These devices were prone to a type of plasma instability known as a kink mode, a large scale instability which results in a loss of confinement. The toroidal magnetic field coils of the tokamak are spaced closer together on the inside of the torus when compared with the outside, which causes the magnetic field strength to vary across the tokamak. The combination of the curvature and gradient in the magnetic field produce a drift of particles which acts in opposite directions for ions and electrons. The result of this drift is to cause charge separation between the ions and electrons across the top and bottom of the tokamak. The resulting electric field then combines with the toroidal field that is externally produced to cause the plasma to drift radially outward due to ExB drift and out of confinement [4, 5, 6]. The solution to this problem, is to connect the top and the bottom of the torus together with the magnetic field, thereby preventing the separation of charge. To connect the top and bottom of the tokamak together, the field lines must be twisted around the torus. The twisting of the field lines is produced by driving a current through the plasma using transformer action. The poloidal magnetic field generated by the plasma current causes the magnetic field lines to orbit the tokamak in a helical path which eliminates the charge separation [3, 6].

The ratio between the poloidal and toroidal magnetic field strengths determines the number of times a given field lines travels toroidally before returning to a given poloidal starting point. The ratio is defined using the safety factor, q, which can be defined as the number of toroidal revolutions (m) to poloidal revolutions (n), or approximated using physical values. The definitions are shown in equation 1.2. The symbols are defined as follows, a, is the minor radius, R is the major radius (see figure 1.2), B_ϕ is the toroidal magnetic field and B_θ is the poloidal magnetic field [6, 7].

$$q = \frac{m}{n} \approx \frac{aB_\phi}{RB_\theta} \tag{1.2}$$

The value of q varies across the minor radius of the plasma, with the lowest values of q occurring on the magnetic axis of the tokamak where the plasma current, and hence B_θ is the largest. The value of q increases as the minor radius increases. The safety factor is named due to the constraints it places on plasma stability, with higher values producing greater stability. There exist certain regions where the value

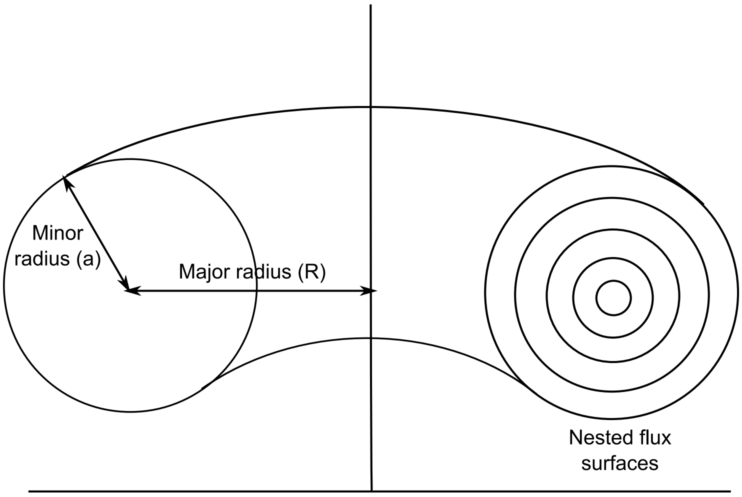

Figure 1.2: Major and minor radii in a tokamak and nested flux surfaces

of q is rational, in these regions the field lines meet with themselves after n toroidal rotations. Rational surfaces with low q values (such as 1, 3/2 or 2) play a large role in determining the stability of the plasma [6].

Force balance

The magnetic field in a tokamak confines the plasma against the plasma pressure. The force balance between the magnetic field, driven currents and the pressure gradient can be found, to first order, by considering the conservation of momentum in the system [8]. The resulting simplified, steady state expression, found by examining the forces acting on the system and seeking a time independent result, is shown in equation 1.3. The expression links together the magnetic field, $\vec{B}$, the current, $\vec{j}$ and the plasma pressure, P.

$$\vec{j} \wedge \vec{B} = \nabla P \tag{1.3}$$

The implications of equation 1.3 are that there is no current or magnetic field in the direction of the pressure gradient. To prove this, simply take the dot product of 1.3 with $\vec{j}$ and $\vec{B}$ the result of this is to yield the two equations, $\vec{j} \cdot \vec{\nabla} P = 0$ and $\vec{B} \cdot \vec{\nabla} P = 0$. The equilibrium of a tokamak is therefore constructed of a series of toroidally symmetric nested surfaces, known as flux surface, upon which, $\vec{B}$, pressure, q and current are constant. These flux surfaces can be seen in figure 1.2 [6, 7, 8].

By confining a plasma, which has a given pressure, with a magnetic field gives rise to a limit of tokamak confinement. Associated with a magnetic field is a magnetic field pressure, it is this magnetic field pressure that balances the plasma pressure. It is clear that in a situation where the plasma pressure exceeds the magnetic pressure, there can no longer be confinement of the plasma. A measure of how far the plasma pressure is from matching the magnetic field pressure can be expressed as a beta (β)

value, which is simply the plasma pressure divided by the magnetic pressure. The formula for beta is shown in equation 1.4, where μ_0 is the permittivity of free space and the remaining symbols are as previously defined. The value of beta is often quoted as a percentage. Although from these basic considerations, a beta of 100% is possible, in reality, other instabilties place constraints on the maximum beta that can be obtained (see section 1.3) [5, 6].

$$\beta = \frac{P}{B^2/2\mu_0} \tag{1.4}$$

The beta limit, which will be discussed later, (chapter 2.1) is a fundamental operational constraint in a tokamak, exceeding it leads to a sudden, uncontrolled loss of confinement. Exceeding this, or any other operational boundary in a tokamak will produce a loss of confinement, which is known as a disruption. Disruptions, their effects and mitigation form the major part of this thesis and will be discussed at length in the following sections and chapters.

Despite the hazards of operation at high beta, it is highly desirable to operate a tokamak at high beta. The reason for this is that the fusion reaction rate varies directly with both density and temperature, i.e. the pressure of the plasma. The main cost of running a fusion reactor arises from the need to generate the toroidal and vertical fields which provide the magnetic pressure for confinement. Hence, the plasma beta can be considered to be inversely proportional to cost, and the ideal case is to confine the greatest plasma pressure with the least magnetic field, i.e. high beta operation.

1.2.2 Power handling

The confined plasma will fill the vacuum vessel in which it is placed. Some particles will follow closed field lines, which do not intersect with material surfaces and some will follow open field lines, which do intersect with surfaces. The diffusion of particles across the magnetic field due to collisions allows particles on closed field lines to move to open field lines. The interaction between the plasma and the vessel walls must be controlled to prevent the build up of high atomic number (Z) impurities. The high Z (such as iron, or nickel) impurities produce large quantities of line radiation, thereby cooling the plasma and limiting performance. There are two main ways in which the interaction between the plasma and the wall can be controlled. These two methods are the use of a limiter or the use of a divertor.

Limiters simply consist of a toroidally or poloidally symmetric ring which protrudes from the vacuum vessel wall. The plasma hits this material first, which can be made of a low Z impurity (such as carbon), thereby limiting the interaction of the plasma with the vessel wall. The limiter is the simplest solution to prevent plasma wall interactions, however, it is not considered as a solution for future devices due to the fact that the contact area between the plasma and the limiter is small. The

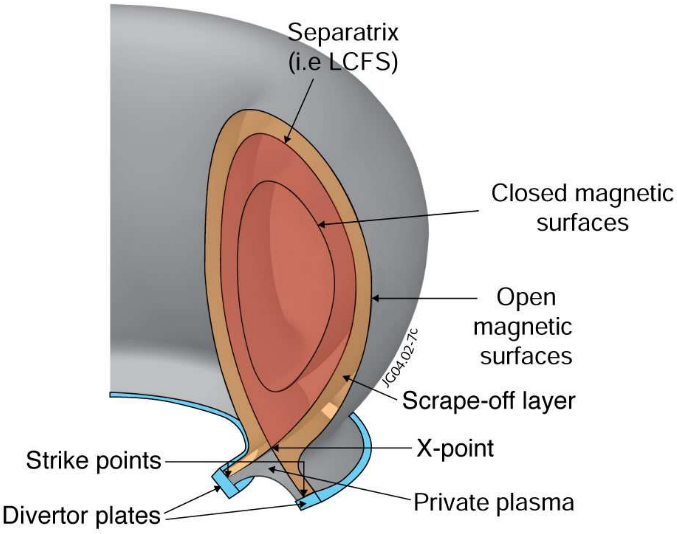

Figure 1.3: A divertor [2]

small contact patch gives rise to significant heat loads to the limiter, which erodes away the material. The divertor is the present solution to controlling the plasma wall interaction, as it produces several other advantages which will be outlined next [7, 9].

Divertors

A tokamak divertor can be formed either toroidally or poloidally around the machine, however, the typical configuration is for a poloidal divertor which is illustrated in figure 1.3. A divertor is formed by driving a current around the torus in the same direction as the plasma current in an external coil. The effect of this is to generate a null in the poloidal magnetic field which is known as the X point. Field lines which pass through the X point are located on a surface known as the separatrix, or last closed flux surface (LCFS). The separatrix marks the change between open and closed magnetic surfaces, with regions outside of the separatrix following open field lines which interact with the divertor targets and those on the inside being closed. The interaction point between the field line and the target is known as the strike point and the region outside the separatrix is known as the scrape off layer (SOL).

Particles move along field lines rapidly when they move parallel to the magnetic field, this is known as parallel transport. The formation of an X point creates a very low poloidal field which causes the field lines on the separatrix to loop around it many times before interacting with the divertor targets. The divertor increases the along field line distance between the material surfaces and the core plasma region. The effect of this is to minimise the contact of the high temperature core plasma from the region where the plasma interacts with material surfaces [6, 9]. The use of a divertor also provides additional benefits. One of these benefits is a mechanism for

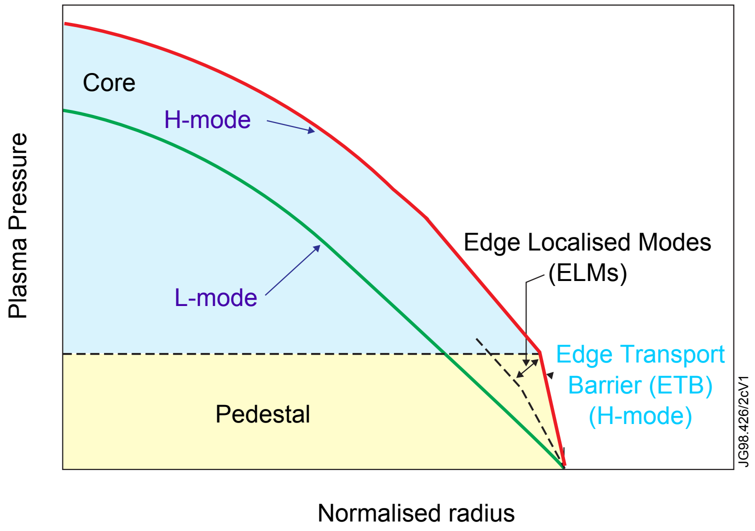

Figure 1.4: Plasma pressure profiles for H mode and L mode [Image courtesy EFDA-JET]

the removal of helium, a product of DT fusion, from the plasma. If the helium is not removed once it has thermalised with the plasma then it contributes an impurity source and limits performance. Also the heat exhaust from the plasma can be controlled by directing it onto the divertor targets. The strike point region can be broadened to further decrease the heat loads on the targets by modifying B_θ to allow expansion of the divertor legs [9, 10]. Perhaps the most important effect of the divertor is the access to operational regimes with improved confinement [9].

The improved confinement regime is known as H mode and was first reported in the ASDEX tokamak [11]. In order for a transition into H mode from the standard operating mode (L mode), sufficient auxiliary heating power must be applied. The heating power can be provided from a variety of means but the main type of external plasma heating is the injection of neutral particles, which is known as neutral beam injection (NBI). Entry into H mode will occur at a given threshold of power crossing the SOL and varies from machine to machine. The existence of H mode can be seen experimentally by decreased emission (D_α) from the plasma edge. The effect of H mode on tokamak performance is to increase the temperature and density of the confined plasma, which can be seen in figure 1.4, through the doubling of the confinement time [6, 9].

1.3 Spherical Tokamaks (STs)

The beta limit in a tokamak is set by a specific type of plasma instability, known as a kink mode [6], which occurs when excessive current is driven through the plasma. A simple description of kink mode is where the plasma deviates from a circle toroidally, and folds in on itself. The origin of the kink mode is the evolution of the current distribution in the plasma, known as the current profile. The plasma is unstable to kink modes when the value of q at the plasma edge falls to 2. The limit set by the kink mode to tokamak stability was calculated by Sykes and Troyon [12, 13]. The limit can be defined in equation 1.5 where the symbols are defined as follows; β_T is the toroidal beta, I_p is the plasma current (in mega Amperes), a is the minor radius and B_T is the toroidal magnetic field strength [6, 14].

$$\beta_T \leq 3.5 \frac{I_p}{aB_T} \tag{1.5}$$

It is possible to write equation 1.5 in a different form using the definition of q at the plasma edge (q_a) [6, 7, 14]. By using the definition of the beta limit using the value of q it is found that $\beta \propto \frac{1}{Aq_a}$, where A is the aspect ratio of the plasma. The aspect ratio of a tokamak is the ratio between the major radius, R and the minor radius (a). Therefore, the beta limit can be increased by decreasing the aspect ratio. Tokamaks, such as JET, have aspect ratios of around 3. Spherical tokamaks by contrast have significantly lower aspect ratios of between 1.2 and 1.3.

The effect of the low aspect ratio is shown in figure 1.5, it is clear that the spherical tokamak (ST) is a much more compact device when compared to a conventional tokamak. The design for an ST was first put forward by Peng [15]. There are several advantages, other than high beta operation to STs. Firstly, as result of the improved beta limit, the required toroidal field to confine a given plasma (to maintain edge $q > 2$) is lower than that required on a conventional tokamak, resulting in STs having poloidal magnetic fields that are comparable to conventional tokamaks and toroidal fields that are lower in strength. In addition, the variation of the toroidal magnetic field across the plasma radius is larger than in a conventional tokamak due to the smaller major radii of STs and the $1/R$ dependence of the magnetic field strength. The ratio of the poloidal and toroidal field give the angle between the x-z plane and the magnetic field line, in a conventional tokamak this does not vary significantly over the length of a field line. However, this is not the case on an ST, where the pitch angle on the outer side (outboard side) of the tokamak being steeper than that on the inside. The effect of the shallow inboard pitch angle is to cause confined particles to spend more time on the inboard side of the tokamak. The inboard side of the tokamak has the centrifugal force acting against the pressure gradient, this region is known as a good curvature region, as the configuration is stabilising. The outboard side is known as a region of bad curvature, here the pressure gradient and the centrifugal force on the particles act to move the particles out of confinement [14]. The varying field line pitch also acts to increase the edge q value making the ST particularly stable [5]. The disadvantages of STs arise from their compact size. For example the area over which the heat flux is deposited is proportional to the radius of the tokamak. The small radius of the centre column provides a small area over which the power from the inner divertor leg is deposited, leading to high heat fluxes in power plant scale STs. In addition, the compact design provides limited space for shielding around the centre column to protect against neutron damage

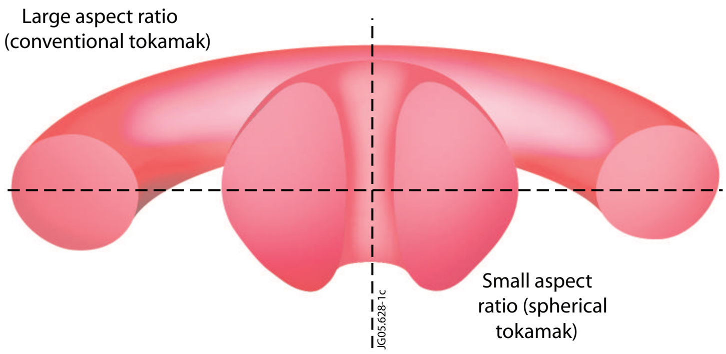

Figure 1.5: Conventional and spherical tokamak comparison [2]

when the ST concept is extended to a power plant scale machine.

There are several other inherent advantages of the ST, including natural elongation and high bootstrap fraction, which are too numerous to discuss here. A full treatment can be found in [14] and [16].

The first ST, the Small Tight Aspect Ratio Tokamak (START), was built at Culham in the 1990s. START operated until 1999 and prior to decommissioning in 1999 set a record beta of 40% [17]. Following the sucess of START, a new spherical tokamak was constructed at Culham called the Mega Ampere Spherical Tokamak (MAST), which has been operating since 1999, and will be the tokamak upon which this work is based (see chapter 3).

1.4 Transient Events

There are several challenges that must be resolved before commercial energy generation from fusion can be a reality. The current focus of tokamak research is concentrated on these areas in order to refine and finalise the design for ITER, which is presently under construction. A detailed account of the design goals of ITER, specification and an overview of the present status of research can be found in [18].

A key area of research is the study of transient events which are short lived events that have to capability to generate large heat loads and vessel forces. Transient events in tokamaks include sawteeth, Edge Localised Modes (ELMs) [19] and disruptions. Recently, methods of mitigating ELMs have been developed [20, 21]. Disruptions and their mitigation for the basis of this thesis, and the following section will present an overview of this type of transient event [22].

1.4.1 Disruptions

A disruption in a tokamak is a sudden, uncontrolled loss of plasma confinement. The causes of disruptions are many and varied, often consisting of a sequence of events, such as increased density, mode growth or plant failures, which ultimately lead to a disruption. A detailed literature study of disruptions and their mitigation will follow in chapter 2, what follows here will be an introduction to this chapter.

The main motivation for studying disruptions and their mitigation is the damaging effect they can have on tokamak components. The loss of confinement during a disruption causes all of the energy stored in the plasma, both thermal and magnetic, to be lost. Typically, the energy is deposited onto the divertor and first wall of the tokamak which can lead to high energy fluxes on these surfaces which could lead to melting or vapourisation. The magnitude of the heat fluxes and a comparison to the melting/vapourisation onset of the divertor material on ITER can be made using the convention defined in [23] of the power divided by a product of the divertor wetted area and the timescale over which the energy is deposited. The expected energy load for ITER is between 144 MJ m^{-2} $\mathrm{s}^{-0.5}$ and 446 MJ m^{-2} $\mathrm{s}^{-0.5}$ ([23], table 6) depending on the actual duration of the energy deposition. The limits for melting or vapourisation for the various divertor and first wall materials are significantly lower than this; for carbon and tungsten the limit is 40-60 MJ m^{-2} $\mathrm{s}^{-0.5}$ ([23], table 5) and beryllium is 15 MJ m^{-2} $\mathrm{s}^{-0.5}$ [23]. The stored energy in a tokamak plasma has been seen to scale as R^5 [24], where R is the major plasma radius. It is clear from this scaling, that the divertor energy loading on DEMO and future commercial reactors will pose a significant challenge.

The loss of confinement leads to a rapid loss of the plasma current. The rapid current quench causes currents to be induced in the vacuum vessel of the tokamak. The interaction of these currents and the toroidal magnetic field (which is externally generated, and as a result does not change) produces large forces which act on the vacuum vessel. In addition to inducing current in the tokamak vessel, if there is contact between the plasma and the vessel walls, then the current flowing in the plasma will complete via the conducting vessel walls. The currents flowing in the walls, known as halo currents, interact with the toroidal field and give rise to structural stresses. The speed of the current quench in ITER [23] is projected to be 35 milliseconds, giving quench rates in excess of 400 $\mathrm{MA}^{-2}\mathrm{s}^{-1}$ for a plasma current of 15 MA.

Finally, the rapid current quench generates a large electromotive force which can act to accelerate electrons in the plasma to relativistic energies [25]. These high energy electrons, known as runaway electrons, can lead to the production of X-rays when the runaway electron (RE) beam interacts with components inside the tokamak. These X-rays can damage radiation sensitive diagnostics, in addition to the localised heating damage produced by the interaction of the RE beam and the tokamak. In ITER [23] it is projected that around 70% of the initial plasma current could be converted into REs, this would amount to a runaway electron current of around 11 MA.

1.5 Motiviation for study

The consequences of disruptions in the next generation of tokamaks are severe, the consequences of a disruption in a power plant tokamak would be catastrophic. Clearly, a means of mitigating a disruption is required which can ameliorate the damaging effects. One such method is the injection of a large quantity (approximately 10-100 times the original plasma inventory, see chapter 2) of neutral particles, typically high Z noble gases are used due their ability to radiate away energy via line radiation. The injection of the impurity gas causes to the stored energy to be radiated away, decreasing the heat loads to the targets and terminating the plasma prior to the generation of REs or halo currents.

The purpose of this thesis is to study disruptions and their mitigation by addressing the following points;

Determine the operational space of MAST. Disruptions occur at the boundary of operational space. Previous disruptions in MAST can be used to locate the density limit, q limit and beta limit.

Characterise unmitigated disruptions. The timescales of energy loss from disruptions can be determined from past discharges. The timescales can be compared to data from other machines, and ITER scalings. The energy balance between radiation and transport to the divertor can be determined, allowing comparison with mitigated disruptions.

Install a disruption mitigation system on MAST. Disruption mitigation via massive gas injection (MGI) has been performed on several machines (see chapter 2 for details). Mitigation via massive gas injection requires a suitable system to deliver impurities to the plasma on millisecond timescales.

Perform disruption mitigation experiments. MGI is the leading method of mitigating disruptions in ITER. MAST is equipped with a range of diagnostics which can assess the impact of mitigation on disruptions.

Study impurity penetration. The open design of MAST allows excellent imaging access compared to other tokamaks. The ability to image the whole plasma presents a unique opportunity to follow the mixing and penetration of the injected impurities.

Profile evolution during mitigation. Plasma temperature and density profiles evolve during mitigation. MAST is fitted with a high temporal and spatial resolution Thomson scattering system which can be used to follow the mixing of the impurities with the bulk plasma.

Study the effect of MGI on disruptions. The characteristics of mitigated disruptions can be compared with unmitigated disruptions. The comparison allows the impact of massive gas injection to be evaluated. The characterisation will include studies of the energy balance during disruptions, made possible by divertor heat flux measurements using infra red thermography covering all four strike points.

1.6 Thesis Outline

The purpose of this thesis is to study the effects of disruption mitigation in the MAST spherical tokamak. Chapter 1 has introduced some the concepts of the tokamak which will be used later and outlined some of the main features of disruptions and their effects on tokamak operation. Chapter 2 will build on the introduction to disruptions presented in chapter 1, it will contain a comprehensive literature study of disruptions and their mitigation which will outline the physics behind the following chapters. The MAST tokamak based at the Culham Centre for Fusion Energy (CCFE) is the tokamak on which this work will be based. Chapter 3 will outline the parameters and diagnostics that will be used for subsequent study of disruptions and disruption mitigation on MAST. There is a database of past MAST discharges, some of which have terminated in a disruption, the characteristics of these disruptive discharges will be analysed in chapter 4. The analysis of natural disruptions in MAST will allow the effects of disruption mitigation to be determined. Chapter 5 will detail the disruption mitigation valve (DMV) system on MAST which is used to produce controlled terminations of the MAST plasma. Chapters 6 and 7 will give the results of disruption mitigation on MAST, drawing information from the many diagnostics on MAST which have been detailed in chapter 3. Finally, chapter 8 will conclude the thesis and provide details of further work.

Chapter 2

Disruptions and Disruption Mitigation

This chapter will review the current state of knowledge on disruptions, which will allowing an assessment of the consequences of a disruption in future devices and highlight the areas which a disruption mitigation scheme must address.

2.1 Operational limits

The operational domain of a tokamak is bounded by three major limits. The most severe consequence of exceeding these limits is a total loss of confinement. The loss of confinement leads to the deposition of the whole stored plasma energy, both in terms of thermal and magnetic energy, onto the divertor and first wall of the tokamak in timescales of a few milliseconds. It is this rapid and uncontrolled loss of confinement that is known as a disruption.

The operational limits are the density limit [26], the low q limit [6] and the beta limit [27]. These boundaries have been identified experimentally by plotting the operating space of a tokamak in terms of major parameters and noting the regions in which the discharges begin to disrupt.

The most common method of illustrating the operational boundaries of a tokamak is the use of a Murakami-Hugill diagram [28] which shows the low q limit and the density limit. The general form of the disruptive boundary in a Hugill diagram is shown in figure 2.1. The boundary represented at $1/q_a = 0.5$ is the low q limit which arises due to current driven instabilities in the plasma. The plasma becomes unstable when the current profile steepens around the q=2 surface, the instability gives rise to the formation of an external kink mode. A kink mode is a type of plasma instability that causes the whole plasma boundary to deform which ultimately leads to a disruption. The production of a steep current gradient near the q=2 surface can be brought about by redistribution of the current flowing in the tokamak. The current profile is generally peaked in the centre, however, an internal kink mode becomes unstable when the value of q on axis falls below 1. The internal mode, known as a sawtooth, has the effect of fixing the maximum amount of current that can flow at the plasma centre. The result of driving additional current in a sawtoothing plasma is to cause the current to flow off centre and create a hollow current profile. The current flowing off centre gives rise to a steepening of the current profile around the q=2 surface, thereby destabilising it [6].

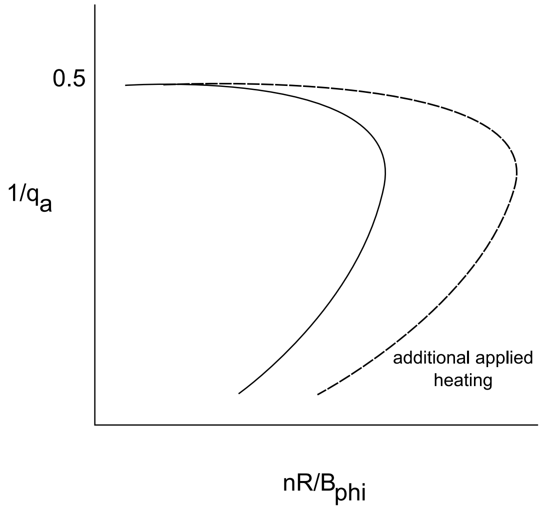

Figure 2.1: A schematic Hugill diagram for a tokamak showing the low q limit which runs horizontally across the plot and the density limit which can be extended with additional heating power. The quantity plotted along the abscissa is also known as the Murakami number.

The density limit arises from the cooling of the outer plasma regions as a result of the high density of gas at the plasma edge. The cooling of the plasma edge leads to the contraction and steepening of the current profile around the q=2 surface [6, 26, 29]. The process begins to runaway, as cooling of the plasma increases the density further until the plasma collapses.

It must be noted that the density limit is dependent on the amount of power available from additional heating. Discharges with additional heating power are able to sustain higher densities than those without. This is due to the high edge temperatures present which act to delay the onset of the edge cooling [7]. The empirically derived Greenwald limit for a tokamak without additional heating (ohmic) can be expressed by the formula $\bar{n}(10^{20}\mathrm{m}^{-3}) = I(\mathrm{MA})/\pi a^2$ where $\bar{n}$ is the line averaged density, I is the plasma current and a is the plasma minor radius [29].

The pressure limit arises through the destabilisation of a ballooning mode, and it is the stability of the ballooning mode that sets the beta limit for a tokamak [8]. The stability of a ballooning mode can be calculated by optimising the current and pressure profiles to determine the maximum allowable plasma pressure before confinement is lost [27]. The analysis leads to an empirical expression which shows that the maximum beta is proportional to I/aB_ϕ. The Sykes-Troyon beta limit arises when the constant of proportionality is 2.8 [6]. The beta limit can be expressed as $\beta_T(\%)) \leq 4l_iI_p(MA)/aB_\phi$, as the maximum possible beta is also dependant on the current profile, which can be characterised by the internal inductance, l_i.

2.2 Disruptions

Disruptions generally consist of three distinct phases, figure 2.2 shows a typil disruption in the MAST tokamak and illustrates each of the three phases [30, 31]. The main characteristic of a disruption is the sudden loss of plasma current, which can be seen in the top panel of figure 2.2. The precursor phase lasts the longest of the three phases and arises due to the growth of modes in the plasma which produce magnetic perturbations as they rotate around the tokamak. It is possible to measure the magnetic perturbations using Mirnov coils (see chapter 3) which allow the growth of the modes to be observed. The growth of theses modes can be seen on the second panel of figure 2.2. As the mode slows and eventually ceases rotating the disruption proceeds to the thermal quench phase. The thermal quench is a rapid phase, followed by the current quench which proceeds at a slower rate than the thermal quench. The cooling of the plasma and the subsequent contraction of the current profile generate the current spike seen during the thermal quench phase. The contraction of the current profile (becoming peaked on axis) causes the inductance of the plasma to fall. However, the magnetic energy (ϵ) given by $\epsilon = 1/2LI_p^2$, where L is the plasma inductance and I_p is the plasma current, must be conserved. Therefore, the plasma current rises and the characteristic current spike is generated.

2.3 Physics of a disruption

The initial causes of a disruption can be many and varied, however, the sequence of events that mark the onset of the disruption are generally the same in each case. A general timeline of a disruption is shown in figure 2.3 and an assessment of the characteristics of each phase will be made in the following sections.

2.3.1 Precursor phase

The duration and sequence of events during the precursor phase is dependent on the initial cause of the disruption. Initial disruption causes have been investigated by several authors; density limit disruptions have been studied in detail in [30, 31, 33], q limit disruptions have been addressed by [30, 31] and beta limit disruptions have been studied in [31, 34, 35].

Density limit precursors

Density limit disruptions will initially proceed via edge cooling, which causes the contraction of the current profile as the plasma resistance increases in cool regions. As the current profile contracts the gradient of the current profile steepens in regions around rational q surfaces. The steep current gradient is destabilising

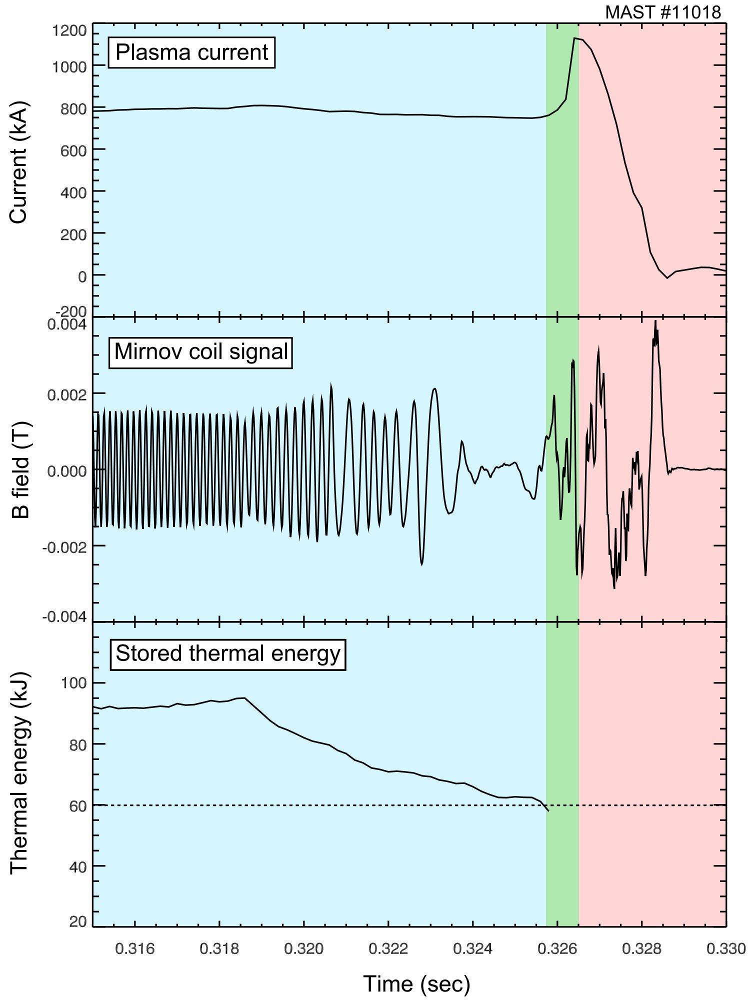

Figure 2.2: A MAST disruption is typical of a disruption in a tokamak which show three phases. The blue phase corresponds to the precursor phase, where mode growth is present. The mode begins to slow and locks, giving rise to a disruption. The green phase is the thermal quench phase where the thermal energy is deposited onto the divertor. Finally, the red phase is the current quench phase in which the plasma current is lost.

to magnetohydrodynamic (MHD) instabilities, and as a result tearing modes are produced [30].

The tearing mode produces magnetic islands in the plasma, as shown in figure 2.4. The islands cause decreased confinement as particles on the inboard side of the island can travel to the outboard side by simply moving parallel along the field line, without having to move perpendicular to the field. The parallel transport speed along the field line is significantly higher that the perpendicular transport speed, hence the confinement provided by the nested flux surfaces is 'short circuited' by the island. The islands rotate with a given frequency and are formed on particular rational surface. The mode can be identified by the q surface it forms on, hence, the tearing mode shown in figure 2.4 is a m=2/n=1 mode [6, 8].

The predominant tearing mode is a m=2/n=1 mode which grows on the q=2

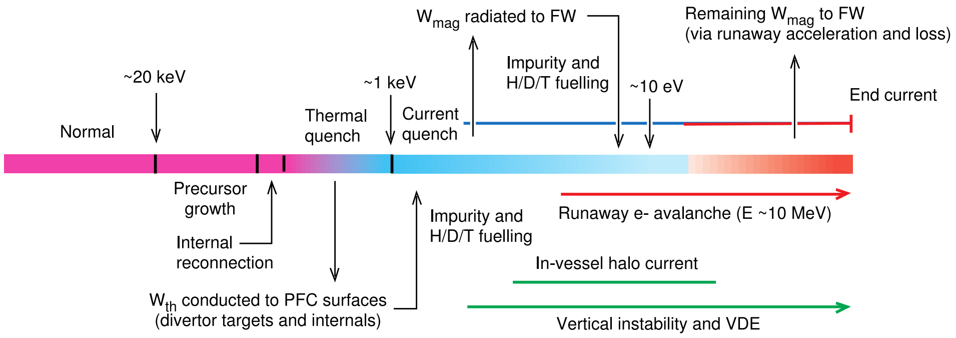

Figure 2.3: The sequence of key events during a disruption (from [32], page 118)

surface [30, 31], the rotation of the islands produced can be seen by using magnetic coils (see chapter 3). Additional low order modes can be triggered as the rotation of the 2/1 mode slows. Ultimately, the 2/1 mode can become coupled with the 1/1 mode as the current profile becomes peaked in the centre due to edge cooling [31]. Rotating modes present in the plasma are stabilised by the eddy currents that they generate in the surrounding vacuum vessel. Growth of the modes gives rise to increasing magnetic perturbation from the islands, the finite penetration time of the vacuum vessel cannot stabilise these modes and the result is a drag force on the plasma. The efficiency of the vacuum vessel wall at stabilising the modes falls as the mode slows. This is due to the increased time available for the perturbations to penetrate the wall when the mode rotates at a lower frequency. The decreasing efficiency of the wall stabilisation and the presence of toroidal magnetic error field cause the mode to stop rotating [6]. This process is known as mode locking. Once a mode locks, there is no mechanism to stabilise it and it will grow, until plasma confinement is destroyed [30, 31, 33].

q limit precursors

The precursor of a q limit disruption is shorter that than of a density limit disruption [30], however, the mechanism of mode growth and subsequent locking is the same. Typically, there is little precursor activity [30], with the disruption following rapidly once the safety factor at the edge has reached two which triggers m=2 mode growth. The thermal quench occurs at the point of mode locking [30].

Beta limit precursors

Beta limit disruptions also show limited precursor growth and are generally triggered by a different mechanism to q limit and density limit disruptions [23, 36].

The sequence of events leading up to a high beta disruption can be summarised as follows [36]. The initial stage of the high beta disruption is the growth of MHD activity at the edge of the plasma, which is similar to the density limit disruption previously discussed. The analysis of magnetic data from the TFTR tokamak [36]

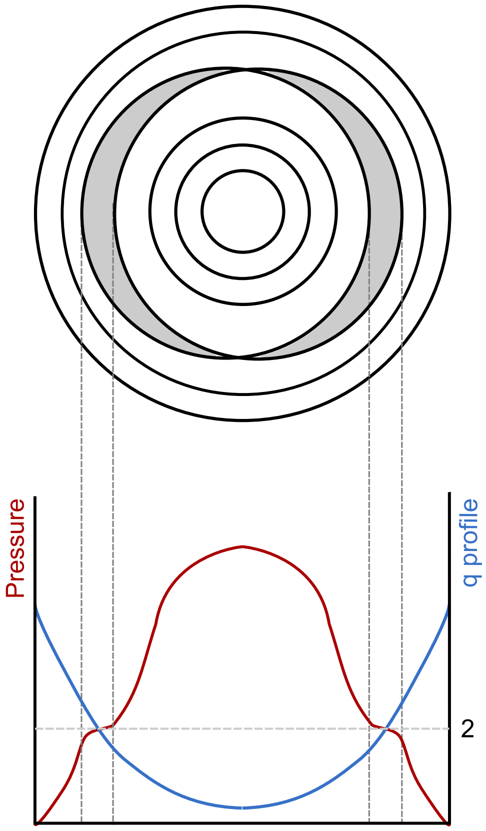

Figure 2.4: A tearing mode in a circular tokamak. The lower figures shows the pressure profile (red) and the q profile of the plasma (blue). The mode affects the temperature and density profiles as shown by the profile beneath. The mode shown is a 2/1 mode, which forms around the q=2 surface in the plasma.

shows that the initial mode is a 4/1 mode which then triggers the growth of 3/1 and 2/1 modes and finally 1/1 modes. The result of the mode growth is the cooling of the core of the plasma, causing a decrease in the stored thermal energy of the plasma. Unlike the density limit disruption, the high beta nature of the plasma cause the generation of ballooning modes, typically at the point where the 1/1 modes grow [23, 36]. The result of the ballooning modes is to cause the expansion of the hot plasma core outward into the low field side of the plasma, a result also supported by modelling [37]. The bands, or ‘fingers’, of cold plasma (see figure 2.5, from [37]) connect regions of hot and cold plasma allowing the thermal energy in the core to be lost. The size of the fingers is affected by the curvature of the tokamak, the good curvature on the inboard side acts to suppress the bands, but the bad curvature on the outboard side assists the growth of the bands. In addition, the width of the bands is affected by the resistivity of the plasma, with lower resistivities producing broader bands.

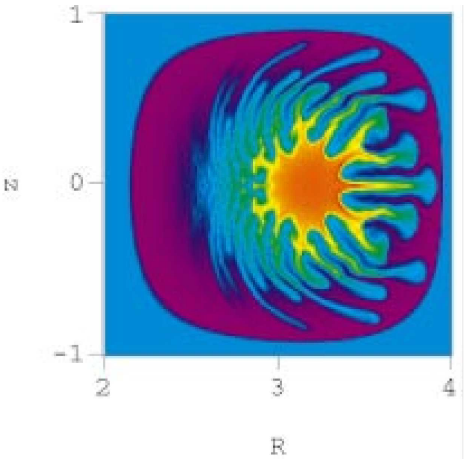

Figure 2.5: Modelling results of ballooning modes during high beta disruptions (from [37], page 105)

2.3.2 Thermal quench

The thermal quench phase of a disruption is the phase during which the stored thermal energy in the plasma is lost to the divertor and first wall surfaces and is the fastest phase of the disruption, predicted to last between 1-10 ms in ITER [23]. The onset of the thermal quench occurs when there has been significant mode growth and coupling which has significantly degraded the plasma confinement. The thermal quench typically occurs in either one or two stages [23, 31]. The number of stages of the thermal quench is thought to be determined by the initial cause of the disruption. Density limit disruptions occur in two stages [30, 31, 33], however, beta limit disruptions can occur as either single stage [31] or two stage disruptions [36].

Modelling of disruptions have shown that the coupling of the modes brings about large scale stochasticisation of the flux surfaces which allows the thermal energy to be released from the plasma [33, 38]. The two stage thermal quench model has been described in [31], the initial stage of the thermal quench is the redistribution of the thermal energy within the q=2 surface, over the plasma volume within the q=2 surface. The redistribution is caused by stochasticisation brought about by a 1/1 mode. The first stage of the thermal quench is predicted to last around 10ms on ITER [23]. The second stage of the thermal quench occurs on significantly faster timescales (around 1ms on ITER), and is less well diagnosed than the first stage due to the speed at which it occurs [31].

The thermal quench in high beta discharges is thought to be initiated by the mixing of hot and cold regions of plasma by an interchange instability [37]. The use of an interchange instability is advantageous over stocasticity based mixing, as the speed at which the mixing occurs is independent of the resistivity. The model of disruptions using stochasticity predict that the timescales should increase with increased resistivity, which would not produce a thermal quench fast enough to be consistent with the observed beta limit disruptions. In general, the speed of the thermal quench can only be explained by the conduction of particles along open field lines [31].

Thermal quench timescales

The timescales of the first and second phases of the thermal quench scale linearly with machine radius. The scaling, and existence of single and two stage thermal quenches has been seen on many machines, and the resulting timescales can be plotted as a function of minor radius to produce figure 2.6 (taken from [32]).

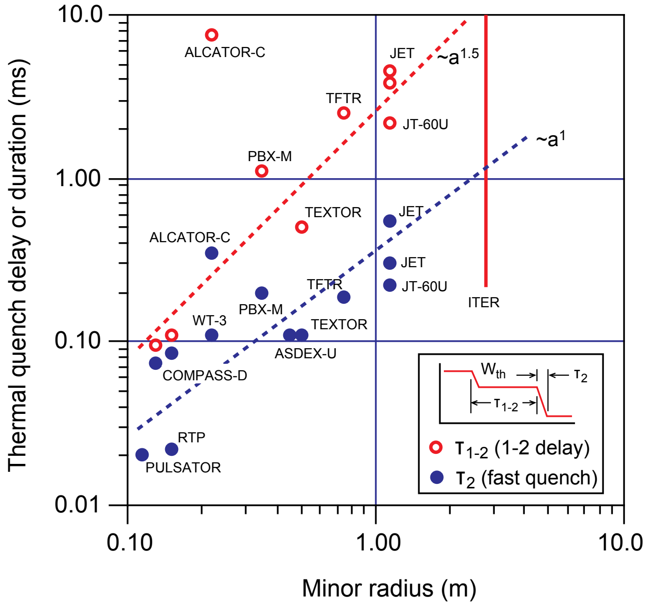

Figure 2.6: Thermal timescales for various machines, showing the scalings for both the first stage (τ_{12}) and second stage (τ_2) timescales. (from [32], page 2330)

The temporal evolution of the energy deposition exhibits two stages, the first stage is a fast rise and the second stage is a slower decay [39]. The timescales for the energy deposition are seen to be longer than the timescale of the second stage of the thermal quench [23, 39]. The timescales of the energy deposition are limited by several physical process which are detailed in [23] and can be summarised as follows. Firstly, the energy must be transported to the divertor surfaces along magnetic field lines, and the transport along field lines will be affected by the stochasticity of the scrape off layer (SOL). Secondly, the heat flux onto the divertor surfaces is limited by the power flux which can be transported through the sheath region (see chapter 3). Finally, the divertor surfaces may be shielded from the power load by neutral particles surrounding the plasma. These particles act to radiate away some of the energy lost from the plasma as it travels to the divertor and first wall [23]. It has been found experimentally [40, 41] that high beta disruptions typically exhibit the largest heat loads when compared to density limit or q limit disruptions, possibly as a result of the lower edge densities present due to the disruption not being initiated by edge cooling [41].

Divertor energy loading during the thermal quench

The energy deposited onto the divertor leads to large heat loads. These heat loads will produce significant damage to the divertor surfaces should they occur in future devices. The energy loading during a disruption is determined by a convention described in [42]. The energy loading is normalised to time and area of impact, hence the energy loading, or energy impact, η, is given by $E/A\sqrt{t}$, where E is the energy deposited over the area A in time t. The convention is chosen as the heat load is assumed to fall onto a one dimensional, semi infinite material. The solution to the heat transfer equation for such a material yields the time dependence above. The typically quantity of energy released during the thermal quench has been found experimentally on DIII-D to be between 50-100% of the thermal energy and 15-50% of the total plasma energy [40].

The area over which the energy is deposited is determined by the heat flux width during the disruption, it has been widely reported [43, 44] that there is significant broadening of the heat flux width during disruptions of between 3 to 10 times the initial width prior to disruption. Presently, the assumed broadening of the SOL for ITER is 7 times the initial pre thermal quench width, 100% of the thermal energy will be lost to the divertor and the thermal quench phase will last for between 1-10ms. The resulting normalised energy load will be between 144 and 446 MJ m^{-2} $s^{-0.5}$, which is equivalent to a power load of between 10 and 100 GWm^{-2} [23]. The normalised energy load that tungsten or carbon can withstand before melting or vapourisation is between 40 and 60 MJ m^{-2} $s^{-0.5}$. Vapour shielding of the divertor surfaces is not included in these figures, however, modelling has suggested that it is effective in decreasing the power reaching the targets during disruptions [45].

2.3.3 Current quench

The cooling generated by the thermal quench causes the resistance of the plasma to rise. The increased resistance causes a rapid decrease in the plasma current. The projected timescale of the current quench on ITER is around 36ms to fall from 15MA to zero. The current quench phase marks the conversion of the stored magnetic energy to thermal energy via ohmic heating, and the subsequent radiation and conduction of the energy to the divertor and first wall surfaces. The cooling of the plasma during the current phase brings about a change in plasma inductance. The change in inductance is rapid at the end of the thermal quench, and it is the change in inductance that gives rise to the large spike in the plasma current at the start of the thermal quench [6, 23].

Current quench forces

The rapid decrease in plasma current during the current quench generates significant forces on the vacuum vessel. The forces can be generated in two main ways, either via induced currents or halo currents. The induced current flowing in the vacuum vessel as a result of the current quench interacts with the externally produced toroidal field to produce structural stresses on the vacuum vessel. Structural forces can also be generated by halo currents and the toroidal magnetic field. Halo currents in the vessel arise due to the interaction of the plasma with the vessel or supporting structure (see figure 2.7). The interaction of the plasma with the vessel, causes the current being carried in the plasma to flow through the vessel structures.

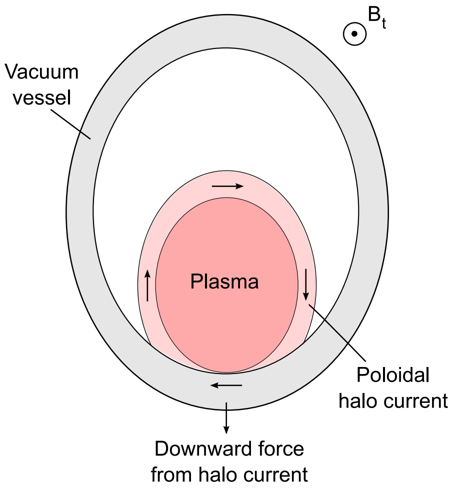

Figure 2.7: An illustration of a halo current

Vertical stability during the current quench

The loss of vertical stability which gives rise to halo currents are known as vertical displacement events (VDEs). VDEs typically affect plasmas which are elongated, but can affect circular cross section plasmas at lower rates of motion [46]. The plasma is elongated by using poloidal field coils, with currents flowing in the same direction as the plasma current. Hence, any deviation of the plasma from equidistant between the shaping coils will cause the plasma to be drawn toward the shaping coil it is the nearest to [8]. Typically, the direction in which the VDE will cause the plasma to move is found to be in the direction of the primary X point [47].

Runaway electrons

The final hazard to future tokamak devices during the current quench is the formation of runaway electrons (RE). RE are formed by acceleration (to relativistic velocities) of electrons in the plasma by the electric field generated during the current quench. It is possible for runaway electrons to carry up to 70% of the pre disruption plasma current in ITER [23]. The frequency of collisions between electrons decreases as their velocity increases (as they are Coulomb collisons), it is this phenomena that allows runaway electron production [8]. Electrons which possess sufficiently high velocities will be accelerated, and the friction that they experience as a result of collisions will decrease as their velocity increases [48]. There is a magnitude of electric field at which even thermal electrons can be accelerated to runaway energies, this field is known as the Dreicer field. The Dreicer field is modified when relativity is taken into account, giving rise to a critical electric field below which runaway electrons will not be formed [48] which will be detailed in section 2.6.4.

However, the Dreicer field is not the only means of accelerating electrons to relativistic velocities. When a relativistic electron is present in a plasma it can undergo a collision with a thermal electron in the bulk plasma, the effect of this is to accelerate the thermal electron to relativistic speeds. The formation of electrons via this 'knock on' method requires runaway electrons to already be present, but leads to avalanche multiplication of the runaway electrons [49].

The runaway electrons are confined during the acceleration phase and are typically released during VDEs. The cross section of the runaway beam is found to be small, around 10cm [50], which leads to significant damage to the plasma facing components or diagnostics which the beam may interact with. The estimated power load to due to runaway interaction on ITER is between 15 and 65 MJ m^{-2} with the threshold for ablation in graphite being around 35 MJ m^{-2} [23].

2.4 Disruption mitigation

A disruption in an ITER or DEMO class tokamak would have severe consequences for machine availability and performance. These consequences arise as a result of the impurities released during the high heat load phases, which contaminate future discharges and the structural stresses generated which can damage internal structures. It is clear from the discussions in this chapter, and the introduction to disruptions in section 1.4.1 that a scheme to mitigate the heat loads, structural stresses and runaway electrons generated during a disruption is required.

Disruption mitigation can be performed using two main techniques, these are massive gas injection or killer pellet injection. Disruption mitigation techniques rely on the injection of impurity species (elements with $Z>2$) into the tokamak. The effect of the impurity is to cause energy to be radiated away from the plasma over the whole plasma volume. The mechanisms used for disruption mitigation do not prevent the loss of the plasma, instead they produce a controlled termination of the discharge.

Disruption mitigation via killer pellet injection involves the injection of a cryogenic pellet of impurity or deuterium into the core of the plasma. The radiation generated by the injection of the killer pellet then acts to dissipate the stored thermal energy, initiate a current quench and allow the magnetic energy to be radiated [51]. Disruption mitigation with killer pellets has been shown to reduce the heat loads and electromechanical forces when compared to a natural disruption [22], however, the termination of a discharge with a killer pellet generally tends to generate runaway electrons. The explanation for the mechanism of runaway production is detailed in [22]. The runaways are thought to be generated as a result of the rapid cooling induced by the injected pellet. The cooling is sufficiently fast that the electrons in the tail of the energy distribution are not affected. The tail is not affected as the collision rate of the hot electrons is too low to allow sufficient interaction with the cooled bulk electrons. The hot electrons can then be accelerated to relativistic velocities by the induced electric field [52]. It has also been suggested that the high occurrence of runaway electrons in killer pellet discharges compared to massive gas injection terminations is due to the lower levels of magnetohydrodynamic activity in killer pellet terminations. The decreased MHD activity produces ineffective mixing of the impurities and therefore lower current quench densities and enhanced runaway production [41].

2.5 Mitigation via massive gas injection (MGI)

The process of mitigating disruptions using massive gas injection (MGI) relies on the ability to deliver a large quantity of impurity gas (>10-100 times the plasma inventory) in a short space of time (5ms) into the plasma. In the same way as killer pellet injection, the injected gas radiates away the thermal and magnetic energy stored in the plasma. The injection of large quantities of gas into the vessel requires specifically designed valves to deliver the gas to the plasma. Typically, the flow rate required for disruption mitigation should exceed 1000 bar litres per second [53].

Studies into disruption mitigation have been performed on several machines across the world. Initial disruption mitigation experiments were performed on DIII-D, in addition to killer pellet studies [22]. Table 2.1 summarises the different machines and the quantity of gas that is injected in each.

Tokamak	Number injected	Multiple of inventory	References
DIII-D	4×10^{22}	70x	[22, 54]
C-Mod	10^{23}	300x	[55]
ASDEX-Upgrade	10^{23}	70x	[56]
JET	2.3×10^{23}	5x	[57]

Table 2.1: Specification of various MGI systems

2.6 Physics of MGI

The time line of disruption mitigation has been identified on several machines, [58, 59, 60] and consists of several stages which are outlined in figure 2.8. There are five phases of a mitigated disruption, these are the vacuum transit time, edge cooling phase, destabilisation of MHD modes, the thermal quench (TQ) and current quench (CQ). The duration of each of the stages varies with machine size and injected gas quantity/species, but in general the longest phase is the vacuum transit phase. The vacuum transit phase is determined by the time taken for the injected impurity to travel from the valve nozzle to the plasma edge. The speed of gas flow to the edge is determined by the thermal velocity of the species injected, as propagation occurs at the thermal speed through the vacuum (choked flow) [39, 41, 55].

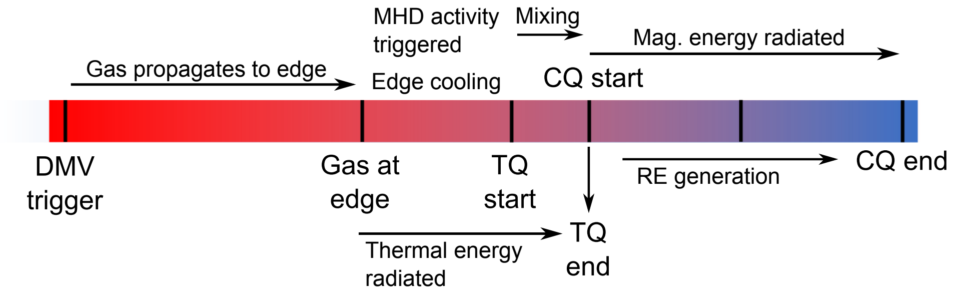

Figure 2.8: Key events during disruption mitigation from the point of triggering the disruption mitigation valve (DMV)

2.6.1 Gas propagation

The arrival of the injected impurity at the edge of the plasma occurs around 1-2ms after the triggering of the gas injection. The time is determined by the path length the gas must travel to reach the plasma edge, as the neutral injected gas is unaffected by the magnetic field. The mitigation valve is typically mounted externally from the vacuum vessel (although in vessel valves have been used [56]) and are connected by a pipe to the vacuum vessel. The typical distances between the valve and the plasma range from 1 metre in DIII-D [41] to 4 metres in JET [61]. A variety of pipe diameters are used, typical values tend to be between 2 and 5cm [59]. Larger diameter (15cm) pipes have also been used, however, the effect of the diameter on mitigation times was found to be small [58].

The arrival of the injected gas at the plasma edge leads to ionisation of the impurity, and the gas being entrained along field lines. There have been extensive studies, both experimental and theoretical into the mechanism of impurity penetration during this phase of the mitigation.The result of the ionisation is to prevent the radial expansion of the impurity into the plasma and across the field lines, but allowing the impurity to be carried along the magnetic field lines. It is thought [62] that the neutral impurity is carried along magnetic field lines via the ions which are trapped along the field. The neutral gas is entrained in the field following ions.

Analysis of high speed camera imaging on DIII-D has shown that the injected impurity does not penetrate deeply into the plasma even if the ram pressure of the jet exceeds the toroidal magnetic field pressure [58]. The investigations on the penetration depth were performed using deuterium (98%) and argon. Other studies [55] using argon helium mixtures have shown that there can be significant penetration (to a normalised radius of around 0.3) of helium into the core, in contradiction to other results reported.

Gas penetration modelling

Modelling of the impurity penetration has been performed by several authors, [63, 64, 65], and has covered the penetration of the gas into the plasma and the effect of the penetration depth on the plasma. The modelling of the jet in [64] supports the experimental findings, of radial and toroidal expansion of the cloud. Modelling has suggested that the radial penetration of the impurity is stopped due to the ionisation of the gas cloud [64]. It should be noted that the penetration of the gas cloud can be affected by the quantity of the gas injected [64]. As a result, the DIII-D results which yielded deep penetration could be due to the injected quantity exceeding a critical limit, which arises as the plasma electrons cannot penetrate the gas jet. The lack of penetration by the plasma electrons prevents heating of the injected gas jet, allowing for increased penetration [63].

The effect of the shallow gas jet penetration has been modelled by [65] where is has been shown that despite the shallow penetration, the mitigation can still be effective. In this modelling, the impurities are introduced at a set depth into the plasma and the effect of the impurities on the stability of MHD modes is then calculated. The modelling has shown that when the impurities penetrate to the q=2 surface, triggering MHD activity which generate mixing that rapidly distributes the impurity throughout the confined plasma, initiating the thermal quench [65].

2.6.2 Thermal quench

The influx of impurities to the plasma edge initiate a cooling and shrinking of the of the current channel. As the cooling front propagates toward the plasma core, as in the case of a density limit disruption, various MHD modes are triggered. The observation of mode growth has been shown experimentally [55, 58, 59] and by modelling [66]. There is limited contact between the impurity ions and the plasma at the onset of the edge cooling phase, however, the limited contact provides enough cooling to initiate the modes. These modes then rapidly increase the mixing of the impurity ions during the thermal quench [41, 62]. Measurements of the impurity mixing have been performed on DIII-D using ultraviolet diode arrays. The measurements show that limited mixing occurs prior to the thermal quench. As the thermal quench proceeds, the impurity penetration can be followed with the increase in UV light. Figure 2.9 (from [41]) shows that the majority of the impurity mixing occurs during the thermal quench, ultimately leading to the impurity being present across the plasma radius 2ms after the onset of the thermal quench [62].

The rapid mixing of impurities through the plasma is brought about by the ergodisation of the flux surfaces in the plasma. The ergodisation is caused by the growth and overlap of the MHD modes induced during the edge cooling phase [58]. Disruption mitigation modelling suggests that ergodisation leads to the loss

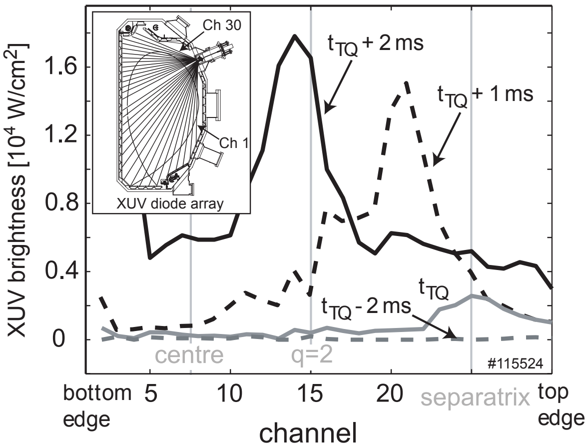

Figure 2.9: Impurity emission during neon disruption mitigation on DIII-D (from [41], page 1050)

of confinement associated with the thermal quench [66]. The modelling couples a pellet code, to handle the radiation of the injected impurities and NIMROD, an MHD code to model the effects of the cooling on the equilibrium. The result of modelling neon mitigation in C-Mod is shown in figure 2.10 (from [66]) which shows the evolution of the equilibrium through the thermal quench. It is clear from this analysis that the destruction of the closed flux surfaces occurs during the thermal quench when the stored thermal energy is lost from the plasma.

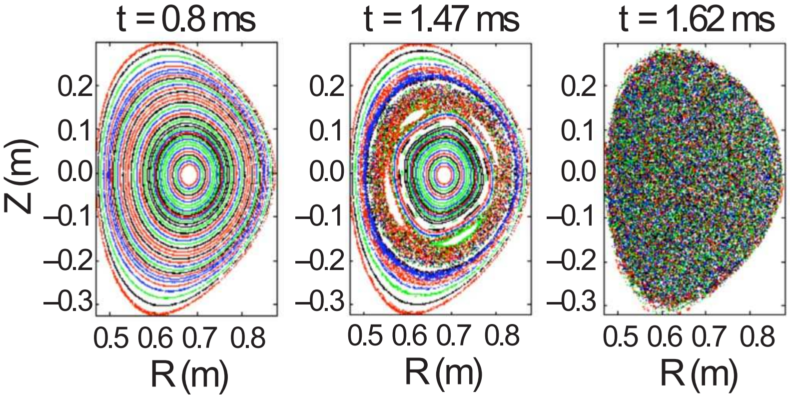

Figure 2.10: NIMROD modelling of the thermal quench on C-Mod (from [66], page 4). The time t=0 corresponds to the impurity arriving at the plasma edge (TODO)

NIMROD modelling of the mitigation has shown the rapid growth of MHD generates the thermal quench. The dominant mode numbers of the MHD produced are 2/1 and 1/1 modes in C-Mod which is consistent with experimentally measured magnetic coil signals [58, 60]. Although, it has been argued in [41] that the speed at which the thermal quench takes place is far quicker that the timescale for the overlap of modes. Instead, it has been suggested that the rapid thermal quench is brought about by the plasma exceeding an ideal limit, where modes can grow rapidly on timescales consistent with those of the thermal quench [41].

The analysis of the temperature and density profile evolution during a mitigated discharge can be used to assess the penetration of the impurities and the mechanism by which the stored energy is lost. Data from DIII-D [41] shows that during the mitigation, both the central electron density and temperature decrease, whilst the edge temperature falls and the density rises. The behaviour of the edge density and temperature is consistent with the heat stored in the plasma being used to ionise the impurity thereby producing radiation. However, the same cannot be said for the core. The evidence from the core is that heat is lost suddendly, causing a drop in temperature and density. A possible explanation for the transport of heat from the core is that mode growth has connected the edge regions and the core regions which allows transport along open field lines to take place. The radial position where the electron density changes from rising to falling can be thought of as the maximum penetration depth of the impurities, the DIII-D data shows that this radius is around the q=2 surface [41].

Analysis of magnetic coil data has shown that the arrival of the cooling front at the q=2 surface is associated with the formation of a 2/1 mode [41, 41, 60]. The observation of the rapid 2/1 mode growth associated with the arrival of the cooling front at the q=2 surface seem to indicate that the q=2 surface is critical in determining the onset of the thermal quench. Experiments have been performed on DIII-D to determine if a critical q surface exists. A critical surface would be defined as a surface to which the cold front must propagate in order to trigger the thermal quench [60]. The experiments performed involved mitigating a plasma where the value of q at q_{95} is varied by changing the toroidal magnetic field. The effect of increasing the depth of the q=2 surface is to increase the time required between the edge temperature collapsing to half the pre-mitigation value and the central temperature contracting to half the original value. The timescale of the thermal quench, defined as the time required for the central electron temperature to fall from 90% to 10% of the initial value, remains unaffected by variation of the q=2 surface depth [60].

Mitigated power loads

The heat load on the divertor surfaces during mitigated disruption are decreased over the natural cases, particularly, when a high Z mitigation gas is used. The effect of increasing the Z of the injected impurity can be seen using data from C-Mod (figure 2.11) which shows a time history of the divertor temperature for various injected species. The divertor temperature is reduced in all cases of mitigation when compared to the natural disruption. The duration of the temperature rise is also decreased with increasing impurity Z [58].

Despite the advantage of decreased divertor heat loads when higher Z impurity gases are used, there is a disadvantage as a result of the higher mass. The speed of impurity propagation into the vacuum vessel from the valve occurs at the thermal

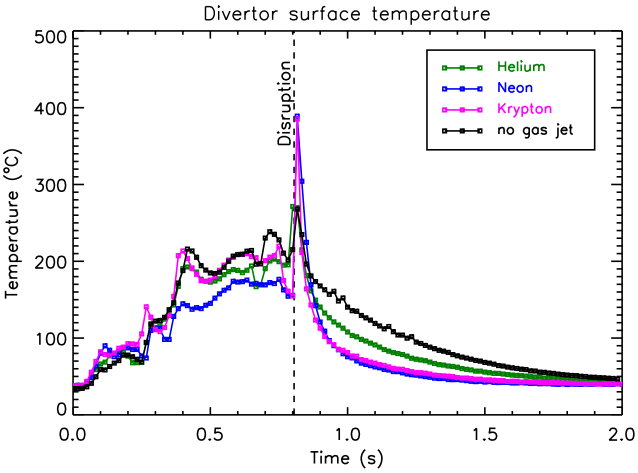

Figure 2.11: The effect of disruption mitigation on the divertor temperature (from [58], page 1088). The data for krypton shows higher temperatures than in the natural disruption as a result of motion of the camera during the disruption. The motion of the camera prevents accurate data from being gathered during a 60ms period after the disruption [58].

speed of the impurity, hence, high Z impurities are slower to arrive at the plasma edge [59]. It is possible to use a lighter 'carrier' gas, such as deuterium or helium, to decrease the transit time. Mixtures of heavy and light gases can be used to entrain a heavier species, thereby providing increased radiation power and minimising the transit time [62]. A variety of mixtures of impurity gases have been used, from 98% deuterium/2% argon [58, 62], to 10% neon or argon with 90% deuterium [67]. It has been shown on JET [68] that the mixtures using deuterium or helium and a heavier gas produce similar effects in terms of cooling time, transit time and current quench time. It has also been shown that the mixtures of argon and helium or deuterium are similar in performance to neon, and are faster propagating that pure argon alone.

The large quantity of radiation produced during the mitigated thermal quench can pose a risk to the walls of ITER if the radiation is localised in one region [69]. If the mitigation produces a region of concentrated line radiation in the region around the injection port, then the wall in this region can experience a high radiated heat load, as opposed to a high conducted heat load. The amount of radiation localisation needs to be assessed in order to develop an effective disruption mitigation system for ITER. The key design decision to reach during the construction of the ITER disruption mitigation system is the number of injection ports required to prevent the melting of the beryllium walls as a result of radiation asymmetry. The present design is to have 2 ports for injection [70], but results from C-Mod [71] and ASDEX-Upgrade [72] suggest that there is a radiation asymmetry during mitigation (of between 0 to 30% in ASDEX) which could lead to additional ports being required, perhaps 6-8 ports [69]. Assessment of the radiation asymmetry is required from present day machines to refine this part of the ITER design.

2.6.3 Current quench

The current quench marks the conversion of the stored magnetic energy into thermal energy via Joule heating, the energy is used to heat the remaining plasma which then radiates to dissipate the energy [58].

The duration of the current quench, τ_{CQ}, is approximately given by L/R, where L is the plasma inductance and R is the plasma resistance. Hence, the speed of the current quench is set by the type and quantity of impurity which is assimilated into the plasma core during the thermal quench [60]. The use of high Z impurities therefore will produce the largest amount of plasma cooling, and therefore the highest resistivity. The result of using a high Z impurity to mitigate a discharge is to increase the speed of the current quench, low Z impurities on the other hand, produce longer current quench times. The timescales for various types of impurity can be seen in figure 2.12 which is from the JET tokamak [67]. The timescales are normalised to the plasma cross section to allow extrapolation to ITER. The ITER lower limit on current quench rate determined by the maximum allowable induced current and is given as 1.67 ms/m^2 [23].

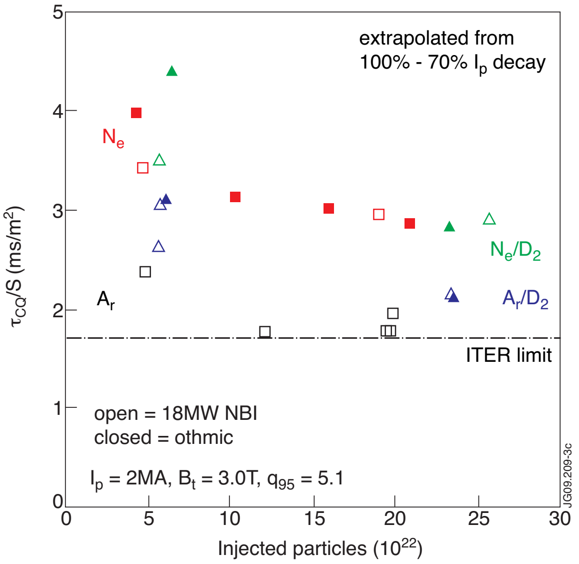

Figure 2.12: Mitigated current quench timescale i[2]

The choice of impurity to use strongly depends on the type of tokamak on which the mitigation is to be performed. Tokamaks that are circular in cross section have better vertical stability than those which are elongated. During a disruption or a mitigation, elongated plasmas, such as in MAST, typically undergo vertical displacement events (VDEs). Vertically unstable plasmas are best mitigated using high Z impurities which bring about the destruction of closed flux surfaces prior to the interaction of the plasma with the vessel, thereby limiting the production of halo currents [58, 59]. Low Z impurities are best suited to vertically stable, circular plasmas where the largest structural stresses come from induced currents.

Therefore extending the time over which the current quenches reduces the induced eddy current size. It has been seen that massive gas injection is an effective means of controlling halo currents, with a 50% reduction in halo current size being observed on C-Mod [58]. Reductions in halo current size and vessel forces via mitigation have been seen on ASDEX-Upgrade [59].

2.6.4 Runaway electrons

The suppression of runaway electrons requires a sufficiently high number of electrons, either bound or free, at the current quench in order to collisionally suppress the generation of runaways [58]. To achieve collisional suppression, the critical electric field at which runaways are generated must be raised above the toroidal electric field generated during disruptions or mitigated terminations. The critical electric field for runaway production can be expressed as $E_c = 0.12 n_e$ where n_e is the number density of free and bound electrons in units of $1 \times 10^{20}\mathrm{m}^{-3}$ [48, 59, 73]. The estimated electric field during a disruption on ITER is predicted to be around 40 V/m, this will require a density of $4.2 \times 10^{22}\mathrm{m}^{-3}$ to collisionally suppress runaways [23]. However, it must be noted that the electrons must have been mixed into the plasma (assimilated) during the thermal quench to be effective. As the impurities must be assimilated during the thermal quench, a sufficient number of impurities must be delivered to the plasma prior to the onset of the thermal quench. The percentage of injected impurity ions which are assimilated is around 20% to 25% [61, 74]. These considerations lead to the requirement that the ITER disruption mitigation system will need to deliver around 5000 bar litres ($\approx 1 \times 10^{26}$ particles) to the ITER vacuum vessel prior to the thermal quench onset. The injection of this quantity of gas will raise the vacuum vessel pressure to 300Pa, which may result in the regeneration of the cryopumps [75] which will delay operations.

An additional mechanism for mitigating runaway electrons relies on the use of magnetic perturbations to destroy the closed flux surfaces on which they form [76]. It is thought that the absence of runaways in the majority of discharges on C-Mod and DIII-D is caused by the large scale MHD activity which destroys flux surfaces preventing the formation of runaway electrons [58, 73].

2.7 Summary

This chapter has reviewed the operational limits of tokamaks which identify the regions in operating space outside of which a disruption is likely to occur. Disruptions undergo three distinct phases, each of which pose significant challenges for future devices in terms of divertor power loading, structural stresses and runaway electron formation. The detrimental effects a disruption will have on future devices means that a disruption mitigation scheme must be employed. Experiments have been performed on several tokamaks using massive gas injection to mitigate disruptions.

These studies have shown massive gas injection to be a promising technique for mitigation.

However, a number of issues must be addressed before massive gas injection becomes the solution to disruptions in future devices such as ITER and DEMO. Firstly, the interaction between the injected gas and the plasma is poorly understood. The enclosed nature of present day tokamaks prevent extensive imaging of the gas penetration. In addition, high spatial and temporal measurements of the profile evolution are not possible in several machines, which limits the understanding of how and where the injected impurities are assimilated into the plasma. These issues prevent the dynamics of MGI from being accurately studied. The heat loads and halo currents have been assessed on several machines. Heat load analysis is complicated in conventional tokamaks due to closed divertor geometry. The closed geometry prevents direct views of the divertor and requires lines of sight which pass through the plasma. The radiation emitted by the impurities can then affect the accuracy of the heat load measurements.

Finally, all present experiments involve mitigation into conventional tokamaks. Whilst the conventional tokamak is the chosen design for ITER and DEMO, the testing of components for these devices requires the production of high heat loads in a compact facility, such as a spherical tokamak (ST). Therefore, assessment of disruption mitigation in an ST is of key importance for ITER and DEMO.

Chapter 3

MAST and Diagnostics

The Mega Ampere Spherical Tokamak (MAST) is located at the Culham Science Centre in Oxfordshire, and has been operating since 1999. MAST is of a similar design to the successful START spherical tokamak which operated during the 1990s. In this chapter, the basic design and operating capabilities of MAST will be outlined and details of the diagnostics relevant to the study of disruptions and disruption mitigation will be provided.

3.1 Introduction to MAST

MAST is a mid sized tokamak capable of producing plasmas with a plasma current of up to 1.5MA, but more typically of around 750kA. The design of MAST reflects the design of its predecessor, START, both are spherical tokamaks (see chapter 1.3) and are designed with no close fitting vacuum vessel. MAST consists of a 4 metre high, 4 metre diameter vacuum vessel, around which the central solenoid, vertical field coils, divertor and toroidal field coils are constructed. The toroidal magnetic field is produced by twelve toroidal field coils, which divide the machine into twelve sectors. The poloidal coils, toroidal coils and centre solenoid in MAST are water cooled. Cooling is required to dissipate the Joule heating generated in the centre solenoid. The Joule heating limits the maximum discharge duration to 0.7 seconds. Typically, discharges are 0.3-0.5 seconds in duration, at the nominal rate of four per hour. MAST is equipped with two neutral beam injectors (NBIs) as a source of external plasma heating. The basic design parameters of MAST are shown in table 3.1 and a cross section of MAST can be seen in figure 3.1 [77, 78].

In 2004 several changes were made to the MAST tokamak, these changes included a new increased length centre column, repositioned divertor coils to extend the accessible range of elongation and an improved divertor [79].

The geometry of the plasma in MAST can be varied between double null (DN) or single null (SN), where SN discharges can be either upper single null, (USN) or lower single null (LSN). In addition, the DN discharge can be operated with two X points on the same flux surface (known as connected double null (CND)), or with two X

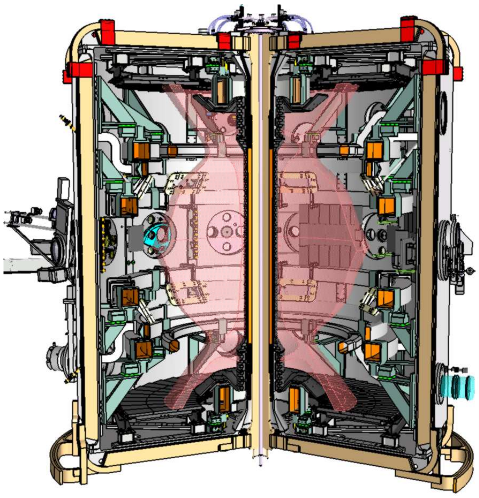

Figure 3.1: The Mega Ampere Spherical Tokamak (MAST)

points on differing flux surfaces which is known as disconnected double null (DND). The inner strike points in all configurations sit on the extremes of the centre column, with the outer strike point resting on the toroidally symmetric divertor tiles. The strike point position evolves during the ramp up phase of the discharge as a result of the sweeping of the solenoid current. A selection of the various configurations of the MAST plasma can be seen in figure 3.2.

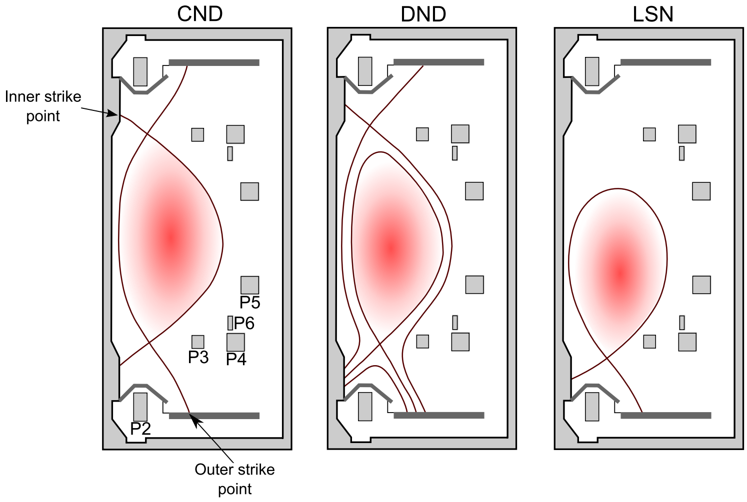

Figure 3.2: Typical discharge geometry in MAST.

3.1.1 The MAST Divertor

The divertor region of a tokamak must handle the steady state power load deposited onto it by plasma crossing the LFCS. The basic design and operation of a divertor was discussed in section 1.2.2, and is created by the formation of a null in the poloidal field.

The divertor is the region in which the plasma is brought into contact with a

Parameter	Value
Plasma current	1-1.5 MA (750kA typ.)
Major radius	0.9m
Minor radius	0.6m
Toroidal field	0.55T (@ 0.9m)
Discharge length	0.3-0.5 seconds typ.
NBI heating power	5MW (2 PINI @ 2.5MW)
Typical core T_e	0.5-2.0keV
Typical core n_e	$1 - 3 \times 10^{19}\mathrm{m}^{-3}$
Plasma volume	$10\mathrm{m}^3$
Vessel volume	$50\mathrm{m}^3$
Aspect ratio	1.3
Elongation (κ)	$1.6 \leq \kappa \leq 2.5$
Triangularity (δ)	$\delta \leq 0.5$

Table 3.1: Key MAST parameters ([77, 78])

material surface. The region where the plasma interacts with the divertor target, the strike point, is highly localised with widths of a few centimetres. The strike point width is set by the ratio of the parallel and perpendicular transport in the plasma edge and is approximately 1cm on MAST. During plasma material interaction, the flux of electrons onto the surface will be greater than the flux of ions, due to the lower mass and higher velocity of the electrons. A plasma will seek to remain an overall neutral charge, known as quasineutrality, and any electric fields which form will be shielded from the bulk plasma. The negative charge on the material surface therefore acts to repel electrons from the surface and accelerate ions toward the surface. In order to obtain zero current, the potential of the wall must be sufficient to repel electrons in the plasma with energies around the plasma temperature. Hence, the wall potential is of the order $-kT_e/e$ [9]. The speed at which the ions leave the plasma is defined by the Bohm criterion. The Bohm criterion can be derived by solving Poisson's equation in the sheath region where the electron density distribution is Boltzmann and the ion density can be obtained by using energy and particle conservation [4].

$$u_{Bohm} = \left(\frac{k(T_e + T_i)}{m_i}\right)^{\frac{1}{2}} \tag{3.1}$$

The Bohm criterion, equation 3.1, states that the sheath will form when the fall in potential with respect to the bulk plasma is $T_e/2$ (when $T_i = 0$) due to the ions requiring a fixed energy prior to entering the sheath. The effect on the plasma potential, density and pressure can be seen in figure 3.3.

The initial MAST divertor was composed of several ribs and boxes, which formed a toroidally asymmetric divertor and shadowed the bottom of the MAST vacuum vessel from plasma impact. The improved divertor (2004 onwards) is toroidally symmetric, composed of graphite and consists of 48 individual elements. The individual elements are separated by a gap to provide diagnostic access, as a result of this requirement, the individual tiles are inclined at 4 degrees in the toroidal

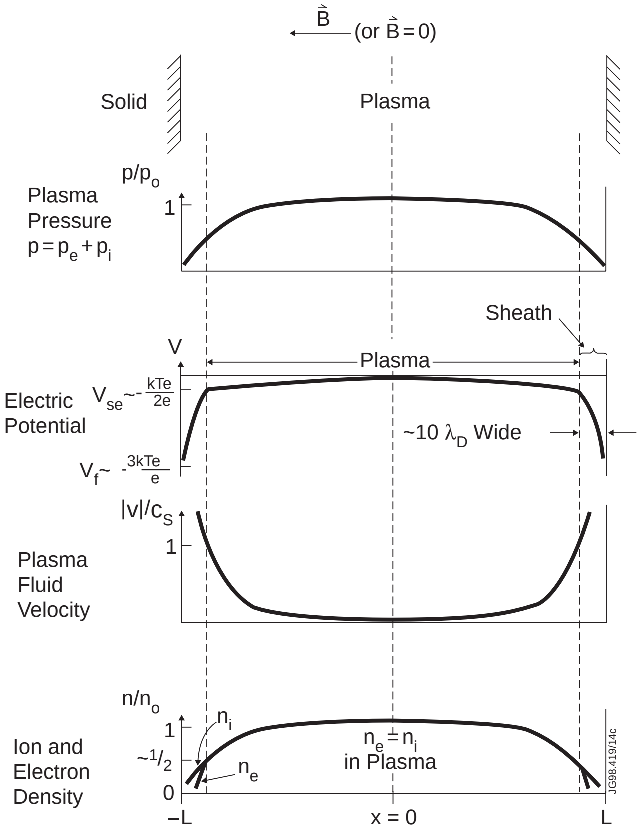

Figure 3.3: The plasma sheath (Image from [9])

direction to shadow the gap from plasma interaction. The divertor tiles are also fitted with in built Langmuir probes for the determination of edge temperatures and densities [79].

3.2 Diagnostics

MAST is equipped with a wide range of diagnostics which are suited to the study of disruptions. In this section the key diagnostics which will be used in future analysis will be detailed. An overview of the diagnostics installed on MAST is shown in figure 3.4.

3.2.1 Magnetics

Magnetic pick up coils consist of loops of wire, when a current is driven in a plasma, either externally or through the formation of a magnetic instability the magnetic field generated can be detected using the coils [6]. The magnetic flux passes through the coil and a voltage is induced across the ends of the coils as a result of Faraday's Law. The magnetic field can be determined by integrating the voltage signal with respect to time once the area of the coil has been accounted for [80].

There are three main types of coil in MAST, these are Rogowski coils, Mirnov

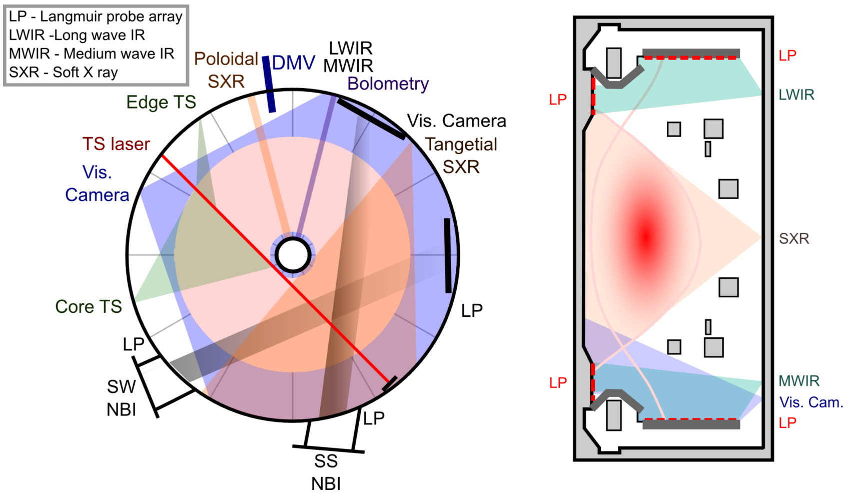

Figure 3.4: Overview of diagnostics on MAST

coils and voltage loops. Rogowski coils are solenoidal coils which are used to measure the currents flowing in conductors and plasmas. Voltage loops are unintegrated and are used to measure induced voltages, for example the voltage induced by the solenoid on the plasma which drives the plasma current. Finally, Mirnov coils are used to measure magnetic instabilities and these are typically located in arrays poloidally and toroidally spaced around the vessel to enable the reconstruction of poloidal and toroidal mode numbers [80].

During disruptions it is possible for large currents to flow in the vacuum vessel or vessel components [23]. These currents, known as halo currents, can cause significant damage to the components that they flow through. Magnetic Rogowski coils are located at key points around the vessel in order to monitor currents flowing in the structures. The location of the halo current detectors can be seen in figure 3.5 which shows one quadrant of the MAST vessel. The coils are located symmetrically in the other three quadrants.

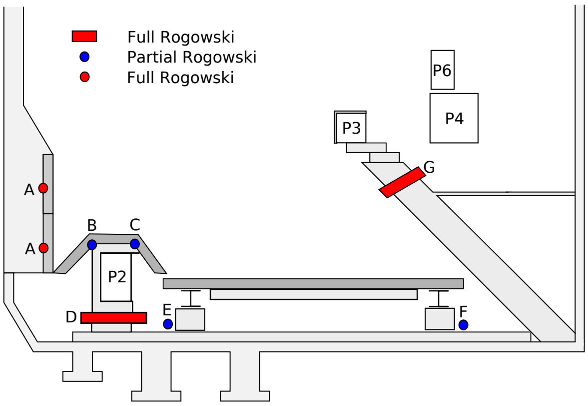

Figure 3.5: Diagram showing the lower half of the MAST vacuum vessel (see figure 3.2 showing location of the halo current detectors in MAST.

3.2.2 Langmuir probes

Langmuir probes are the simplest form of temperature and density measurement on a tokamak. They are suited to the analysis of target measurements, as they rely on being in contact with the plasma. A Langmuir probe consists of a conductor in contact with the plasma, typically the area of the probe in contact with the plasma will be controlled by surrounding it in an insulating material [6, 80]. A Langmuir probe simply placed into the plasma will become charged by electrons due to their higher speed over the ions. As a result of this charge, a sheath will form and the ion current to the probe will balance that of the electron current. The voltage reached on an unbiased probe is known as the floating potential and is shown in figure 3.6.

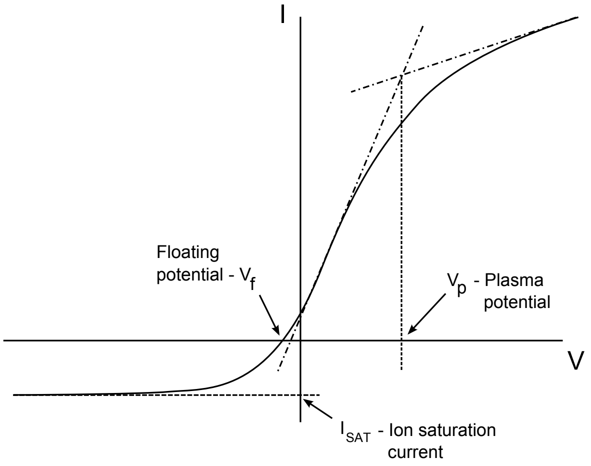

Figure 3.6: A Langmuir probe current-voltage (IV) characteristic

The measurement of the temperature and density of a plasma using a Langmuir probe can be explained using a current-voltage (IV) characteristic. The measurement is performed by biasing the probe to negative voltages, with respect to the potential of the plasma (the plasma potential) and then sweeping the bias voltage upwards. The effect of this is to generate an IV characteristic, which records the current arriving at the probe for a given bias voltage. The negative bias causes all electrons arriving at the probe to be repelled, hence the current arises solely from ions and is known as the ion saturation current. When the probe is biased positive with respect to the plasma potential, the current collected is due to electrons only and is known as the electron saturation current. In general it is undesirable to operate in the electron saturation current region, this is due to the large current which is drawn from the plasma. The large current arriving at the probe causes rapid heating which can damage the probe and the large current also perturbs the plasma. The region of interest in the IV characteristic is the ion saturation region through to the plasma potential. In the region between the floating potential and the plasma potential, the current arriving at the probe is composed of electrons and ions. It is in this region that the electron energies are sampled. At bias voltages close to the ion saturation region, only the most energetic electrons reach the probe, as the bias voltage is increased, then the number of electrons increases [9, 80].

If a Boltzmann distribution of electron energies is assumed, then the electron current arriving at the probe is given by equation 3.2 and the ion current is given by equation 3.3 due to the number of electrons arriving at the probe being set by the Bohm speed [80].

$$I_e = \frac{1}{4} n \bar{v} e^{\frac{eV}{T_e}} \tag{3.2}$$

$$I_i = nAe \left(\frac{T_e}{m_i} \right)^{\frac{1}{2}} e^{-\frac{1}{2}} \tag{3.3}$$

The total current arriving at the probe is the sum of the electron current and the ion current. The equation 3.4 can be used to calculate the electron temperature of the plasma from the IV characteristic. The ion density, and electron density through quasineutrality, can be derived using equation 3.4 once the temperature has been found [80].

$$\begin{aligned} I &= neA_p \left(\frac{T_e}{m_i} \right)^{\frac{1}{2}} \left[\frac{1}{2} \left(\frac{2m_i}{m_e \pi} \right)^{\frac{1}{2}} exp \left(\frac{eV}{T_e} \right) - exp \left(-\frac{1}{2} \right) \right] \\ &= -I_{sat} + neAp \left(\frac{T_e}{m_i} \right)^{\frac{1}{2}} \left(\frac{m_i}{2m_e \pi} \right)^{\frac{1}{2}} exp \left(\frac{eV}{T_e} \right) \\ &= I_{sat} \left[exp \left(\frac{e(V - V_f)}{T_e} \right) - 1 \right] \end{aligned} \tag{3.4}$$

MAST is equipped with Langmuir probes on the inner and outer divertor surfaces. The outer divertor surfaces have 92 probes across the major radius of the divertor with arrays of probes in three toroidal locations on both the top and bottom divertor. The inner strike point at the top and bottom of the machine have around 100 probes each in one toroidal location only. The location of the probes can be seen in the figure 3.7 and allow the Langmuir probes to be used to study toroidal asymmetries in the energy arriving at the divertor.

At any one time, there can be a maximum of 384 probes operational due to the finite number of amplifiers and digitisers available. There are 16 probes connected to each amplifier, with each probe being sampled every millisecond. In addition to providing temperature and density measurements, it is also possible to operate the probes to collect the ion saturation current only. Operation in this mode allows for higher temporal resolution data to be collected, as the probes do not need to be swept. The sample time in ion saturation mode is 0.7ms compared to the rate in swept mode which is 1.04ms.

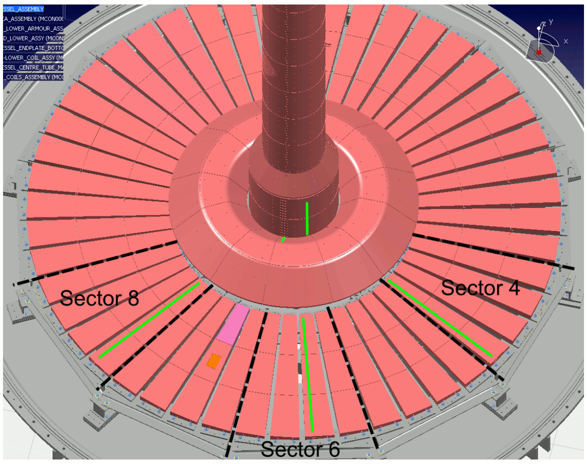

Figure 3.7: Langmuir probe locations in MAST (Courtesy MAST Design Office)

3.2.3 Thomson Scattering (TS)

Thomson scattering can be used in tokamaks to determine the plasma temperature and density in the core region [81]. In order to perform measurements using Thomson scattering, a high intensity laser is passed through the plasma. The effect of the laser is to cause the free electrons in the plasma to emit dipole radiation as a result of the oscillating electric field generated by the laser. The collected light from the electrons will be of the form of a broadened line centred on the laser wavelength, the broadening is generated by the random thermal motion of the electrons and hence can be used to determine the temperature of the plasma [82]. The intensity of the scattered light is proportional to the electron density, hence the density can be determined by calculating the area under Thomson scattering spectrum.

MAST is equipped with two Thomson scattering systems, which operate at different wavelengths. The first system uses a ruby laser and can be used once per discharge with 300 data points across the plasma radius. The Nd:YAG system uses neodymium-doped yttrium aluminium garnet as a lasing medium and can provide 130 spatial points with a continuous time resolution of 4.2ms. Alternatively, the Nd:YAG system can be operated in burst mode where a succession of up to eight laser pulses can be fired with spacings down to 5 μs. The group of eight lasers can then be repeated every 33ms throughout the discharge. The collection optics for the Thomson scattering system is composed of two parts, a collection lens for the core region and a collection lens for the edge region. The edge TS system provides an additional 16 data points from 1.29m radius to 1.45m radius. The layout of the laser and collection optics can be seen in figure 3.8 [83].

3.2.4 Soft X Ray (SXR) cameras

Bremsstrahlung radiation is emitted from the electrons in an ionised plasma when they are accelerated by the ions in the plasma. The optimum range for viewing

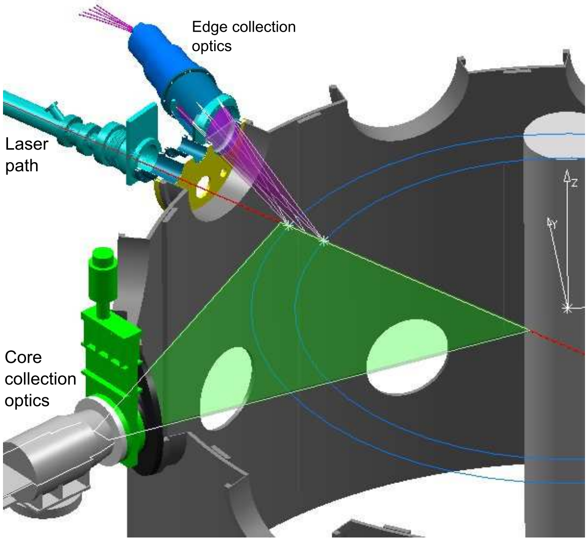

Figure 3.8: MAST Thomson scattering system (Courtesy MAST Design Office)

bremsstrahlung in a tokamak is in the region where the photon energy is approximately equal to the electron temperature [80] which is in the soft X ray region. The emission of bremsstrahlung radiation is affected by the plasma temperature, density and effective charge as shown in equation 3.5 [84].

$$P_{Brem}[W/m^3] = \frac{Z_{eff}^2 n_e n_i}{(7.69\text{x}10^{18}\text{m}^{-3})^2} T_e[eV]^{\frac{1}{2}} \tag{3.5}$$

The effective charge, Z_{eff}, is the average charge state of the ions in the plasma and is used as a measure of the quantity of impurities present in the plasma. A pure deuterium plasma will have an effective charge of one, as the impurity quantity grows the effective charge will increase. The plasma temperature and density are affected by the presence of magnetohydrodynamic (MHD) instabilities, which generate island structures and large scale plasma instabilities. The use of SXR emission can determine the mode numbers of these instabilities and the poloidal topology of the instability. The measurements of SXR emission are performed using viewing chords and are as such line integrated. The location of MHD activity inside the plasma can be identified by using the strength of the SXR oscillations across the viewing chords [6].

The MAST SXR system is composed to two main SXR arrays, with the detection of the SXR being performed using a photo diode fitted with a 12.5 μm beryllium filter to remove emission below the electron temperature of the plasma. The two arrays used for SXR analysis view radially into the plasma at a fixed poloidal location (sector 2) and tangentially across the plasma major radius from sector 2. The individual SXR chords used can be seen in figure 3.9, where the radial view is composed of two separate arrays for the upper and lower half of the plasma. The upper and lower radial arrays have two overlapping chords to enable the two to be

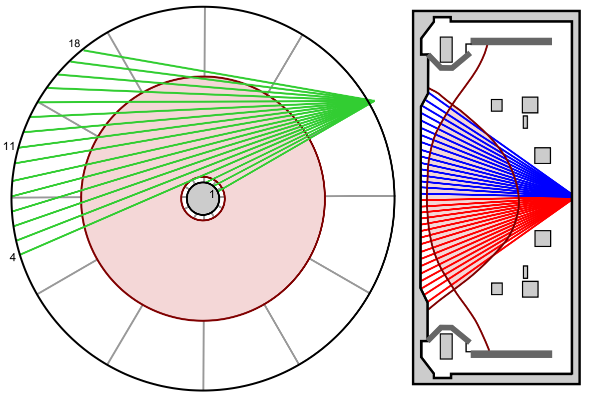

Tangential SXR chords

Poloidal SXR chords

Figure 3.9: Soft X ray viewing chords in MAST. The tangential chords are shown on the left and are number from 1 on the centre column to 18 on the outer plasma edge. The radial chords are shown on the right, with the blue chords corresponding to the upper camera and the red the lower. The radial chords are numbered from as chord U1 and L1 at the midplane and U18 and L18 at the X points

calibrated and can operated at up to 500kHz [85].

3.2.5 Bolometry

The emission of line radiation can be a significant source of energy loss from a plasma. Bolometry can be used to measure the quantity of energy that is radiated away from the plasma in the form of line radiation. Bolometers use an element which absorbs the incident radiant energy and causes the temperature of the absorber to rise. It is then possible to calculate the power delivered to the absorber and hence the power radiated from the plasma [6, 80].

MAST is fitted with a multi channel gold foil bolometry system, which views poloidally and toroidally. The poloidal view covers the length of the plasma vertically, including both X points. The viewing chords of the bolometry system are shown in figure 3.10 and the bolometry system is located in sector 2 of the MAST vessel [86]. The maximum sample rate is 2.5kHz and is heavily smoothed. These factors prevent the separation radiated power between each disruption phase from being identified.

3.2.6 Infrared (IR) Thermography

IR thermography is technique which can be used to determine the heat flux received by plasma facing components in the tokamak. The most common use of IR thermography in present day machines is the monitoring of the heat loads on the divertor surfaces for the purposes of physics studies.

MAST uses two IR cameras for thermography which cover two different wavelength ranges, both cameras image the divertor using a focal plane array. The long wave IR (LWIR) camera is a Thermosensorik CMT 256 LHS and typically views the

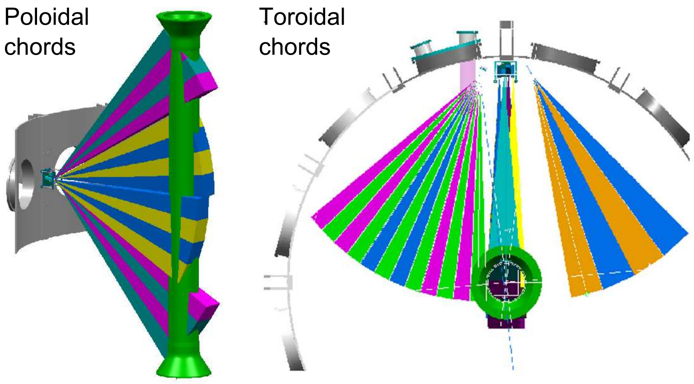

Figure 3.10: Bolometry viewing chords in MAST. The left hand image shows the poloidal chords and the right hand images shows the toroidal chords. The toroidal chords view in the co and counter direction, with the orange and blue chords viewing in the counter plasma current direction. (Courtesy MAST Design Office and [86])

upper divertor of MAST. The medium wave IR (MWIR) camera is a Santa Barbara Focal Plane SBF125 and views the lower divertor. The IR cameras are mounted on supports outside the vacuum vessel and view the divertor surfaces through a vacuum window. The specification of the two cameras is shown in table 3.2.

Parameter	LWIR	MWIR
Wavelength range	7.6-9.0 μm	2.5-5.0 (filtered to 4.5-5.0) μm
Detector size	256x256 pixels	320x256 pixels
Frame rate (@ full frame)	880Hz	315Hz
Maximum frame rate	25kHz (128x8)	10kHz (128x8)
Typical spatial resolution	7mm	5mm
Data transfer	Fibre optic	Fibre optic

Table 3.2: MAST IR camera specification

The standard camera views are configured to allow the coverage of the inner and outer strike points of the upper and lower divertor. The total strike point coverage allows the measurement of the total power delivered to the divertor. The standard IR camera setup is shown in figure 3.11, where the upper images are from a CAD model of MAST and the lower images are the IR camera images which cover the inner and outer strike point [87].

High frame rates are required on the IR cameras to capture the rapid thermal energy loss (0.3ms duration) during a disruption. To obtain high frame rates the image size is reduced down to approximately 256x8 pixels. The windowed regions are shown on figure 3.11 by red rectangles. The full frame view is required to align the camera image with a wire frame model of the MAST vessel. The alignment is required to allow the conversion of camera pixel space to real space. The conversion to real space then allows the temperature and heat flux to be derived as functions of radius across the divertor surface (see section 7.2). The alignment is performed using the alignment code LEON, which was developed for MAST based on the LEOPOLD

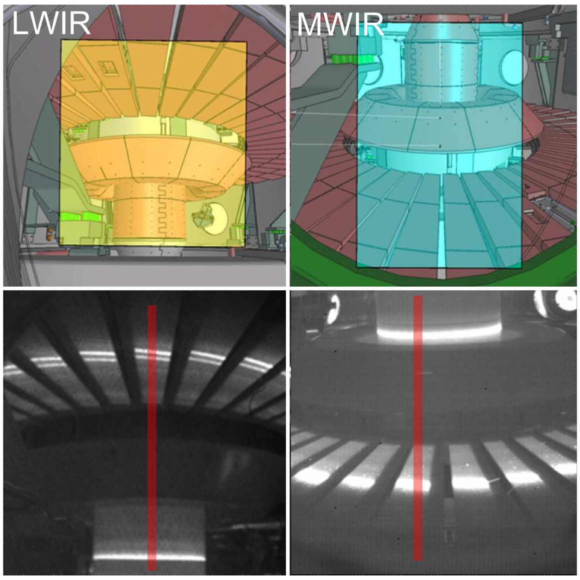

Figure 3.11: MAST IR coverage. The red regions indicate the location of the high speed window (CAD drawings courtesy CCFE Design Office)

code used by ASDEX Upgrade [88].

Calibration

The camera must be calibrated to relate the number of photons recorded to the number of photon counts emitted by the black body source. The first stage of the calibration is performed by viewing a black body calibration source and recording the number of photons collected for a given temperature. The camera is linear in flux versus counts, but exponential in counts versus temperature. The calibration is also dependent on the integration time and frame rate, therefore the calibration is performed for five various settings, covering a temperature range of 25 to 750^{o}C. The data from these integration times can then be fitted, allowing the calibration factor to be determined for all integration times. Once the laboratory calibration is complete, the camera is calibrated on the MAST vessel using a heated tile fitted inside the MAST divertor. The heated tile is fitted with a thermocouple to determine the temperature, and resulting photon flux emitted, which can then be compared to the flux recorded by the camera. The calibration on the vessel allows the determination of the emissivity and transmission effects generated by the graphite surface and optics [87].

3.2.7 Imaging

MAST is equipped with three high speed Photron APX-RS mega pixel cameras which are capable of imaging the whole plasma at speeds of up to 50kHz using a windowed view. The cameras can be used to follow the evolution of the plasma through the discharge or follow the collapse of the plasma during mitigation. The cameras can be mounted in sectors 2, 7, 10 or 12, with the sector 10 mounting being routine. The cameras can be fitted with remotely controlled filter wheels, into which up to six filters may be fitted to image certain wavelengths of light. The substantial quantity of radiation produced during disruption mitigation means that all of the cameras are fitted with a 0.9 neutral density (12.5% transmission) filter to cut down on the light collected and provide correctly exposed images. The camera views used during the disruption mitigation experiments can be seen in figure 3.12.

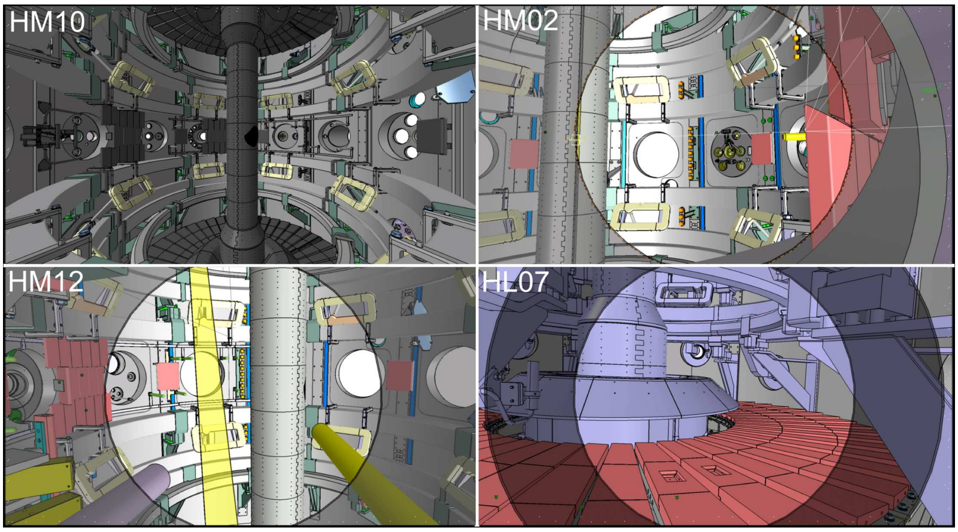

Figure 3.12: Disruption mitigation camera views. The gas injection is visible in the top left and lower right images with the lower right image showing the injection pipe in the lower left corner. (Images courtesy CCFE Design Office)

3.2.8 Summary

MAST is equipped with a wide range of diagnostics particularly suited to the study of unmitigated and mitigated disruptions. The open design of MAST allows for imaging of the whole plasma, which allows the plasma shape to be followed during disruption and the interaction of the injected gas to be follwed during mitigated disruptions. Infra red thermography provides coverage of all four divertor strike points for heat flux monitoring and energy balance when coupled with bolometer data. Finally, high resoultion Thomson scattering allows the study of plasma profile evolution during the mitigation via massive gas injection.

Chapter 4

Disruptions on MAST

Disruptions which have previously occured on MAST can be used to characterise key parameters in MAST such as the thermal quench timescales, current quench timescales, energy balance and operational boundaries [23]. The characterisation of unmitigated disruptions will allow comparison to mitigated disruptions in chapter 6.

4.1 MAST operational space

The operational space of a tokamak can be defined by two diagrams, the Hugill diagram as shown in figure 2.1 and the beta plot as described in section 2.1. The values required for these diagrams can be found at the time of the disruption by using the diagnostics available on MAST and the magnetic equilibrium reconstruction code EFIT [89]. The EFIT code is run on each discharge performed on MAST and provides reconstruction of the plasma based on the solution to the Grad-Shafranov equation [6, 7] using magnetic signals and optical measurements obtained from experiment. The EFIT run scheduled after each shot is available for all previous MAST discharges, and provides several of the required quantities for the operational space diagrams. The variables supplied by EFIT for the purposes of this analysis are, the edge safety factor (q_a), minor radius (a), major radius (R), the toroidal magnetic field on axis (B_{phi}), toroidal beta (β_T) and the dimensionless plasma inductance (l_i). The remaining quantities, the line average density (n), and the plasma current (I_p) are obtained from interferometry and Rogowski measurements respectively (see chapter 3 for details).

4.1.1 Thermal quench time

The thermal quench is thought to be brought about by the formation of MHD activity and the rearrangement of the flux surfaces within the plasma [31, 33]. The best method for determining the time of the thermal quench is to use a diagnostic which is dependent on the plasma temperature directly. The only diagnostic with sufficient time resolution on MAST is the soft X ray array. However, there are several complications to using soft X rays to determine the disruption time compared to the plasma current method. The first complication is that the soft X ray signal is low in ohmic discharges, due to the low plasma temperature, which makes the drop in the thermal energy less clear. In addition, it is not always the case that there is one clear, single thermal quench. Finally, the number of discharges with soft X ray data is lower than those with plasma current data, which decreases the number of discharges available for analysis.

However, an alternative method to determine the TQ time is available. As the TQ involves the rearrangement of the flux surfaces inside the plasma, this causes the inductance of the plasma to change. The change in inductance, coupled with the conservation of magnetic energy leads to the plasma current spike [6, 60]. Hence, it is possible to provide an estimate of the thermal quench time using the plasma current spike which has previously been used to study disruptions on MAST [90]. The procedure employed is shown in figure 4.1 and can be summarised as follows;

- The maximum gradient of the plasma current is found in the region where the plasma current exceeds 50kA (figure 4.1a)).
- A window around the maximum gradient is taken, and a window of 8ms duration is taken which is 2ms before the maximum gradient. These two regions represent the upward rising current spike region and the flattop in the plasma current prior to the current spike.
- A straight line fit can be made between these two windows and then the thermal quench time (t(TQ)) can be determined by using the intercept of these two fits (figure 4.1 c)).
- The plasma current is checked 5ms after the thermal quench time to ensure it has fallen to less than 50kA. This check is required to prevent the detection of internal reconnection events [34] as disruptions.

4.1.2 Operational space

The thermal quench time can be used to produce a Hugill diagram [28] for disruptions in MAST. To perform this analysis the various parameters required for the Hugill diagram detailed in section 4.1 are determined at the thermal quench time using EFIT data. The Hugill diagram can then be produced using a two dimensional histogram in terms of the Murakami parameter, nR/B_{phi}, and $\frac{1}{q_a}$ which is shown in figure 4.2.

Figure 4.2 shows the frequency of disruptions in a given region of the operating space of MAST. The regions in which MAST operates can be seen. However, the figure shows that the highest frequency of disruptions occurs within the centre of the

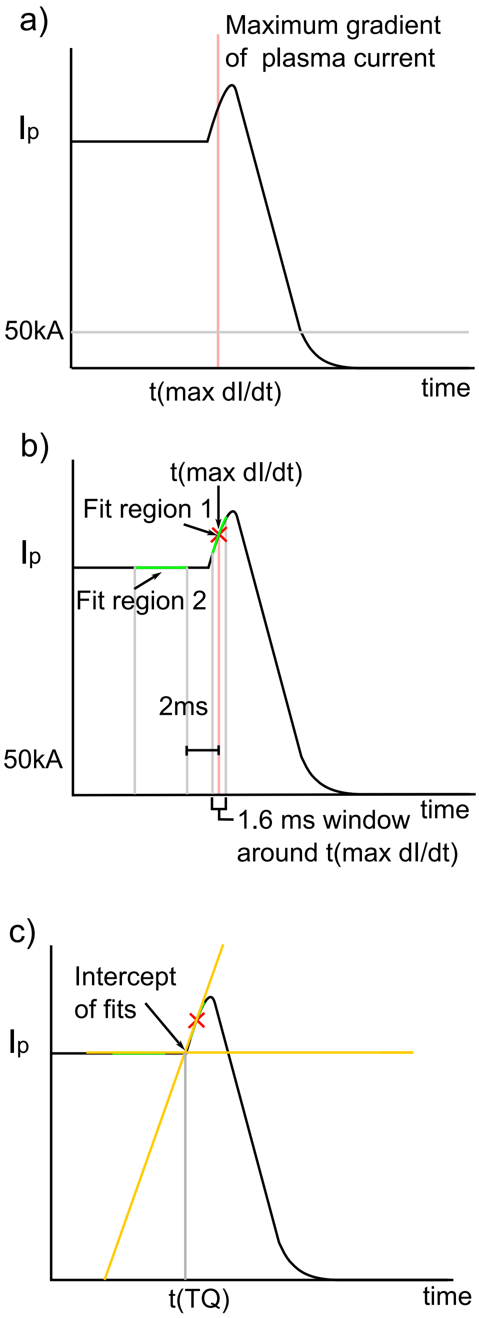

Figure 4.1: Determining the thermal quench time using the plasma current. a) First determine the location of the current spike using the derivative of the plasma current (red line). b) Define two regions (green lines) around the current spike to fit a line through each. c) The thermal quench time (t(TQ)) is defined as the intercept between the two fits (gold lines)

operating space where it would be expected that the plasma would be most stable. The reason for this apparent anomaly is that MAST operates in a certain region of the operating space more that others. Hence, the highest frequency of disruptions will occur in a region in which the highest number of discharges are performed. A more comprehensive analysis is required to reveal the operational boundaries.

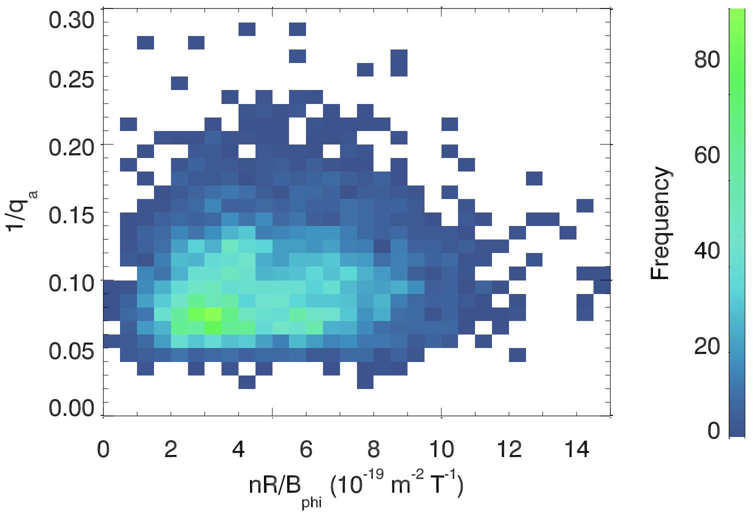

Figure 4.2: The frequency of disruptions in MAST operational space

4.1.3 Disruptivity

The normalised disruption frequency is known as the disruptivity, which was first suggested by de Vries [91], and has been calculated on JET discharges [91]. The disruptivity is the frequency of disruption normalised to the number of discharges which have been performed in a given region of operational space.

The disruptivity on MAST is determined by the follow the procedure, as set out in [91]. The analysis is performed by taking a MAST discharge and splitting it into 10ms time slices. The values of the various parameters required for the operational plots are then found in the middle of the time slice window. The time of the thermal quench can then be used to determine in which time slice the disruption occurs. The disrupting time slice uses the values of the plasma parameters at the time of the thermal quench instead of at the mid point of the slice, this is necessary as the plasma may have quenched prior to the middle of the window which would lead to parameters of zero.

Once the various plasma parameters have been obtained, the number of discharges in a given range of parameters x to $x + \delta x$ and y to δy can be found. The disruptivity can then be defined as in equation 4.1, where N_{tot} is the total number of time slices with plasma parameters in the range x to $x + \delta x$ and y to $y + \delta y$ and N_d is the number of disrupting time slices with plasma parameters in the range x to $x + \delta x$ and y to $y + \delta y$.

$$\text{Disruptivity} = D = \frac{N_d([x, x + \delta x], [y, y + \delta y])}{N_{tot}([x, x + \delta x], [y, y + \delta y])} \tag{4.1}$$

The analysis has been performed on all discharges on MAST, regardless of whether there is a disruption or the disruption occurs in ramp down, ramp up or flattop. Due to the reliance on EFIT reconstructions, the analysis of a given shot will start at 150ms and any discharges where the stored thermal energy at the current flattop returned by EFIT is less than zero are discounted. All values are obtained from the diagnostics listed above, with the exception of the edge safety factor which is replaced by q_{95}, as the value of the edge safety factor in devices with a separatrix can be approximated by q_{95} [14]. The analysis has been performed on 11631 MAST discharges, starting from discharge 3500 and concluding with discharge 22066. The reliance on EFIT for several of the parameters and omitting test discharges, reduces the total number of discharges available for analysis to 9800, of which 8019 are disrupting and 1781 are non disruptive.

The Hugill diagram which results from the analysis can be seen in figure 4.3 and clearly shows that the disruptivity increases toward the edges of the operational space. The figure shows the low q limit, with the disruptivity tending to one as $q_a = 0.5$ is approached, although there a few discharges which reach the theoretical limit of $q_a = 0.5$. The majority of discharges terminate with edge safety factors of less than 0.5. The Greenwald density limit can be seen along the lower edge of the plot, with the solid line corresponding to the empirical density limit $\bar{n}(10^{20}m^3) = I(MA)/\pi a^3$ [26]. As the Greenwald limit is derived for ohmic heated plasmas and MAST is capable of providing additional heating power, then it should be possible to exceed this limit. The enhanced limit brought about by the heating power available on MAST can be seen by the dashed line in figure 4.3 and a comparison of the expected limit and the MAST Greenwald limit can be seen in figure 4.4. The MAST density limit appears to be around one and a half times the Greenwald predicted limit [92], which would be expected with the addition of heat power from neutral beam injection. Figure 4.5 plots $l_i I_p / a B_{phi}$ against toroidal beta and illustrates the low q limit and the high beta limit. The low q limit is shown by the trend of increasing disruptivity as $l_i I_p / a B_{phi}$ tends toward four and the high beta limit is denoted by the dashed line, as discussed in section 2.1. The low q limit is shown as the means of increasing the abscissa values in figure 4.5 is to increase the plasma current, as the other factors are typically fixed by the design of the tokamak. Hence, with increasing plasma current and fixed toroidal magnetic field, the value of the edge safety factor decreases.

4.2 Disruption characterisation

Analysis of the disruptivity in MAST has shown that there are a significant number of disrupting discharges. A database of these disrupting discharges can be formed allow characterisation of unmitigated disruptions on MAST. The characterisation will allow the impact of mitigation to be assessed and comparisons to other tokamaks made.

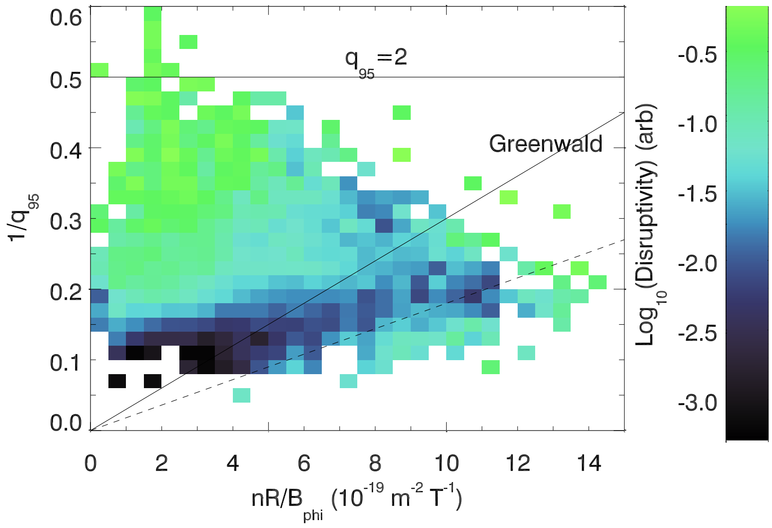

Figure 4.3: Hugill diagram for MAST derived from disruptivity analysis. The disruptivity is related to the probability of a discharge disrupting in a particilar region of operating space. The dashed line shows the density limit on MAST which is enhanced over the Greenwald limit via external heating.

4.2.1 Disruption database

The archive of MAST shots can be used to build a database of disruptions that are representative of high performance operation. Disruptions included in the database should satisfy a certain set of criteria which are as follows;

- Only disruptions which occur in the flattop of the plasma current will be considered as these are disruptions at full performance.
- Disruptions during ramp up or ramp down are not included as these may be triggered by operational reasons (e.g. current ramp rate) and not operational boundaries.
- If the discharge is externally heated via neutral beam injection (NBI), then the NBI must cease after the disruption.
- The central solenoid flux, which drives the plasma current, should not have reached its operational limit or started to ramp in the opposite direction. This would indicate that the plasma is moving out of flattop.

The criteria above have been applied to discharges 3500 to 22066 in the MAST database. The result of this analysis is a database consisting of 9864 discharges of which 8871 discharges disrupt at any point and 1122 discharges are full performance disruptions where EFIT has returned a stored thermal energy of greater than zero. The disruptions in the database have plasma currents between 200kA and 1.5MA with around 43% of discharges having a plasma current between 700 and 800kA.

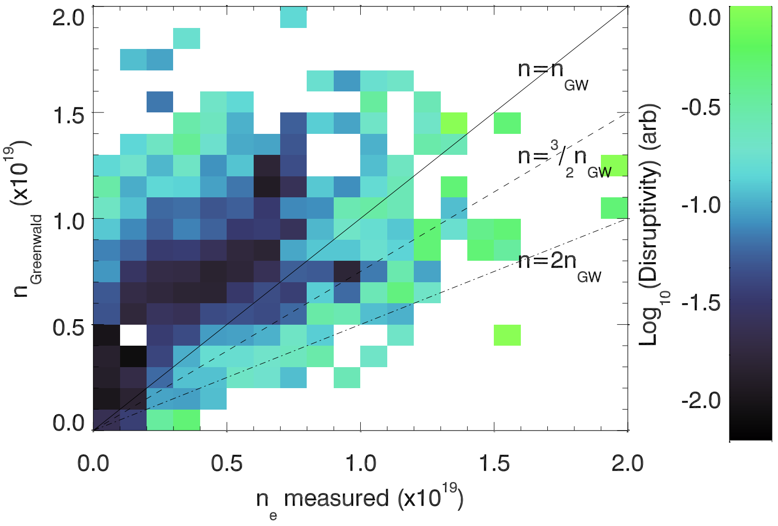

Figure 4.4: Comparison of the measured densities in MAST plasmas and the corresponding Greenwald prediction.

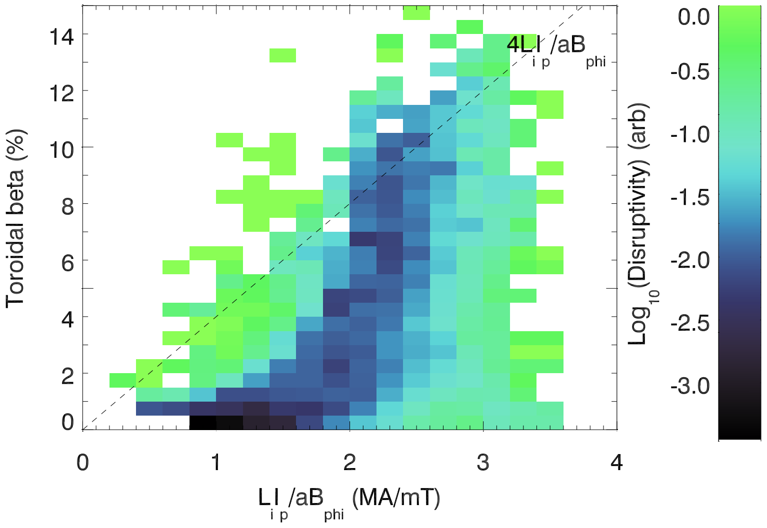

Figure 4.5: Illustration of the MAST beta limit as derived from the disruptivity analysis. The beta limit is shown as the dashed line and the low q limit can be seen as the abscissa values tend toward four.

A variety of timescales and characteristic parameters have been determined for each shot, from the timescales of the thermal and current quench, to the various parameters used in the disruptivity analysis. The parameters from the fitting code EFIT have been recalculated for all full performance discharges on a higher timebase at the time of the thermal quench. The use of the increased time resolution for EFIT runs is due to the scheduled EFIT data being on a 5ms timebase, which is longer than the typical disruption timescale on MAST. As a result, it can be the case that EFIT fails as the next 5ms time slice of the data has no plasma current. The repeated EFIT runs are performed at a 0.2ms resolution for four iterations around the thermal quench time. The following sections detail the physical properties of the disruption phases that can be analysed using the database.

4.2.2 Thermal quench

The thermal quench in ITER is expected to bring about large transient energy loads to the divertor which are significantly (3 to 10 times) above the melting/ vapourisation threshold for tungsten or carbon fibre composite. The estimate for the heat loads on the divertor surface during the thermal quench in ITER are based on several assumptions which have been developed from characterising disruptions on present day tokamaks [23]. The assumptions are based on the amount of energy remaining at the onset of the thermal quench, which is assumed to be 100% of the stored thermal plasma energy, the time scales over which the energy is deposited and finally the area over which the energy is deposited. The area over which the thermal energy is deposited is determined by the strike point width which typically expands during disruptions, it is assumed at present that ITER will seen a strike point expansion of seven times the steady state level [23] which is based on the results of infra red heat load analysis from a range of tokamaks.

Thermal quench timescales

The power load to the divertor during the thermal quench is determined by the magnitude of the stored thermal energy and the timescale over which it is lost. The thermal quench during a disruption can occur in a single stage or in multiple stages, which is dependent on the type of disruption (see chapter 2). The typical timescale for a thermal quench on MAST can be determined using the soft X ray (SXR) diagnostic as discussed in section 3. The determination of the thermal quench duration with the Thomson scattering system is not possible due to the rapid nature of the event (0.5-1 μs) compared to the TS temporal resolution (250Hz in continuous mode).

The thermal quench onset can be determined by locating a sharp decrease in the soft X ray signal around the time of the thermal quench as identified using the plasma current and detailed in section 4.1.1. By fitting a straight line through the thermal quench region of the SXR signal and through a 1 millisecond duration window of data 1 millisecond prior to the decrease, the onset of the thermal quench can be determined using the intercept of these two fits as shown in figure 4.6. The determination of a single or two stage thermal quench can be made by searching for multiple regions of steep decreases prior to the thermal quench, using the derivative of the SXR signal.

A two stage thermal quench can then be defined when two successive drops in signal are found within 8 milliseconds of each other. The disadvantage of using the SXR diagnostic to determine the onset of the thermal quench is that the signal is

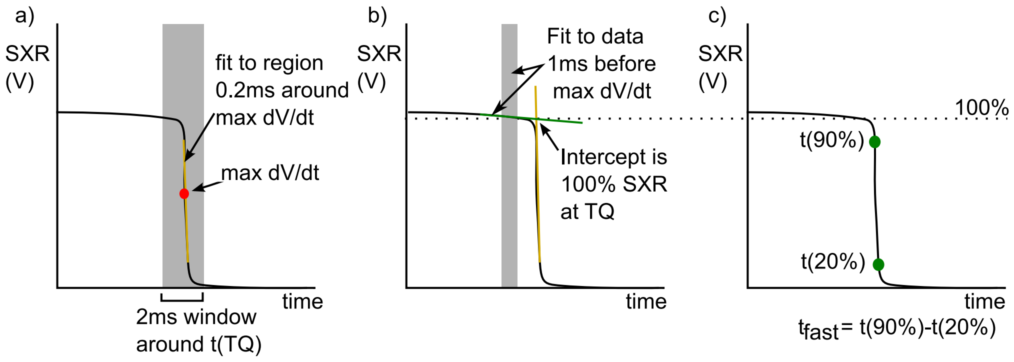

Figure 4.6: The thermal quench timescales can be determined using the SXR diagnostic on MAST. The procedure involves using the derivative of the SXR signal to locate the steep decreases around the time of the thermal quench identified using the plasma current.

often noisy, as a result of MHD activity within the plasma and the SXR signal can also be affected by the density and impurity concentration of the plasma. Discharges which undergo disruptions triggered by vertical displacement events (VDEs) also cause a decrease in signal on the central viewing chord of the plasma, as the plasma moves out of the field of view of the chord. Therefore, pure VDE discharges are not included in the thermal quench timescale analysis. The quality of the fits to the SXR data is assessed visually and any discharge where it is clear that the timescale is incorrectly determined is discarded from subsequent analysis.

The application of the thermal quench analysis to the MAST disruption database produces a modal timescale for the fast phase of the thermal quench of 0.3ms. The value obtained is consistent with the present linear scaling with minor radius, however, the distribution of the fast timescale is positively skewed and broad, leading to a standard deviation of the fast timescale of 0.4ms. The presence of the longer tail to the distribution is represented by the error in the calculated value, and is likely caused by the SXR signal being affected by factors other than the temperature of the plasma during the thermal quench, such as vertical motion of the plasma away from the viewing chord, or impurity influx.

The database returns several discharges in which there are two stage thermal quenches. However, the distribution of the global thermal quench timescale (time elapsed between first and second thermal quench) does not yield a well defined peak, which suggests that the derived global thermal quench timescale is not solely caused by the physics of the thermal quench but also encompasses additional processes taking place in the plasma. Upon closer inspection, the first thermal quench is generally caused by an H mode to L mode (HL) transition which occurs in MAST discharges prior to the disruption. The HL transition leads to a decrease in the plasma temperature which is supported by the decrease in the SXR signal over a timescale which is longer and more variable than that expected for a process determined by the loss of closed flux surfaces. Additional support for the two stage thermal quenches on MAST being generated by an HL transition is the number of L mode discharges which are detected as two stage thermal quenches. There are a total of 676 discharges analysed to determine the thermal quench timescale, of these 483 are L mode and 193 are H mode. Due to the absence of a well defined global thermal quench time, further analysis has been performed which shows that of the 483 L mode discharges around a dozen are two stage thermal quenches as compared to 41% of the H mode discharges. If the two stages of the thermal quench are caused by the collapse of different regions of the flux surfaces in the plasma, it would be expected that there should be no preference for H mode discharges over L mode discharges. The low number of two stage thermal quench discharges observed in L mode prevent an accurate value for the global thermal quench time to be determined for MAST. The updated machine scaling, following the addition of the MAST fast timescale can be seen in figure 4.7 (adapted from [32]).

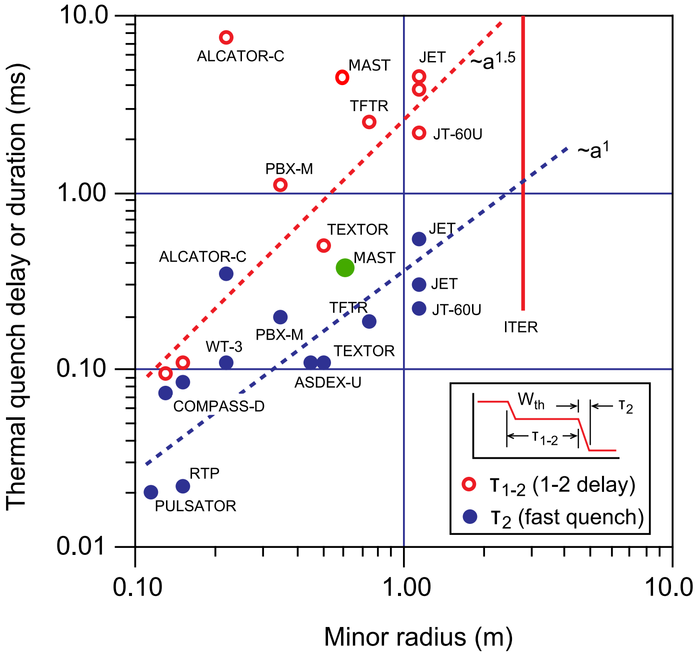

Figure 4.7: The variation of the global and fast thermal quench timescales for a variety of tokamaks including MAST. (adapted from [32])

Pre disruption thermal energy loss

The expected divertor heat loading in ITER is estimated using a number of factors. These factors include the area over which the energy will be deposited, the total stored thermal energy in a full performance discharge and the predicted timescale over which the energy loading will take place, as shown in figure 4.7. The total stored thermal energy in ITER is expected to be around 350MJ (Q=10 inductive scenario) [23], which is deposited on a timescale of 1 to 10 ms depending on whether the global or fast thermal quench phase is used to characterise the thermal quench. The resulting upper estimate of the heat load to the ITER divertor is between 144 and 446 MW $m^{-2}s^{-0.5}$, which relies on 100% of the pre disruption stored thermal energy being deposited in the thermal quench. The resulting lifetime of a carbon based divertor under these heat loads is between 100 and 1000 ITER pulses [93]. The expected disruption rate in ITER is expected to be around 10% [32, 94] with campaign lengths around 15000 discharges [32], hence there are sufficent disruptions to lead to the requirement of divertor replacement during the lifetime of ITER.

However, several machines [95, 96, 97] have shown that there can be a substantial reduction in the stored energy remaining in the plasma at the time of the thermal quench. The loss of stored thermal energy prior to the thermal quench occurs over a longer timescale. For example on JET, the pre disruption loss occurs over 80-20ms, compared to the 0.2 to 3.0ms timescale for energy to be delivered to the divertor [95]. The pre disruption energy loss on MAST appears to be associated with the growth of magnetic modes within the plasma as reported previously in [43, 96]. The growth of modes leads to confinement degradation in the period leading up to the thermal quench allowing the release of the stored thermal energy in the plasma to the divertor surfaces over much longer timescales.

The amount of stored thermal energy loss prior to the disruption can be characterised by using a ratio between the stored thermal energy at the time of the thermal quench to the maximum stored energy in the discharge. On MAST, the stored thermal energy at the disruption is determined using an EFIT reconstruction of the plasma at a 0.2ms time resolution during the thermal quench. The use of diamagnetic loops in spherical tokamaks to determine the stored thermal energy is not possible due to the large variation of the toroidal magnetic field across the plasma and comparable toroidal and poloidal fields which limit the accuracy of the technique [80]. The stored thermal energy at the onset of the thermal quench is then determined by interpolating between the two nearest time points returned from EFIT.

The maximum stored energy contained in the discharge is dependant on whether the discharge exhibits an H mode period prior to the disruption. The following criteria are used to determine the maximum energy;

- L mode discharges use the maximum energy returned from EFIT
- Discharges where H mode is lost within 30ms (one MAST confinement time, which is defined as the time for the energy to decay by $\frac{1}{e}$ of the original value) of the disruption also use the maximum energy returned from EFIT. This discharge is classed as an H mode discharge
- Discharges where H mode occurs prior to 30 ms before the disruption use the peak stored energy during the L mode period prior to the disruption. This prevents the maximum being overestimated due to the H mode phase which is unrelated to the disruption. This discharge is classed as an L mode discharge.

The analysis of the pre disruption energy loss is applied to 1696 discharges in MAST, of which 1406 are L mode discharges and 290 are classified as H mode discharges. The typical time between the loss of H mode and a disruption is 6ms, compared to the energy confinement time on MAST which is 30ms. Therefore, the stored energy at the time of the disruption will be similar to H mode levels despite the discharge actually disrupting in L mode. There are a handful of discharges (shown in figure 4.8) undergoing disruption in H mode. These shots can be compared to a typical H mode disruption where the H mode is lost prior to the thermal quench. It is clear from figure 4.8 that the H mode disruptions (18048 and 20501) exhibit little to no mode activity, as indicated by the quiescent Mirnov coil data. By comparison, the discharge where H mode is lost prior to the thermal quench (23447) shows significant mode activity, due to the presence of a neoclassical tearing mode in the plasma. The presence of MHD activity in beam heated discharges in MAST is typical and has been discussed in [98] and is thought to be due to the presence of a so called long lived mode.

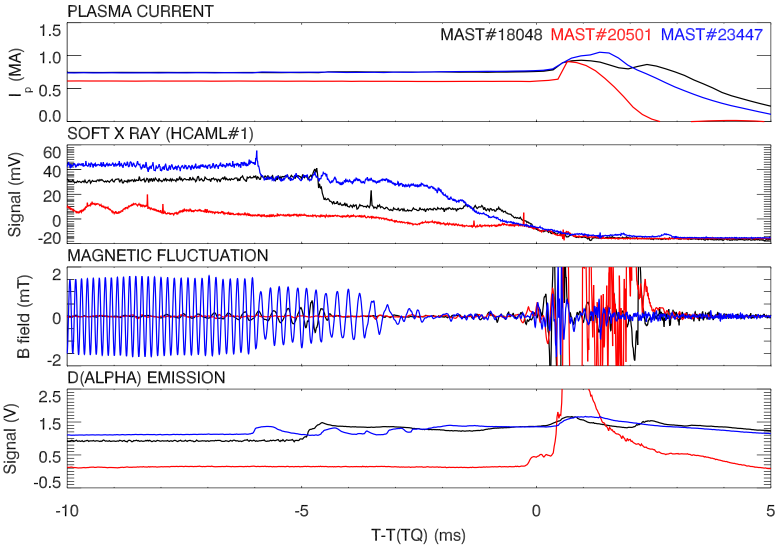

Figure 4.8: Comparison of disruptions in H mode. The discharges 18048 and 23447 are discharges in which the H mode period is lost prior to the disruption, as shown on the lower panel and corresponds to the growth or locking of a magnetic mode in the plasma. The discharge 20501 disrupts in H mode and exhibits no MHD activity prior to the disruption when compared to the other discharges. The origin of the MHD activity in 23447 is a neoclassical tearing mode and in 18048 it is the long lived mode (LLM) identified in [98]

The analysis shows that the mean energy remaining at the time of the thermal quench in all disruptions is 52%, with a broad distribution about the mean (σ = 25%). As a result of the large number of L mode discharges compared to H mode, the distribution for L mode shots is similar to that of all disruptions and is shown in figure 4.9a.

The results from MAST presented here shown a similar trend to studies previ-

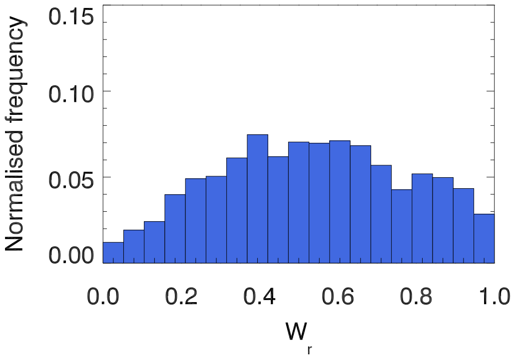

(a) L mode distribution

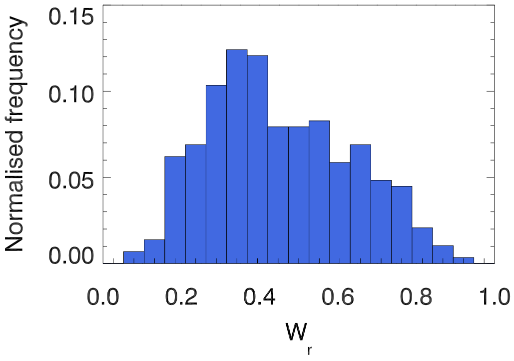

(b) H mode distribution

Figure 4.9: Ratio of stored thermal energy to maximum stored thermal energy at the onset of the thermal quench for (a) L mode discharges (1406 discharges) and (b) H mode discharges (290 discharges)

ously performed on MAST, which did not apply the constraints to ensure ensuring a full energy disruption [90], results from ASDEX (figure 4.10a) [96] and JET (figure 4.10b) [95].

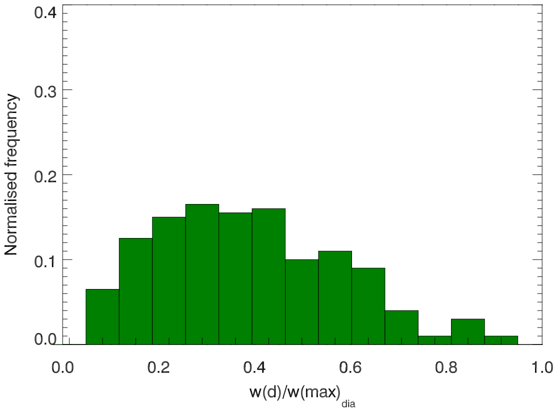

(a) ASDEX data

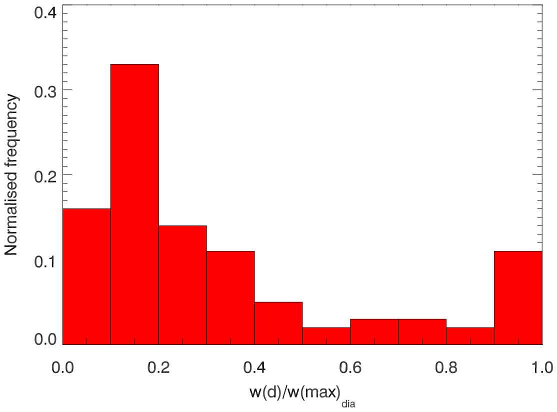

(b) JET data

Figure 4.10: Ratio of stored thermal energy at the onset of the thermal quench for ASDEX (taken from [96]) and JET (taken from [95]) for H and L discharges combined.

The analysis from MAST, JET and ASDEX shown that between 50 to 80% of the stored thermal energy is lost prior to the thermal quench, which is encouraging for ITER. However, there are also a number of disruptions which do occur at full energy, and as a result disruption mitigation will be a necessity in future devices.

Radiated and deposited energy

The total stored energy in the plasma prior to disruption is made up of two contributions. One contribution is from the thermal energy of the plasma and the second is the magnetic energy which is stored by the poloidal magnetic field. Whilst it has been shown that the loss of the stored thermal energy can occur over short timescales (approximately 500μs to 1ms), the magnetic energy is dissipated over a longer period of 2-4ms during the current quench. The magnetic energy is dissipated as a result of the increased plasma resistance brought about by the thermal quench. Ohmic heating of the post thermal quench plasma then allows the magnetic energy to be deposited onto the divertor or radiated from the bulk plasma.

The total energy contained within the plasma, prior to any loss due to the thermal quench, can be derived from EFIT reconstruction of the equilibrium. On MAST it is possible to monitor both the divertor power load using infrared thermography and the radiated power using a multichord bolometer.

The thermal quench time can be used to identify when in time the disruption occurs, allowing the energy dissipated from the plasma to be calculated via integration of the radiated and divertor power during the disruption. The balance between the total stored energy and the total energy lost during the disruption is shown in figure 4.11. The fit to the data shows that 91(±6)% of the stored energy can be accounted for by radiation and deposition onto the divertor. The error on the ordinate in figure 4.11 is derived by seeking to obtain a reduced chi squared fit of approximately one to the data points.

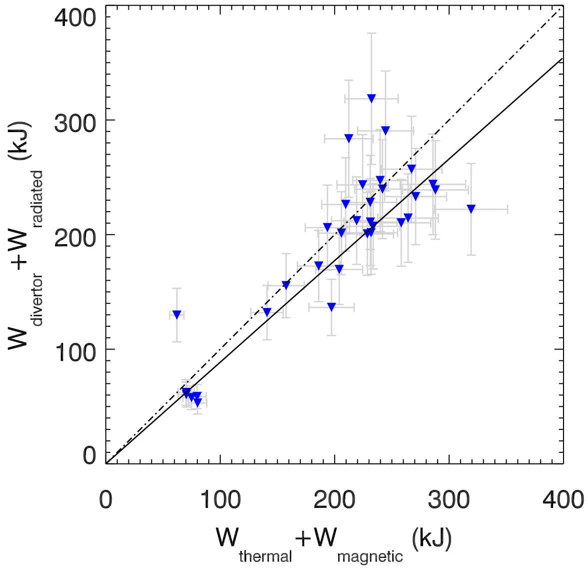

Figure 4.11: Comparison between the thermal and magnetic energy stored within the plasma prior to disruption to the energy delivered to the divertor and radiated over the plasma volume. The solid line show a fit to the data showing that there is a 91(±6)% accounting of energy and the dot-dashed line shows 100% accounting.

The division between energy delivered to the divertor and the energy radiated away during the disruption can be calculated using the bolometry and infrared camera data. The data shown in figure 4.12 shows that the majority of the total energy from the plasma ($W_{total} = W_{radiated} + W_{divertor}$) 82(±6)% is delivered to the divertor surfaces in MAST compared to the 8(±1.4)% of the total energy which is radiated during the disruption. The balance between radiated energy and divertor energy is important as increased radiation allows dissipation of the stored plasma energy over the whole plasma volume, leading to decreased divertor heat loads and extended divertor lifetime. The balance between radiated and divertor power is key to the operation of disruption mitigation schemes and the effect of mitigation on this balance will be assessed in chapter 6.

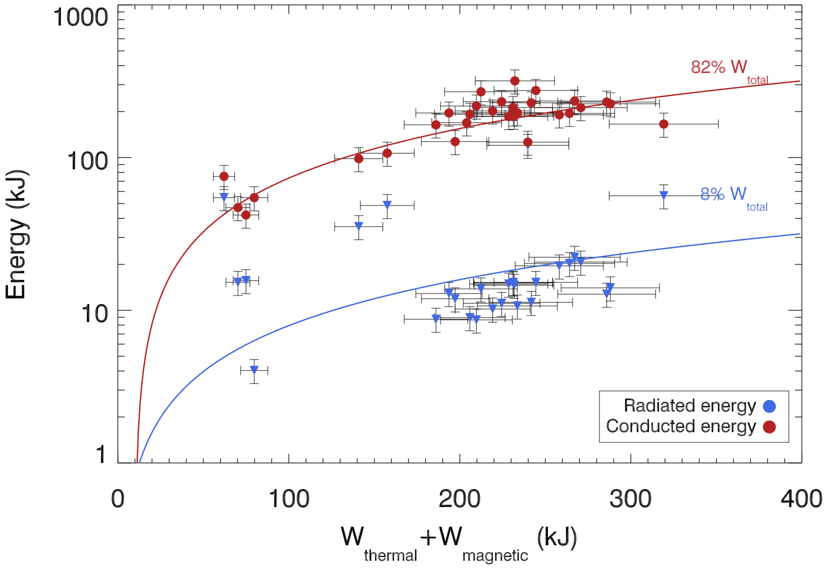

Figure 4.12: The balance between the radiated energy and divertor energy during disruptions as a function of total stored plasma energy. The energy delivered to the divertor (red circles) is significantly larger than that radiated (blue triangles).

The peak heat flux and width of the divertor footprint expands significantly during the thermal quench phase of the disruption compared to the steady state values. The expansion during the thermal quench suggests that there is enhanced transport across the field during the thermal quench phase, which could arise as a result of the destruction of closed flux surfaces into stochastic, chaotic surfaces [38]. Previous wide angle IR studies on MAST [43] have shown strong strike point braiding during disruption, lending additional support to the formation of stochastic surfaces during disruptions. The destruction of the closed flux surfaces will enhance cross field transport, thereby increasing the power load delivered to the divertor surfaces. The power load during a disruption on MAST is shown in figure 4.13 and clearly shows the significant increase in the power load along with a significant broadening of the strike point during the disruption compared to the steady state case. The loss of equilibrium during the thermal quench and current quench cause the loss of a well defined strike point.

4.2.3 Current quench

The rapid current quench can generate large electromagnetic forces on the vacuum vessel. These forces arise thorough the interaction of halo currents with the toroidal

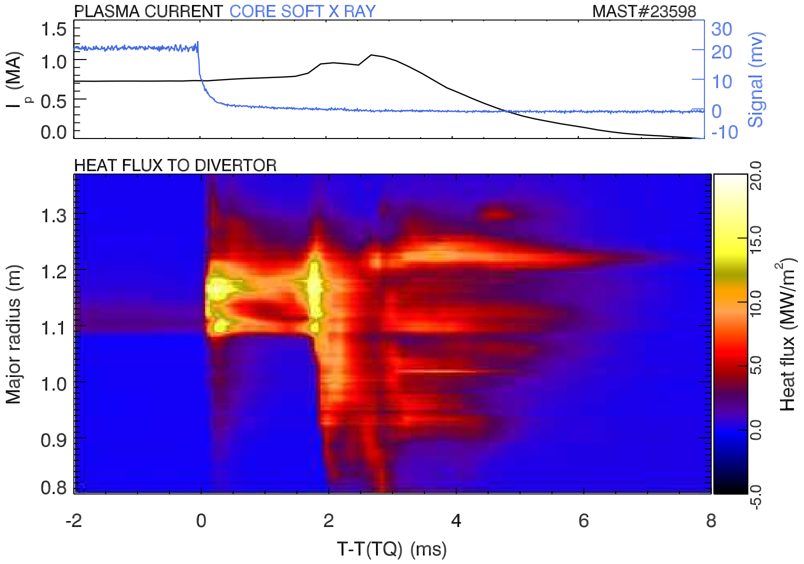

Figure 4.13: The heat flux to the divertor during a disruption on MAST. The power load and the strike point width can be seen to increase significantly at the onset of the thermal quench. The two distinct phases of high heat flux correspond to the thermal quench, followed by the loss of vertical control leading to a vertical displacement event (VDE).

magnetic field. It can also be the case that the halo currents produced during the disruption are not toroidally uniform, and as a result they can peak at a given toroidal angle. The peaking of the halo currents at a given toroidal location produces twisting forces on the vessel as the halo currents are not toroidally symmetric. Induced currents can also be produced during the current quench.

The current quench time on tokamaks is determined assuming a linear 60% decay time from 80% of the plasma current to 20% of the plasma current. The time scale for the 60% decay can then be plotted against plasma current. The current quench time and plasma current are normalised to the cross sectional area of the plasma to allow for extrapolation to ITER where the current and the current distribution are increased in size over present day machines [32].

The timescales for the current quench on MAST can be determined using the 60% time. The current quench times for all disruptions in the database can be seen in figure 4.14. As indicated by figure 4.14 the typical current quench time on MAST is between 1 and 3 milliseconds, however, the distribution is bimodal and skewed toward the upper limit of the current quench time of around 2.5ms. Further analysis of the current quench timescales suggest that the variation is caused by changes made to MAST during an engineering break in April 2004.

During the engineering break, several changes were made to MAST. These changes were as follows, firstly a longer central solenoid was added. Secondly, the divertor coils in MAST (P2 coils, see figure 3.2) were moved further apart and a new toroidally symmetric graphite divertor was installed [79]. In addition, the neutral beam system was upgraded to a JET style positive ion neutral injector from

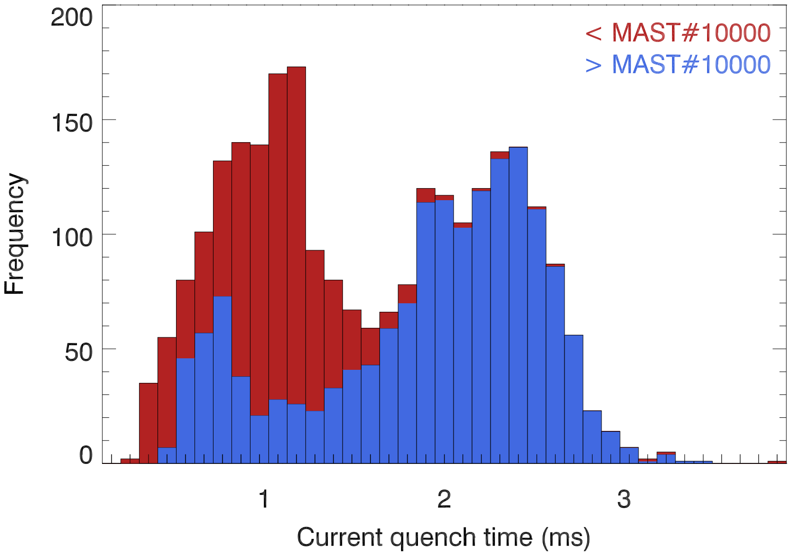

Figure 4.14: Current quench time scales in MAST for full performance disruptions. The distribution is bimodal, with typical current quench time scales of between 1 to 2 milliseconds. Discharges performed before the modifications to MAST in April 2004 (MAST#10000) are shown in red and discharges performed after are shown in blue

a previous Oak Ridge source, error field correction coils were added and a high field side gas puff was added [99].

The tokamak can be thought of as a system of coupled inductors, with the poloidal magnetic field linking the plasma current and the vessel structures. Such a system has a simple relationship between the resistance, R, of the plasma and the inductance of the system, L which can be used to give a characteristic current quench timescale, $\tau = L/R$ [23, 100, 101].

The simple equation for the current quench can be used to investigate the cause of the change in current quench time seen in figure 4.14. The effective inductance of a plasma can be determined using equation 4.2 as given in [100], where R_0 is the major radius, ϵ is the inverse aspect ratio and κ is the plasma elongation. The resistivity of a plasma can be derived using the electron collision time [6] which gives equation 4.3, where $K = 2.8\text{x}10^{-8}$, A is the plasma area, R_0 is the major radius, Z_{eff} is the effective charge of the plasma and T_e is the electron temperature in keV.

$$L_p^{eff} = \mu_0 R_0 \left[ln \left(\frac{8}{\epsilon\sqrt{\kappa}} \right) - \frac{7}{4} \right] \tag{4.2}$$

$$R = 2\pi R_0 K Z_{eff} A^{-1} T_e^{-\frac{3}{2}} \tag{4.3}$$

The parameters in equations 4.2 and 4.3, with the exception of the effective charge and the plasma temperature, can be combined together to evaluate their role in determining the current quench time in MAST. The temperature and effective charge cannot be included to allow a complete estimate for the current quench time as the diagnostics providing these measurements are not routinely available prior to April 2004. Figure 4.15 shows the value of $AR_0[ln(1/\epsilon\sqrt{\kappa})]$ against the current quench timescale on MAST.

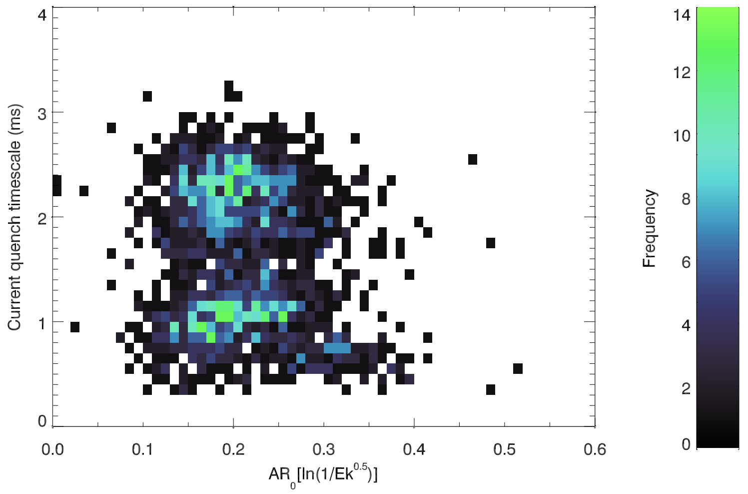

Figure 4.15: Current quench timescales against a product of elongation, area and radii of the plasma showing that the current quench time is not dependent on these quantities.

Figure 4.15 suggests that the underlying cause of the change in current quench time is the effective charge or the temperature. The sudden increase in current quench timescale shown in figure 4.14, coincident with the installation of a graphite divertor on MAST, suggests that the effective plasma charge has decreased. The improved divertor is toroidally symmetric, whereas the previous design consisted of raise ribs which shielded the steel vessel floor from plasma impact [79]. The decrease in effective charge will lead to decreased plasma resistance, and therefore an increase in current quench timescale which is consistent with the data obtained.

4.3 Summary

Analysis of the disruptivty has been used to located the operational boundaries in MAST. The analysis has shown the location of the beta limit, density limit and the low q limit.

A disruption database which includes high performance disruptions has shown that there is significant pre disruption energy loss. Typically the energy loss amounts to 50% of the maximum stored thermal energy. The loss mechanism for this energy is most likely the growth of MHD activity which is typical of MAST discharges. The energy lost during this phase is deposited onto the divertor surfaces, but over a longer period compared to the thermal quench phase of a disruption.

The loss of stored energy from the plasma occurs on timescales which are consistent with the present ITER scaling. Of the energy lost during the disruption, 80% is deposited onto the divertor surfaces with a further 10% radiated away. The 10% of unaccounted for energy could be deposited over the vessel walls, or is not detected due to broadening of the divertor heat flux outside of the infra red camera view (see chapter 7.2).

Finally, analysis of the current quench timescales have shown that there is a change in the duration of the current decay time after the installation of a new toroidally symmetric divertor. Analysis suggests that the decreased effective plasma charge is the cause of this change.

Chapter 5

The MAST Disruption Mitigation Valve

Disruption mitigation via massive gas injection relies on the ability to inject large quantities (10 to 100 times the plasma inventory) of impurity gas into the tokamak vacuum vessel in a short amount of time (1-2ms). In addition to the requirements on speed and volume of injection, it is also necessary for the valve to be capable of operating in areas where there are high magnetic fields. This chapter describes the components, design and operation of the MAST disruption mitigation valve (DMV).

5.1 Disruption mitigation valves

In order to achieve the injection of 10-100 times the plasma inventory, a high capacity fast acting valve is required. There are several designs [58, 62, 102] of disruption mitigation valve, using a variety of techniques for operation from piezoelectric actuation [59] to eddy current actuation [53].

The disruption mitigation valve used on MAST is an eddy current actuated valve, as used on TEXTOR and most recently on JET. The valve, developed at Forschungszentrum Jülich (FZJ), was chosen for use on MAST as a result of the experience already gained installing the valve at JET and the availability of a suitable valve from FZJ.

5.2 MAST Disruption Mitigation Valve (DMV)

The valve is shown in 5.1 and consists of four main components, the piston, pancake coil, front and rear plena. The front and rear plena are separated by the piston, which controls the opening and closing of the front plenum. The front and rear plena are supplied with gas from two separate inlets located on the side and the rear of the valve respectively. The total length of the valve is approximately 300mm, with a diameter of 170mm. The connection of the valve to the vacuum vessel is made by a 63mm flange. The MAST DMV is pictured in figure 5.2 [103].

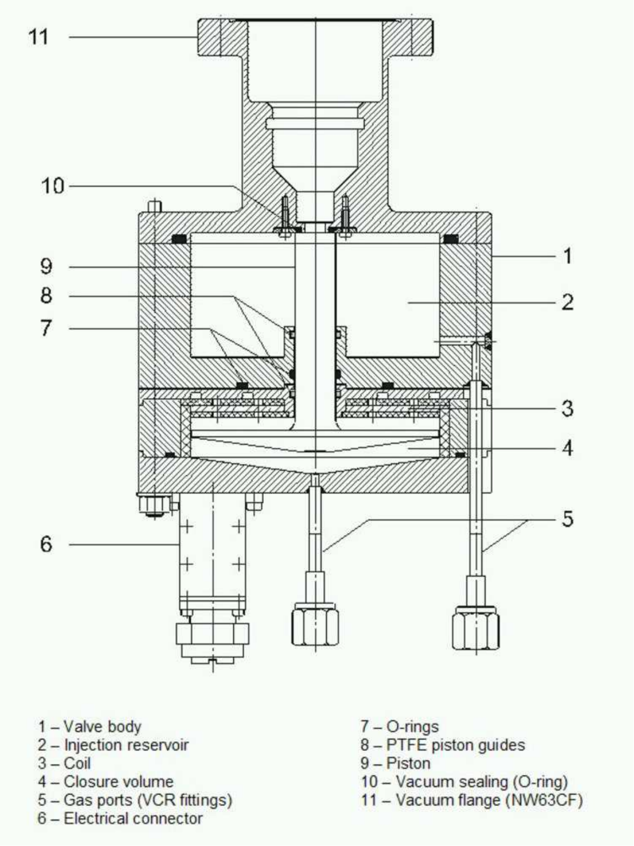

Figure 5.1: Schematic of the FZJ disruption mitigation valve

The valve is constructed from stainless steel and aluminium, and is composed of three main components which are connected together through the length of the valve. The rear of the valve, and vacuum connection can be removed from the valve. However, the pancake coil, piston and housing are held together in one unit by the design of the piston. The piston in the rear plenum volume does not have a gas tight seal between the valve chamber and the piston head. The seal between the sections of the valve; the piston and the valve body and front plenum volume is achieved using O rings between each section. The front plenum of the valve has a capacity of 275 ml and the rear plenum has a volume of around 200 ml. The individual components of the valve can be seen in figure 5.3 [103, 104].

5.2.1 Operation

The opening time of the valve is determined by two factors, the current driven through the pancake coil and the pressures in the valve plena. The rear plenum pressure determines the opening characteristics of the valve and provides a force to seal the front plenum. The basic operation of the valve is that the plena are pressurised (figure 5.4A), and a current pulse is passed through the pancake coil. The current driven in the pancake coil induces eddy currents in the valve piston, which forces open the piston against the pressure in the rear plenum. The rear

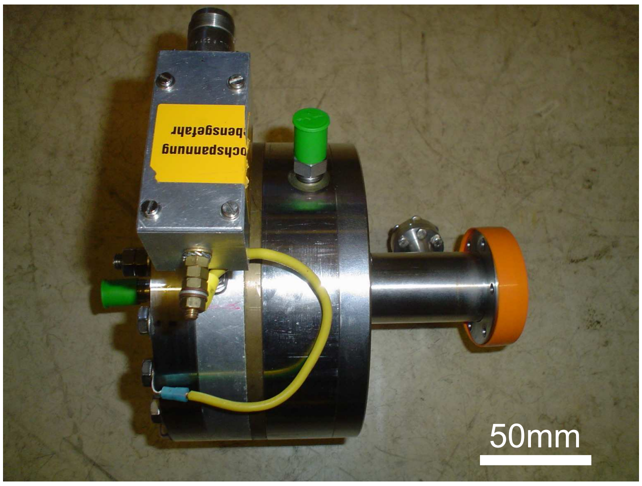

Figure 5.2: The MAST disruption mitigation valve

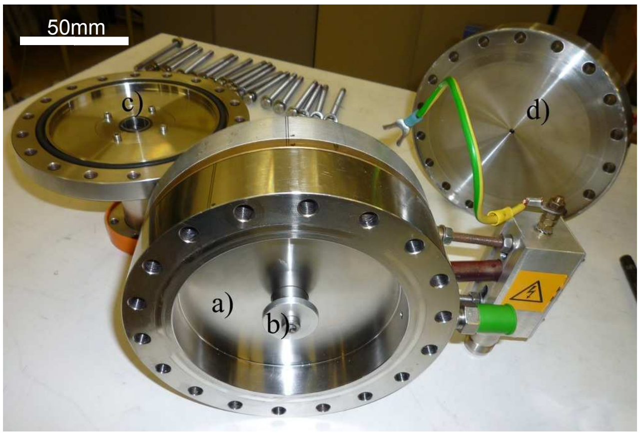

Figure 5.3: MAST DMV components. a) shows the injection plenum, b) shows the pistion and injection plenum seal, c) is the valve outlet and connection to the vacuum vessel and d) is the valve back plate.

plenum pressure then acts on the piston, and provides a restoring force, pushing the piston closed once more (5.4B) [53, 104]. The delay between the triggering of the power supply and the opening of the valve has been determined experimentally to be 0.5ms [53].

The result of the rear plenum pressure being used to seal the injection plenum is that the rear plenum must be pressurised prior to the filling of the injection plenum. The pressure in the rear plenum must be sufficient to prevent the pressure in the injection volume forcing the piston open, and this condition is determined by the areas over which the pressures act. In initial valve designs, [53, 103], the requirement for valve closure was $P_{injection} = 1.4P_{rear}$ which is determined by the areas of the piston stem seal (item 10 on figure 5.1) and the valve exit seal (item 7 on figure 5.1). The increased rear plenum pressure provides a larger restoring force to the piston, causing it to close more quickly. By increasing the output orifice from 10mm to 20mm and making the sealing area at the valve exit seal and the piston stem

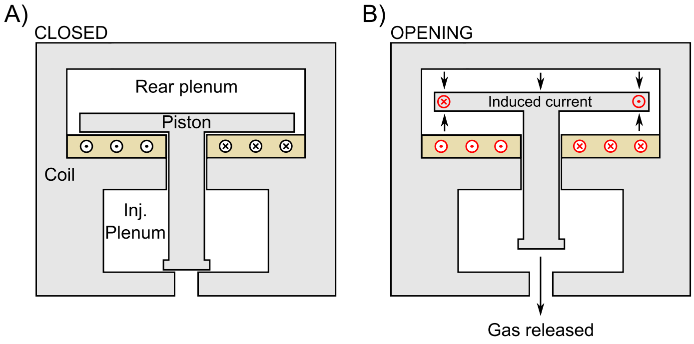

Figure 5.4: Illustration of the operation of the DMV. The plena are charged with gas in A. A current is then pulsed thorough the coil in B. The current induces eddy currents in the piston which push the piston open against the pressure in the rear plenum, thereby opening the valve output orifice and injecting the gas.

the same area, leads to a reduction in the pressure required in the rear volume to 4 bar for all injection plenum pressures. It is the decreased rear plenum pressure and the increased outlet size which enhance the efficiency of the MAST DMV over the JET valve [104]. The gas species used in the rear plenum also affects the opening characteristics of the valve. The use of high mass gases produces small opening distances and rapid closing times, which limit gas throughput. The reason for this behaviour can be understood by considering what happens to the gas in the rear plenum when the piston is actuated. Initially, all of the gas in the rear plenum acts to force the piston closed; however, as the gas in the plenum is compressed by the piston, a void is formed under the piston head. The absence of a gas tight seal between the piston and the chamber walls allows gas to fill the void behind the piston. The pressure acting to close the piston decreases as the gas fills the void, leading to longer closing times than would be expected if a gas tight seal existed. Therefore, high mass gases, which have low thermal velocities will not fill the void behind the piston as quickly as a low mass. The result of this is an increased pressure acting to close the piston in the case of a high mass gas compared to a low mass gas. Hence, low mass gases in the rear plenum will produce larger opening distances and longer opening times than compared to high mass gases [53]. The best choice of gas in the rear plenum is found to be helium [53] which gives good opening distances and a longer open time than heavier gases.

Experimental evidence [104] shows that the valve produces a pulse of gas which travels at the sound speed. The pulse has a well defined shock front which smears out in time as the gas propagates along a tube of 40mm diameter. However, the gas pulse is still sharp and well defined after propagation along a 4 metre tube [104] which is encouraging for MAST where the distance to the plasma edge will be approximately 2 metres. A typical time history of the density delivered from the valve using a 25 bar helium fill can be seen in figure 5.5 which is taken from [104], page 7, for illustrative purposes.

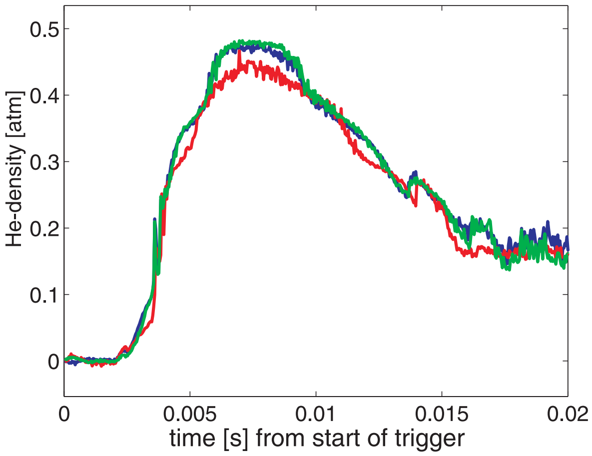

Figure 5.5: Gas flow of the JET DMV performed by [104]. The time history of the density was measured interferometrically at the end of a 40mm diameter, 4 metre long pipe. The three traces correspond to three repeated measurements. A 10mm outlet DMV (JET style) was used with a helium injection fill pressure of 25 bar. (figure adapted from [104], page 7)

5.2.2 Injected gas quantity

The requirement for disruption mitigation, in terms of injected quantity of gas, is difficult to determine. The tokamaks equipped with disruption mitigation inject various quantities of gas, from around 2-7 times the plasma inventory in ASDEX-Upgrade [59] to around 100 times the plasma inventory on DIII-D [41]. A consideration for MAST, unlike other tokamaks, is that it does not have a close fitting vessel wall. Hence, it may be necessary to inject more gas than in other devices to achieve a similar vessel pressure. In addition to the consideration of how much gas is required for effective mitigation, it is also necessary to define a safe level of injection on MAST to ensure that there is no damage to pressure sensitive diagnostics, such as ion gauges, bolometers or vacuum pumps. The estimation of the upper limit of particles in the vessel can be obtained from plasma density and neutral pressure measurements made during the lifetime of MAST. These measurements show that discharges in MAST typically exhibit electron densities of around $3\text{x}10^{20}\text{m}^{-3}$ and upper vessel pressures achieved equate to around $3\text{x}10^{21}$ particles in the vessel. The process of glow discharge cleaning on MAST, which is performed inter-shot, raises the pressure in the MAST vessel to the 10^{-2} mbar level, which corresponds to a particle inventory of approximately 10^{22} particles. It is clear from these considerations that is should be possible to inject at least 10 times the plasma inventory into the MAST vessel for disruption mitigation without any additional requirements to protect individual diagnostics, such as isolating high voltage filaments or protecting diagnostics behind gate valves.

The quantity of gas which can be injected is determined by the pressure and volume of the injection plenum, therefore, it is necessary to determine a suitable plenum volume which will be capable of injecting around 100 times the plasma inventory, assuming a 95% valve efficiency. The resulting injection plenum volume was set at 65ml; giving the scope for increasing the injected quantity by raising the plenum fill pressure as necessary. The reduction in volume of the injection plenum is performed by machining an insert which sits inside the injection plenum.

5.3 Disruption mitigation valve ancillary components

The disruption mitigation valve forms one part of the DMV system. There are several ancillary components, these include the connection between the valve and the vacuum vessel, the power supply to trigger the valve, the control system and the gas supply to the valve.

The MAST DMV is mounted on a midplane vessel port which is located in sector 12. The port stands around 1.8m from the floor level in the MAST machine area, and as a result it is necessary to build a support structure to contain the DMV and ancillary equipment. The design of MAST, without a close fitting wall, means that the vessel port onto which the DMV will be attached is located 0.9 metres from the plasma edge. To ensure the injected gas is delivered to the plasma edge effectively, the DMV is mounted onto the end of a 1.5m, 50mm diameter pipe which can be inserted into the vacuum vessel and positioned to within 30cm of the midplane outboard separatrix. The pipe can be retracted from the vessel and the gate valve closed when the system is not in use, thereby preventing the release of any impurities contained in the valve during standard operations. The support frame also houses the gas system which supplies the front and rear plena.

Figure 5.6 below shows a cut away of the connection between the vacuum vessel and the DMV. The pipe through which the gas is delivered is supported at the DMV end on a mount built into a translation stage. There is also a support at the point where the pipe passes into the vacuum vessel, which is constructed of plastic and machined to allow pumping of the trapped volume. The DMV pipe is constructed of two sections, one 800mm long composed of stainless steel and a 600mm section manufactured from ceramic. The ceramic section is inserted into the vacuum vessel and is manufactured from an insulator to guard against halo current formation should there be interaction with the plasma edge. The DMV assembly is also electrically isolated from the vacuum vessel using two ceramic breaks, one at the connection to the MAST and one at the DMV pipe to DMV connection.

The vacuum connection and translator unit are mounted into the DMV support frame, this allows the gas panels and vacuum pumps to be housed in the lower half of the framework which can be seen in figure 5.7. The details of the gas system and other components will be detailed in the following subsections.

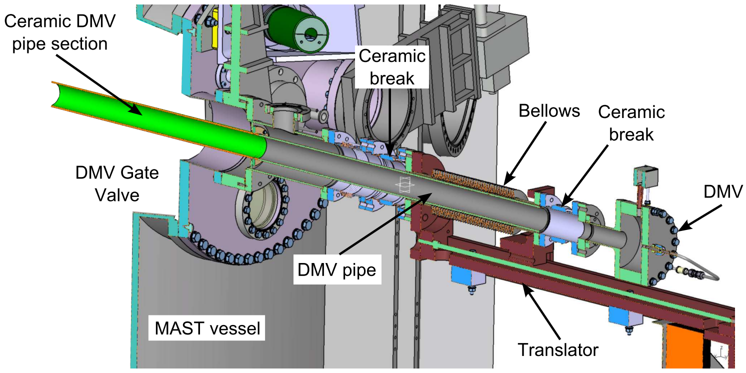

Figure 5.6: The disruption mitigation valve vacuum connection to the gate valve on sector 12. The DMV is shown on the right attached to the translator which allows the retraction and insertion of the pipe into the vacuum vessel

5.3.1 Gas system

The operation of the MAST DMV requires the supply of gas at pressures of up to 30 bar to the front and rear plena of the valve. The standard MAST gas system, used for fuelling, is rated to 5 bar and modification of the standard system would impact operations. The use of noble gases only in the MAST DMV allows the use of a local high pressure gas system housed in the DMV support frame. In addition to supplying the gas for valve operation, the gas system must also enable the vacuum connection to be pumped down and the gas lines and DMV to be pumped out.

The gas system design is shown in figure 5.8 and is composed of two sections, the main gas panel which is housed beneath the vacuum connection and the DMV panel which is attached to the side of the DMV. The two panels are connected together using a flexible hose which allows the translation of the DMV into and out of the vessel. The use of two panels allows the valves which isolate the plena to be located near to the valve and prevent the need of a separate gas line for each plenum. The main panel provides the connection of the gas system to the gas cylinders and the ability to connect the gas panel to the vacuum pump. The main and secondary panels are equipped with three pressure transducers, one on the main panel and two on the DMV panel to monitor the system and plena pressures.

The filling rate of the plena is controlled by a metering valve located on the main gas panel. The metering valve allows the flow rate of gas to be sufficiently slow that the plena fill to 5 bar in around 2-3 minutes with a regulator pressure of around 7 bar.

The DMV gas system valves are pneumatically actuated, with a normally closed indicator to allow the valve status to be relayed to the control system. Figure 5.9 shows the main gas panel, pneumatic gas lines for control valve actuation and the location of the vacuum pump in the lower support frame.

The main gas panel allows the connection of up to four gas cylinders which have a fill pressure of 68 bar and a capacity of 110 bar litres. The cylinders can be supplied

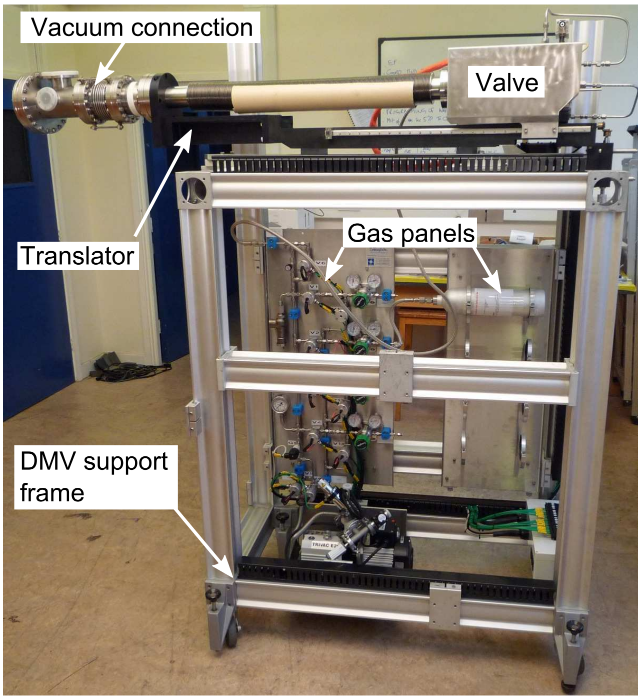

Figure 5.7: The disruption mitigation valve system showing the gas system, vacuum connection and the vacuum pumps. A turbo pump (not shown) and vacuum gauge will be fitted onto the blanked flanges at the top left of the image.

premixed with different noble gas mixtures, or pure mixtures can be obtained. The gas volume in the cylinder will allow operation of the DMV for approximately five full operational days, or equivalently around 100 MAST discharges.

The DMV panel is shown in figure 5.10 and is attached to the DMV translator. The panel delivers gas to each plenum via separate, electrically isolated gas lines. The pneumatic lines, control cables and flexible connection to the gas panel are routed through a flexible trunking attached to the translator unit and the DMV, as shown in figure 5.10. The injection and rear plenum are also protected by pressure relief valves to prevent overpressure in the valve plena which could arise from regulator failure.

The vacuum system allows for pumping of the main vacuum connection and the ability to rough out the gas system if the injection species is changed.

5.3.2 Power supply

The actuation of the valve requires a current pulse to be delivered to a pancake coil within the DMV as shown in figure 5.4. The current to be delivered to the coil is around 1.5kA with a full width half maximum of around 0.6ms [103]. The power supply for the MAST DMV was constructed in house and features several interlocks and outputs which allow the supply to be triggered and monitored remotely. The design is based around a 300 μf capacitor bank charged to around 2kV which is fired using a silicon controlled rectifier (SCR). The firing trigger is supplied via fibre optic

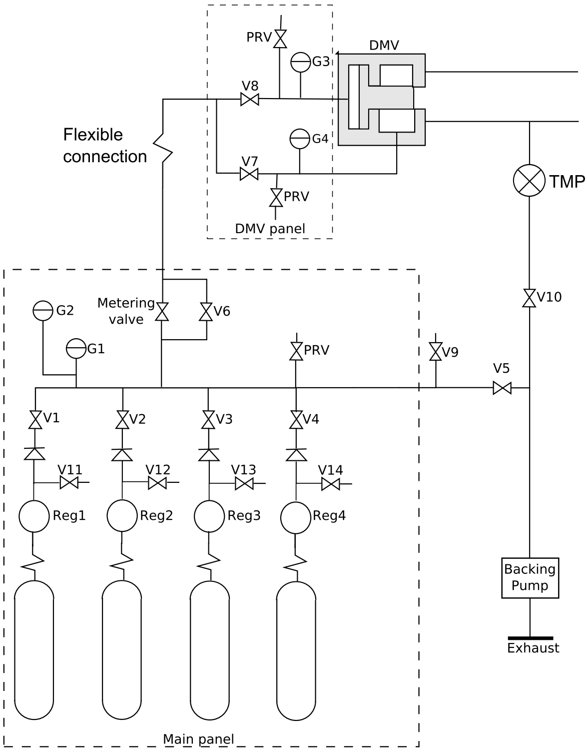

Figure 5.8: DMV gas supply system. The gas system consists of two panels, the main panel located in the support frame and the DMV panel which is attached to the DMV mount on the translator. The flow through the system is controlled by the metering valve on the main panel. The turbo molecular pump (TMP) for evacuating the vacuum connection is shown and backed by the backing pump.

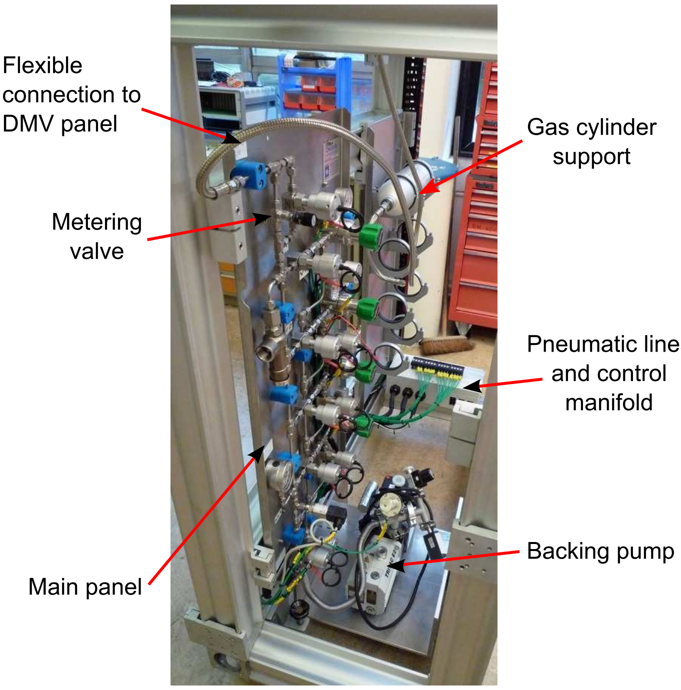

Figure 5.9: Main DMV gas panel with additional items shown.

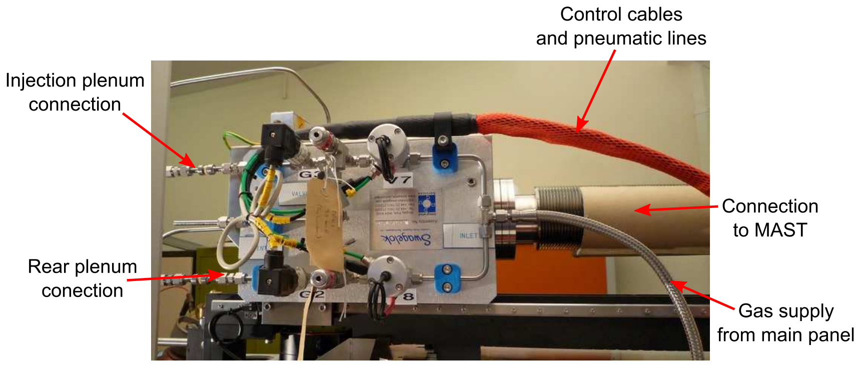

Figure 5.10: DMV gas panel with additional items shown.

input and is delivered from the MAST Plasma Control System (PCS). The power supply (figure 5.11) is housed in a cubicle in the MAST area with a connection between the valve and the power supply being made with a 25 metre long high voltage cable.

Figure 5.11: DMV power supply located in 19 inch cubicle. The front panel shows various status indications and interlock connections. The red, green and yellow lights (lower left corner of image) indicate the presence of mains power, the presence of the control system enable and the start of charging respectively.

The various connections on the power supply can be seen in figure 5.11. The connections allow the input of a control system signal which enables the supply, and returns monitoring of the charge state. These are supplied via a six pin LEMO connector. The connector to the right of the LEMO is for monitoring of the current output from the supply. The current delivered to the coil from the supply is measured to be around 800A, which is less than the design specification, however, the valve actuates as expected. The remaining connectors allow the PCS trigger to be sent to the supply and the provision for interlocking with the neutral beam injection system.

5.3.3 Control

The operation and monitoring of the DMV system must be performed remotely during the operation of MAST as there is no manned access during operations. The filling, pumping and firing of the valve is controlled remotely from the MAST control room using a control interface (figure 5.12). In order to achieve this, the DMV system is integrated into the MAST Vacuum and Gas control system. The control interface allows control over the valves in the gas panel, the status of which are returned to the control system using position indicators fitted to the valves. The operation of the valves is currently performed manually, with the operator selecting the necessary valves to supply gas to the plena. However, the filling of the valve plena (operation of valves V7 and V8 in figure 5.8), is performed automatically based on a defined pressure set point being reached. The charging voltage of the capacitor bank is monitored and recorded by the MAST data acquisition system. The signal returned shows high when the capacitor charge voltage is at 2kV and zero when it falls from this level. The charge signal is used to determine the precise firing time of the supply, allowing the time between the firing of the supply and the trigger being sent via PCS to be determined (0.5ms).

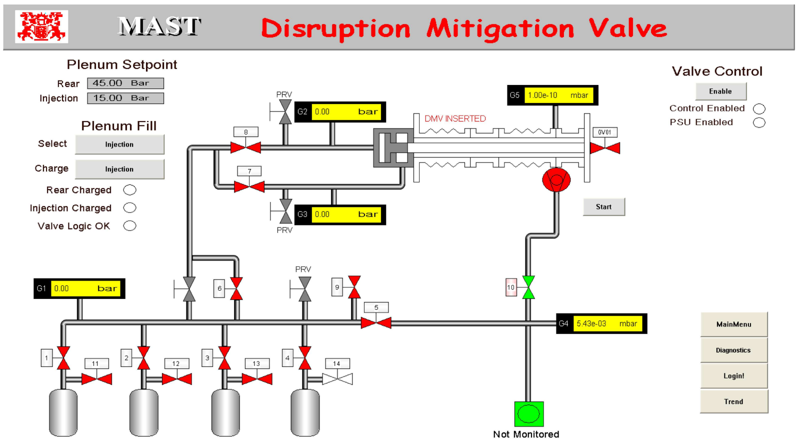
Plenum Setpoint
Rear 45.00 Bar
Injection 15.00 Bar
Plenum Fill
Select Injection
Charge Injection
Rear Charged ○
Injection Charged ○
Valve Logic OK ○
Valve Control
Control Enabled ○
PSU Enabled ○
G1 0.00 bar
G2 0.00 bar
G3 0.00 bar
G4 5.43e-03 mbar
G5 1.00e-10 mbar
DMV INSERTED
Not Monitored

Figure 5.12: DMV control system screen

5.3.4 System protection

The firing of the DMV into the vessel when neutral beam heating (NBI) power is being applied may have undesirable consequences for the NBI system. The resulting high vessel pressures could lead to the deposition of beam power on to the surfaces of the beam line, leading to damage. The DMV is prevented from firing by the plasma control system (PCS) if the NBI system is operational. The PCS checks for a signal indicating that the beams are on 15ms prior to the chosen DMV trigger time. If the PCS detects applied beam power, the DMV trigger will not be sent to the supply, preventing the firing of the valve. The 15ms delay is required to ensure that the beam power has been isolated and is caused by the hardware used to control the NBI system.

5.3.5 DMV calibration

The amount of gas injected can be determined by firing the DMV into an empty vacuum vessel. In order to perform a gas into vacuum calibration, all of the gas fuelling is turned off and all vacuum pumps are isolated. The resulting pressure increase in the MAST vessel, coupled with the change in DMV injection volume pressure can then be used to determine the number of particles injected into the vessel.

The volume of the MAST vacuum vessel is 50 cubic metres and the volume of the DMV injection volume can be calculated from engineering drawings to be 65ml. The pressure measurement on the DMV injection volume is performed using a Swagelok piezoelectric pressure transducer which reads from atmosphere to 68 bar(g), with an error of 2%. The efficiency of the DMV is calculated by the amount of pressure remaining in the plenum after firing compared to the initial fill pressure. The DMV is not 100% efficient, therefore, not all of the initial fill pressure is exhausted during the firing of the valve. The actual quantity of gas injected must be determined by subtracting the pressure remaining in the DMV injection volume from the initial fill pressure. The efficiency of the MAST DMV can be determined by plotting the DMV injection plenum fill pressure versus the pressure change in the injection plenum as shown in figure 5.13. The efficiency of the valve is found to be 76[±2.6]%, which is consistent with the values quoted in [104].

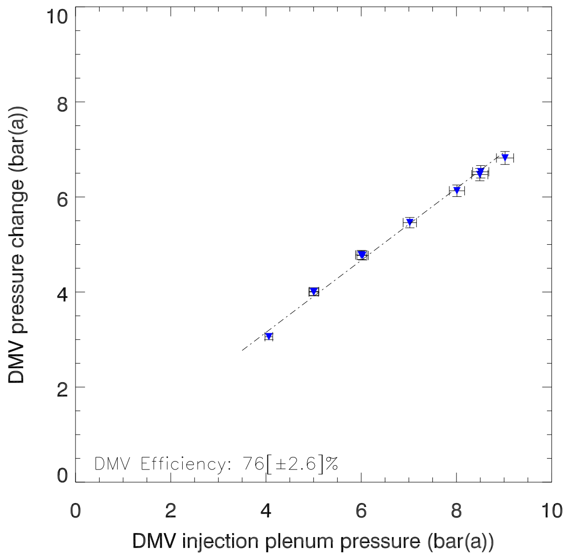

Figure 5.13: The abscissa is the fill pressure of the DMV system prior to firing and the ordinate is the drop in pressure in the injection volume after firing.The linear fit to the data gives the efficiency of the valve.

The pressure increase during the injection can be monitored using the torus vacuum gauge (TG1) which is located in sector 7 of the MAST vessel. The vacuum gauge TG1 is an MKS Instruments Quattro 999 gauge and is a composite vacuum gauge consisting of a piezo, Pirani and ionisation gauge. The pressure range which can be measured using the gauge is from atmosphere to 10^{-9} mbar, however, the typical pressure reached during injection is in the 10^{-3} to 10^{-2} mbar range which is measured using the Pirani component of the vacuum gauge. The Pirani gauge is calibrated in nitrogen, hence it is necessary to convert the measured pressure into the majority species injected (helium) by using a gas correction factor. The pressure gauge used for the measurements applies the correction factor as part of the internal software, hence, it is not possible to correct after the measurement has been performed as the correction factors are not available. However, the gas correction factor for various Pirani gauges have been determined in [105], the gauge VM3 in this paper is of the same type as that used in the TG1 gauge, hence the correction factor has been taken to be 1.2. The actual pressure, P, in the system is determined by using the measured pressure, $P_{measured}$, multiplied by the correction factor, hence $P = 1.2 * P_{measured}$.

The comparison between the injected quantity from the DMV (injection fill pressure minus pressure remaining after injection) and the pressure rise in the vessel can be performed by plotting the inventory delivered by the valve and the inventory increase in the vacuum vessel. It can be seen in figure 5.14 that there is good accounting between the pressure rise and the inventory delivered by the valve, with a mapping of one to 1.13. The possible sources of error in the plot arise from inaccuracies in the total injection plenum volume, MAST vessel volume, temperature variation or pressure gauge error. It can also be seen that there is a systematic error in the fit, which could arise from inaccurate calibration of the TG1 gauge or incorrect calibration factor.

The calibration of the injected quantity requires a relationship between the fill pressure of the DMV injection plenum and the corresponding number of particles injected into the vessel. The relationship between these quantities is shown in figure 5.15. The chart shows the injected number of particles calculated using TG1 (blue circles) and those calculated using the plenum volume and pressure (red triangles), $N_{inj} = (2.42\text{x}10^{22}) * 0.065 * \Delta P$. The volume of the plenum is 65ml and the number of particles in one bar litre is $2.42\text{x}10^{22}$.

Ideally, the number of injected particles would be determined using dedicated lab experiments. However, this has not been possible. The number of injected particles show good agreement between the TG1 measurements and the calculated amount based on the plenum volume. Due to the systematic offset on the TG1, and the operation of TG1 at the upper limit of the Pirani measurement, the number of injected particles will be derived using the plenum volume (figure 5.15, red triangles).

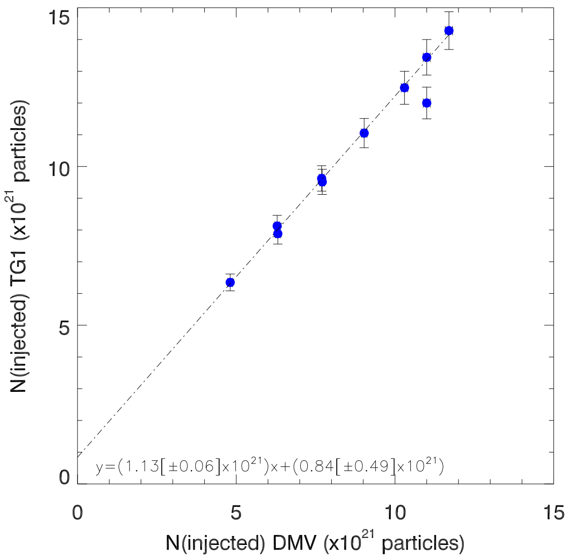

Figure 5.14: Comparison between the number of particles delivered by the DMV (abscissa) and the rise in the number of particles as indicated by the MAST vacuum gauge TG1 (ordinate). Error bars are based only on the specified value for the gauge.

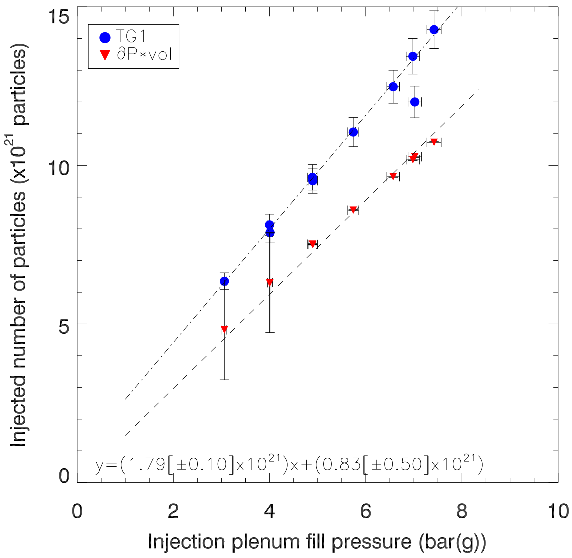

Figure 5.15: The chart shows the number of particles injected by the DMV into the MAST vacuum vessel (as derived from TG1) as a function of the DMV injection plenum fill pressure (blue circles). The number of particles calculated from the pressure change in the plenum and the plenum volume is shown (red triangles). The error on the points is derived from the uncertainties quoted in the pressure gauge literature (5% for TG1 and 2% for the DMV plenum gauges) The error on the pressure change are 2%, except where the pressure after injection falls to 0 bar(g), where they are derived from an error in ΔP of 1 bar.

5.4 Summary

The MAST disruption mitigation system is capable of delivering up to 1.95 bar litres of noble gas to the MAST vessel, approximately 100 times the plasma inventory. The injection of the gas is performed using an eddy current actuated disruption mitigation valve (DMV) supplied by Forschungszentrum Jülich which is of a similar design to the JET DMV. The valve is actuated using a custom built capacitor bank pulsed power supply which can be triggered at a set time using the MAST control system.

Chapter 6

Dynamics of Massive Gas Injection

Disruption mitigation experiments performed on MAST have set out to develop an understanding of the physics of mitigation. In order to study the physics of massive gas injection (MGI), controlled terminations have been performed by firing the DMV into a discharge at a fixed time. This chapter presents a brief outline of the disruption mitigation sequence, followed by an assessment of the propagation, penetration and mixing of the injected neutrals and ions with the bulk plasma.

6.1 Disruption mitigation sequence

Disruption mitigation has been performed in both ohmic and beam heated L mode discharges and beam heated H mode discharges. The timeline for mitigation of the discharge can be seen in figure 6.1 which shows various plasma parameters as a function of time. The time the valve is fired is determined using monitoring of the capacitor bank charge voltage. The injected quantity of gas is 7.8x10^{21} particles of a 90% helium 10% argon mixture, which is approximately 10 times the plasma inventory .

Following the firing of the valve, the neutral gas propagates to the edge of the plasma during the vacuum transit time (yellow panel on figure 6.1). The arrival of the injected impurities at the plasma edge is determined using the point at which first light is detected on an unfiltered camera observing the injection location (see figure 6.1, panel g)).

Upon arrival at the edge of the plasma, the injected impurities become ionised and localised around the edge of the plasma as a result of the magnetic field, as seen on figure 6.1, panels h-i. The ionisation and radiated of the injected impurities cools the plasma edge (blue phase on figure 6.1). Ultimately, the cooling of the plasma produces contraction of the plasma current profile, giving rise to the growth of MHD activity, as seen on figure 6.1, panel f) leading to the thermal quench (red phase). The onset of the MHD activity appears to trigger the thermal quench of

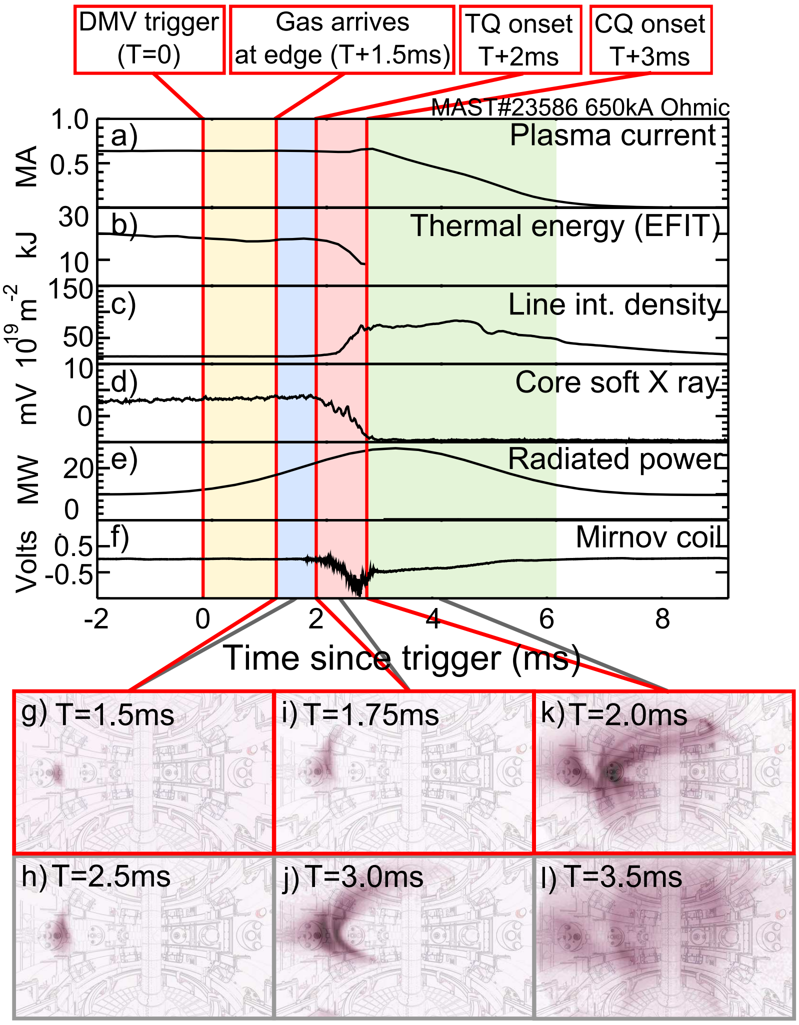

Figure 6.1: Disruption mitigation timeline for an MAST discharge. Panels g) to l) show frames from an unfiltered high speed camera observing the injection. The camera frames are used to determine the time required for the gas to reach the edge (vacuum transit time) shown in yellow. The blue phase shows the edge fill time, where the injected impurities are cooling the edge of the plasma. The cooling leads to the thermal quench (red phase) which is determined from the collapse of the core soft X ray trace. The green phase shows the current quench brought about by the cooling. The images in panels g to l have been gamma corrected and overlaid with a CAD image of the MAST vessel for clarity

the core plasma around 2ms after the triggering of the valve. The thermal quench is identified using a core soft X ray channel (panel d)) and has a duration of 1ms. The rise in the radiated power prior to the trigger time is a result of the heavy smoothing applied to the bolometer signal. The thermal quench phase marks the point at which power is deposited onto the divertor surfaces via transport from the plasma core. The enhanced impurity mixing brought about by the MHD activity gives rise to impurity assimilation during the thermal quench, as shown by the increase in line integrated density (panel c)) [41]. The high speed imaging shows that there is increased interaction of the impurities with the plasma during the thermal quench and current quench phase than compared to the edge fill phase. The expansion of the impurity plume around the plasma is consistent with the magnetic field geometry in MAST (figure 6.1, panels j-k). The cooling of the plasma during the thermal quench increases the plasma resistivity leading to the loss of the plasma current in the current quench phase (green phase). It can be seen on the high speed imaging that the impurities are well mixed with the bulk plasma by the midpoint of the current quench (figure 6.1, panel l).

6.2 Vacuum transit time

The vacuum transit time has been determined using the time between the triggering of the valve and the observation of light on the fast unfiltered (50kHz) camera which views the whole plasma. The integration time of the camera is set to ensure that the images are correctly exposed during the thermal quench phase of the plasma where there is significant radiation. The camera is fitted with a 0.9 optical density filter which reduces the transmittance to 12.5%. The duration of the vacuum transit time as seen by a correctly exposed camera with the neutral density filter is around 1.5ms, giving a propagation velocity of 1200ms^{-1}, which is consistent with propagation at the sound speed of the bulk impurity (helium, $v_s = 1400ms^{-1}$) [55, 106]. However, it has been reported [41, 67] that the propagation speed should be higher than the sound speed as the adiabatic expansion of a gas into vacuum occurs at 3 times the sound speed of the gas [53, 107]. The use of an increased integration time and brightness enhancement on the camera data show that the upper limit on the propagation time is approximately 1ms (± 0.2ms, based on camera frame rate), resulting in a propagation velocity which is 1.5 times that of the thermal velocity of the gas which is consistent with the results published in [41, 58, 61].

6.3 Impurity penetration

The penetration of the neutral and ionised impurities can be followed in MAST using high speed filtered imaging. The injection of an argon/helium mixture allows both helium and argon impurity line imaging to be performed. The penetration of neutrals into the plasma can been monitored using He I (706nm) and Ar I (696.5nm), with the penetration of singly charged species with He II (468nm) and Ar II (458nm) impurity lines. Helium imaging is chosen to monitor the penetration, as helium appears to penetrate deeper into the plasma than argon. The deeper penetration of helium over argon is likely due to the higher first ionisation energy of helium and increased sound speed. The location of the last closed flux surface (LCFS) and the q=2 surface can be determined by overlaying the EFIT equilibrium at the time of injection over the camera images, once they have been aligned with respect to fixed points in the vacuum vessel (typically, the centre column and poloidal field coils are used to perform the alignment).

6.3.1 Neutral penetration

The penetration of neutral helium during the thermal quench phase of the plasma can be seen in figure 6.2 with the LCFS overlaid in grey. The last stable EFIT equilibrium prior to the injection of the impurities is used to locate the LCFS, as the EFIT reconstruction does not take into account the effect of the impurities arriving at the plasma edge.

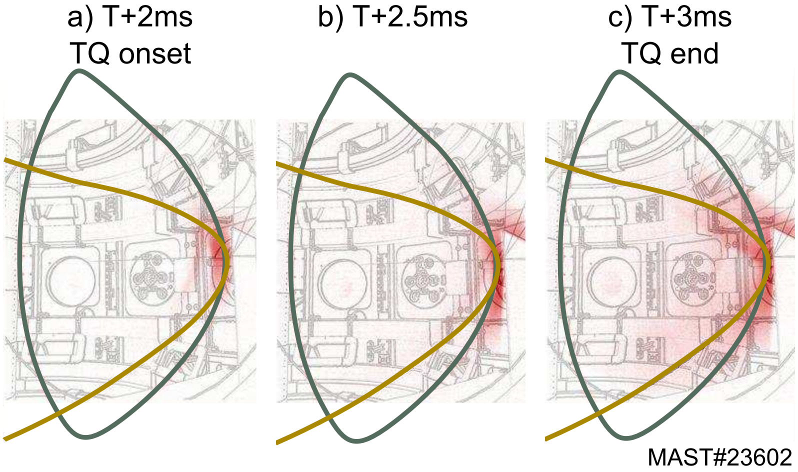

Figure 6.2: Neutral helium penetration during the thermal quench using He I (706nm) imaging. The LCFS shown in grey is obtained from EFIT reconstruction of the plasma and a field line on the LCFS is shown in gold. The injection of impurities occurs from the right hand side of the image, with the DMV port being obscured by the NBI beam dump. The image is false coloured, gamma corrected and overlaid over a CAD model of the interior of the MAST vessel for clarity.

The localisation of the neutral emission around the LCFS shows that there is limited neutral penetration at the onset of the thermal quench. The time evolution of the neutral emission shows that the neutrals remain localised around the LCFS and do not penetrate deeply into the plasma during the thermal quench phase. The impurity plume appears to spread around the LCFS in a direction which follows the shape of a LCFS field line (gold line, figure 6.2). The expansion of the plume is consistent with the magnetic field direction in MAST which is supported by the match between the LCFS field line and the localisation of the emission along it. The expansion of neutrals along the LCFS field line is consistent with observations on other machines [62] that the neutrals are entrained in the ions. The ions must follow field lines, and hence the neutrals are dragged with them producing the expansion along the field line seen in figure 6.2.

6.3.2 Ion penetration

The corresponding images showing the penetration of helium ions into the plasma are shown in figure 6.3. It is clear from comparing figures 6.2 and 6.3 that the ions penetrate much deeper into the plasma than the neutrals. The ion emission is clearly inside the location of the LCFS (shown in grey) and is localised around the q=2 surface (blue line). The temporal evolution of the ion emission also differs from that of the neutrals. The ion emission becomes mixed through the bulk plasma during the thermal quench phase, becoming more dispersed around the q=2 surface in figure 6.3 b), before mixing throughout the frame in figure 6.3 c). The increased mixing seen supports measurements of the line integrated density that the majority of the impurity mixing occurs during the thermal quench phase of the mitigation. The localisation of radiation around the q=2 surface prior to the onset of the thermal quench supports data measured in other tokamaks that the q=2 surface plays a critical role in the triggering of the thermal quench in a mitigated discharge [60, 108].

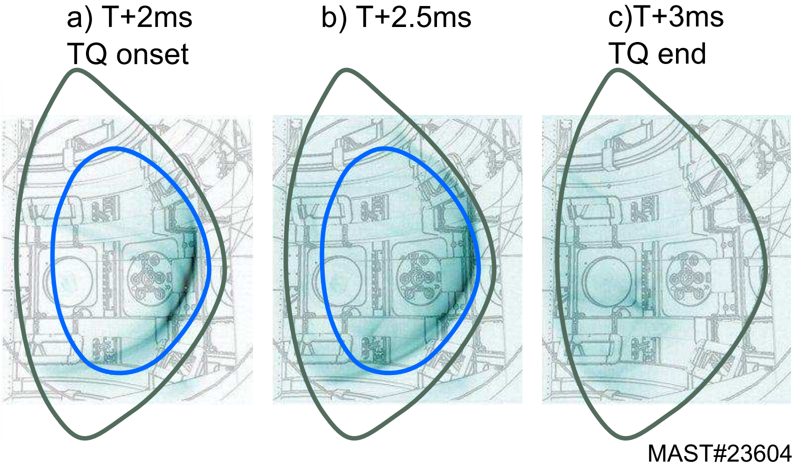

Figure 6.3: Singly ionised helium penetration during the thermal quench using He II (468nm) imaging. The LCFS shown in grey is obtained from EFIT reconstruction of the plasma and the q=2 surface is shown in blue. The injection of impurities occurs from the right hand side of the image, with the DMV port being obscured by the NBI beam dump. The image is false coloured, gamma corrected and overlaid over a CAD model of the interior of the MAST vessel for clarity.

6.4 Plasma profile evolution

The mitigation of a discharge via massive gas injection on MAST has proven to be highly reproducible, with little variation in the plasma parameters seen when a given discharge is repeated (figure 6.4). The reproducibility of the discharges allows high temporal resolution TS data to be collected by repeating a discharge and adjusting the TS laser temporal spacing and offset, the temperature and density profiles can be captured during the build up to and into the start of the thermal quench with a time resolution of up to 0.05ms in current studies.

The TS data taken during the mitigation is affected by the increased background light from the radiation of the injected species. The background light becomes larger than the scattered signal for viewing chords which have a line of sight view of the injection location. The result of this is that the chords viewing the inner part of the plasma are unaffected, as are the outermost chords. However, chords which

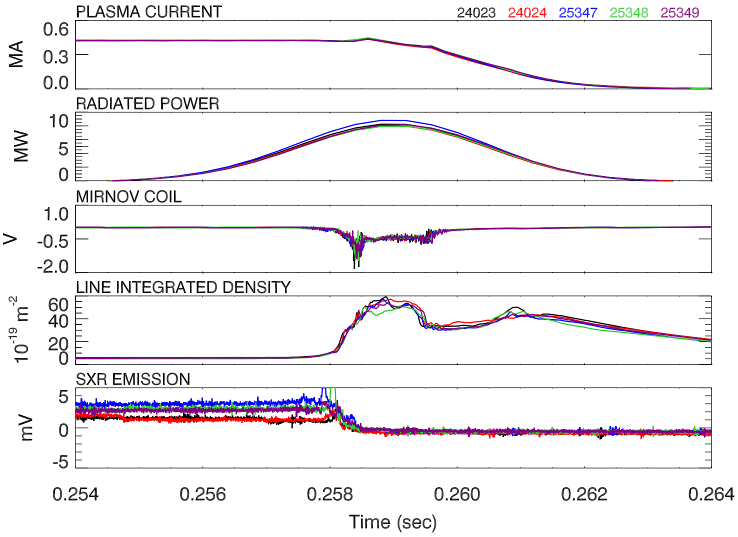

Figure 6.4: Examples of repeated mitigated discharges. Discharges can be seen to be reproducible, with little variance in the parameters shown. Variations in the soft X ray signal are likely due to increasing impurity build up following successive injections.

view the major radius of the plasma between 0.9 and 1.15 metres have background levels above the signal level, which prevents a fit to the scattered signal from being performed, as shown by the greyed regions of figure 6.5. The reliability and accuracy of the data points outside these region has been seen to be good, as discussed below.

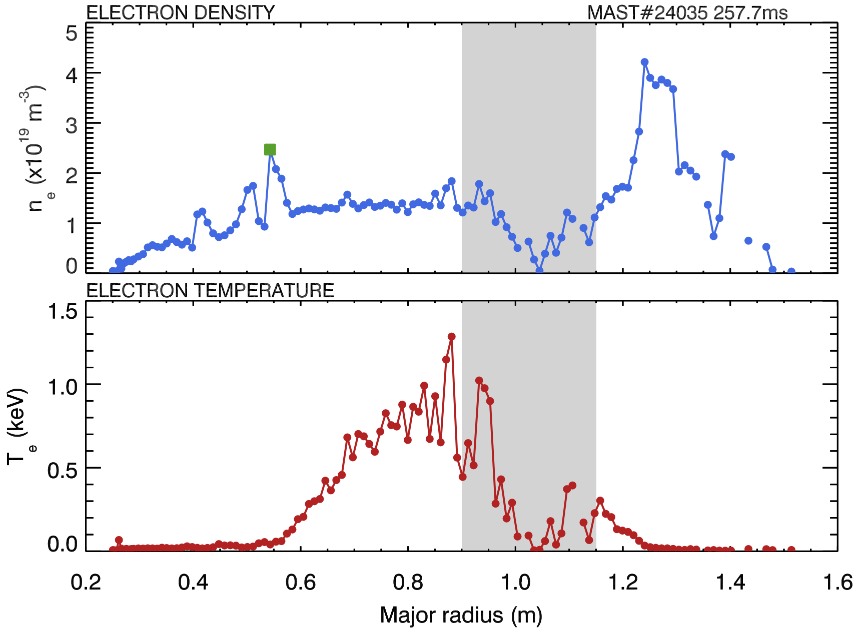

Figure 6.5: Thomson scattering profiles for the temperature and density during the mitigation. The region shaded in grey is affected by increased background emission from the injected impurity species thereby preventing accurate measurement of the temperature and density in this region. The green square point corresponds to a radius of 0.54m. The error on the density and temperature for each spatial point is ±5%.

6.4.1 Validity of the Thomson scattering data

The repeatability of the Thomson scattering (TS) data can be seen in figure 6.6. The figure shows the density profile from discharges 24034 and 24035, which is a repeat of 24034. These two discharges share a common TS measurement at 257.6ms, 1.75ms after the DMV trigger. The profiles are well matched, and the density can be seen to be building up in the same region during both discharges.

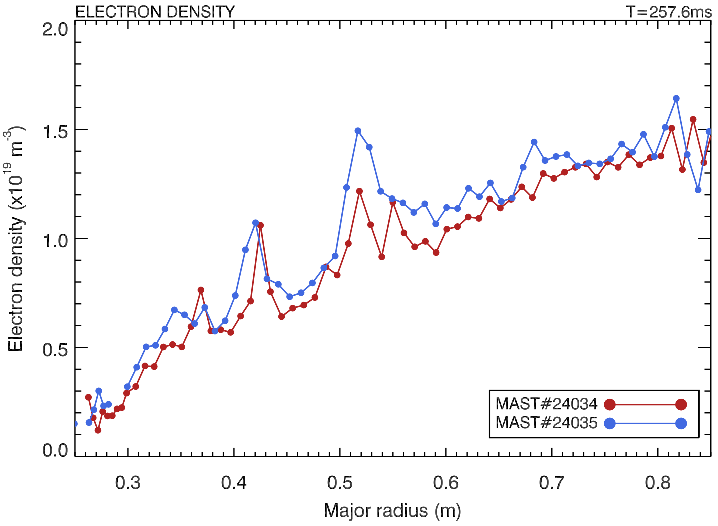

Figure 6.6: Electron density profiles from two mitigated discharges obtained using Thomson scattering. The red trace is from MAST#24034 and the blue trace is a repeat of this discharge. The profiles are well matched and both exhibit the build up of density rational surfaces. The rror on the density for each spatial point is ±5%.

The TS system records the spectrometer signal for a period of 300ns around the firing of the laser pulse. An example of the spectrometer signal during mitigation in a region which density build up occurs (0.54m radius, see figure 6.5, green square) is shown in figure 6.7. The fit to the signal is shown in blue, and it is the fitted data which is used to determine the density. A concern for TS measurements during mitigation would be the background emission from the injected impurities exceeding the scattered signal. The record of the background signal for a period around the laser pulse (figure 6.7) shows that the background level is correctly subtracted and does not exceed the signal level.

The evidence presented here shows that the TS data taken during the mitigation is both repeatable and reliable. The evolution of the plasma profiles during mitigation can now be followed using the TS system.

6.4.2 Inboard plasma profile evolution

The evolution of the temperature and density can be monitored by repeating a set discharge and building up a series of TS profiles. The data shown in figure 6.8 is

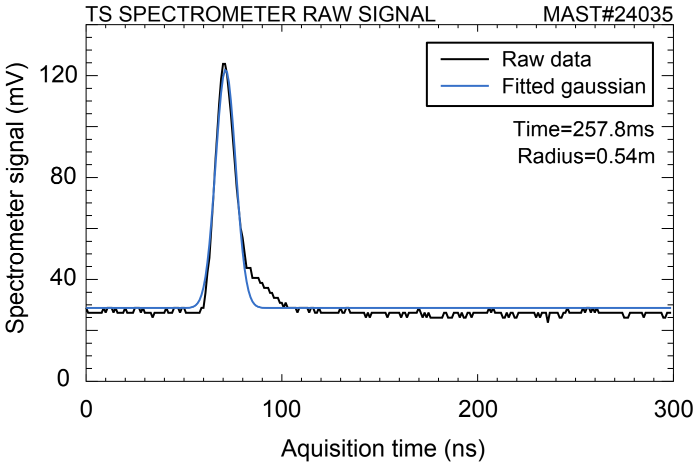

Figure 6.7: Thomson scattering spectrometer data recorded around the laser pulse during discharge 24035 at 257.8ms, during the density build up. The spectrometer is viewing the radius R=0.54m which corresponds to the point in figure 6.5 shown by the green square.

composed of profiles from eight repeated discharges, each with eight profiles per discharge giving a total of 64 measurements of the temperature and density profiles. The figure shows the inboard data, as a result of the saturation of the outboard channels from background emission. The plot starts in time from the point at which the injected impurities are seen to arrive at the plasma edge, as determined using high speed visible imaging with a time resolution of 20 μs and ceases shortly after the thermal quench has occurred.

The data in figure 6.8 shows that the impurities arriving at the edge of the plasma 1.4ms after the trigger begin to cool the plasma edge and give rise to contraction of the temperature profile. As the discharge progresses, it can be seen that the cooling front moves through the plasma edge crossing various rational surfaces generating a contraction of the temperature of approximately 20cm during the edge cooling phase. The TS data allows the cooling front location to be directly measured, by defining a contour on the plot (figure 6.8 b)) which corresponds to the temperature at ψ_{95} (50eV) prior to the injection. The cooling front exhibits a gradual, steady cooling of the plasma edge, which would be associated with energy loss via impurity line radiation during the edge fill time. The thermal quench can be identified using the core soft X ray signal and can be seen in the sudden decrease in the core temperature measurements on panel b). The sudden drop in the core temperature does not follow the gradual cooling that is associated with the cooling front, hence the thermal quench must be generated by a instability generated during the edge fill phase as reported elsewhere [60, 66, 109, 110]. The cooling front velocity can be calculated by taking the gradient of the gold line in figure 6.8, which gives the inward velocity of the front to be approximately 340 ms^{-1}.

The electron density during the edge fill time is shown in figure 6.8, panel c). Comparison of the cooling front location and the density profiles show that there

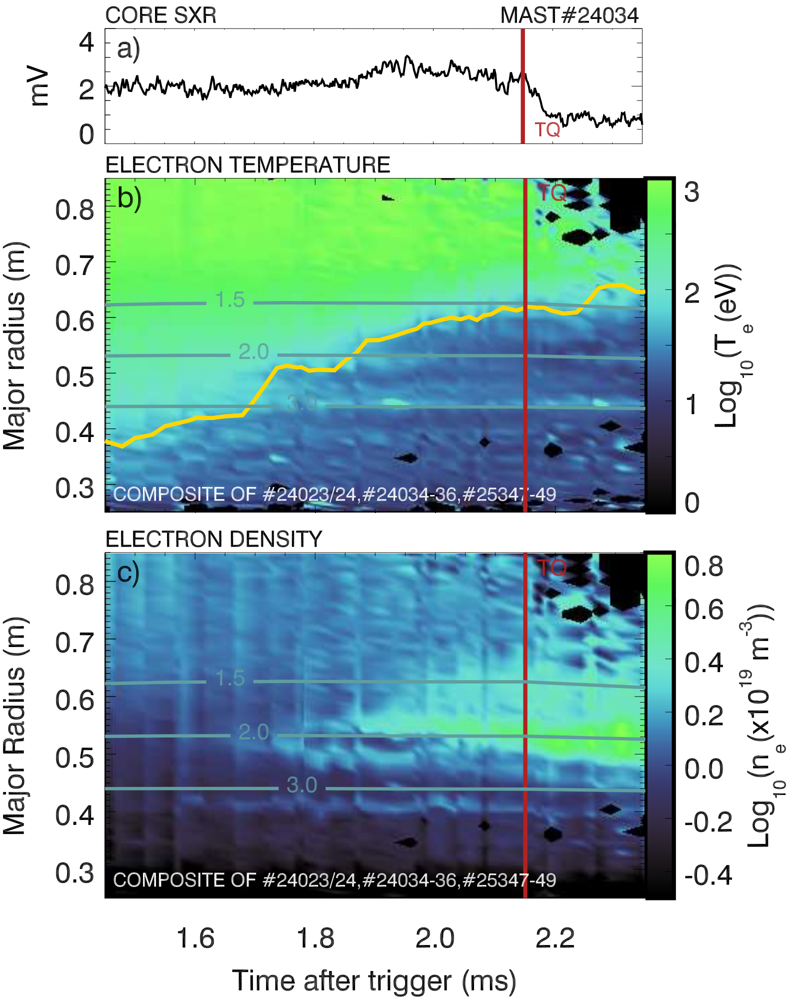

Figure 6.8: Thomson scattering profile evolution on the inboard plasma side prior to the thermal quench as a function of time after the DMV trigger. The figure is a composite of Thomson scattering data from a set of eight repeated discharges. The scales are logarithmic to account for the wide variation in temperature and density that is generated by massive gas injection. The grey lines show the radius of q surfaces as derived from EFIT reconstruction during the mitigation. The gold line corresponds to a temperature of 50eV, which is the temperature at ψ_{95} prior to mitigation of the discharge. The thermal quench is denoted by the vertical red line.

are density rises along rational surfaces which are associated with the cooling front crossing these rational surfaces. The growth of density occurs first on the q=3 surface, at 1.6ms, followed by density build up on the q=2 surface at 1.8ms. A single TS profile taken during the edge cooling phase is shown in figure 6.9 which shows the inboard data over the same radius range as shown in figure 6.8. The figure shows the location of the q=2 and q=3 rational surfaces as derived from EFIT reconstruction. It is clear from figure 6.9 that the build up on the rational surfaces prior during the edge cooling phase is significant and amounts to a value which is twice that of the central density prior to mitigation. The magnitude of the density gradient around the build up is similar to those associated with H mode pedestals.

The penetration of the impurities to the q=2 surface as shown in figure 6.3 it thought to be critical for the initiation of the thermal quench in a mitigated discharge [60] and has been shown to be associated with the onset of the thermal quench in several other machines via the use of visible imaging [108, 109, 110]. The data from MAST supports these observations of impurities arriving at q=2 from visible imaging by directly measuring density structures associated with the trapped impurities on rational surfaces. The behaviour seen in L mode discharges as detailed here is also seen during H mode mitigation.

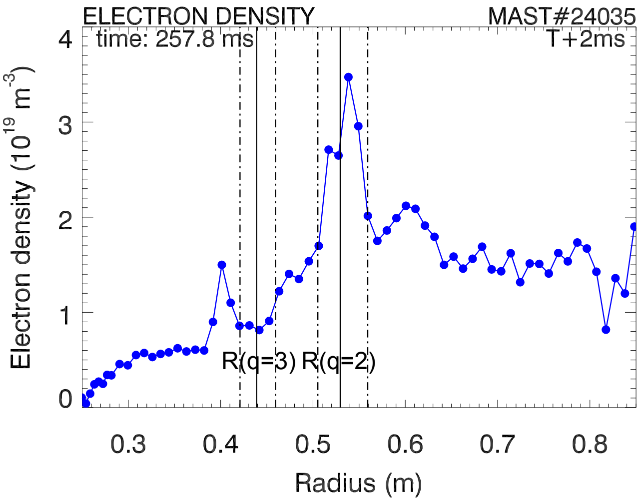

Figure 6.9: Thomson scattering profile taken during the edge cooling phase in discharge MAST#24035.The profile shows data from the inboard plasma side, over the same major radius as that shown in figure 6.8. The location of the q=2 and q=3 surfaces are shown as derived from EFIT reconstruction, with the error arising from a ±10% variation in the expected value of ψ_N at the rational q surface.

6.4.3 Outboard plasma profile evolution

The Thomson scattering data for the outboard side of the plasma is shown in figure 6.10 and shows the cooling front as defined by the temperature at ψ_{95} (gold line). The cooling front velocity is 170ms^{-1} on the outboard plasma side, which is around half that of the inboard plasma side. The density on the outboard side of the plasma is double that of the inboard plasma side. The build up of density on rational surfaces is not as clear on the outboard side, likely as a result of the increase quantity of gas injected on this side and as a result of Shafranov shift. However, it is clear that the density begins to build up on the outboard side in the region between the q=2 and q=3 surfaces. The onset of the density build up occurs at similar times on the outboard and inboard side; by comparing the electron density of both data sets over the same density range it can be seen that the build up of density starts 1.7 to 1.8ms after the DMV is triggered.

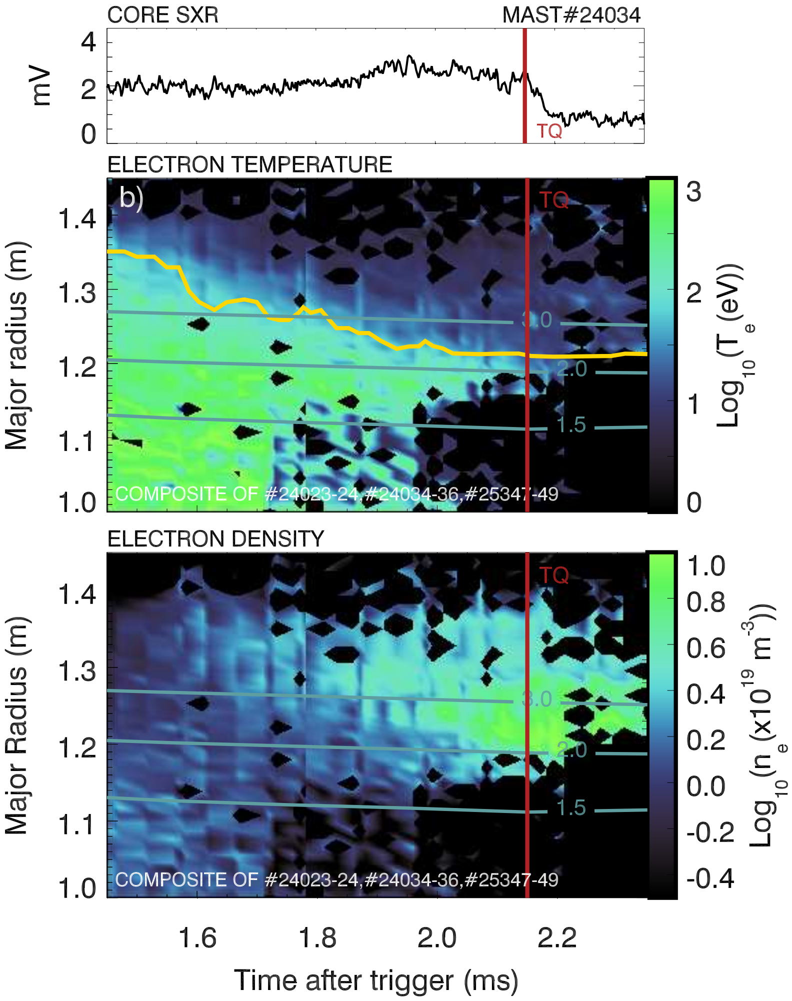

Figure 6.10: Thomson scattering profile evolution on the outboard plasma side prior to the thermal quench as a function of time after the DMV trigger. The scales are logarithmic to account for the wide variation in temperature and density that is generated by massive gas injection. The grey lines show the radius of q surfaces as derived from EFIT reconstruction during the mitigation. The gold line corresponds to a temperature of 50eV, which is the temperature at ψ_{95} prior to mitigation of the discharge. The thermal quench is denoted by the vertical red line.

6.4.4 Assessment of cooling front asymmetry

The effect of Shafranov shift is to push the inner flux surfaces outwards toward the LCFS, thereby making the distance between two rational surfaces on the inboard side larger than the outboard. The smaller distance between the flux surfaces on the outboard side makes it appear as though the cooling front propagates slower when compared to the inboard. Figure 6.11 shows the position 50eV cooling front in normalised flux (Ψ_N) as a function of time for the inboard and outboard regions. It is clear from 6.11 that the cooling front propagates at the same speed on the inboard and outboard side.

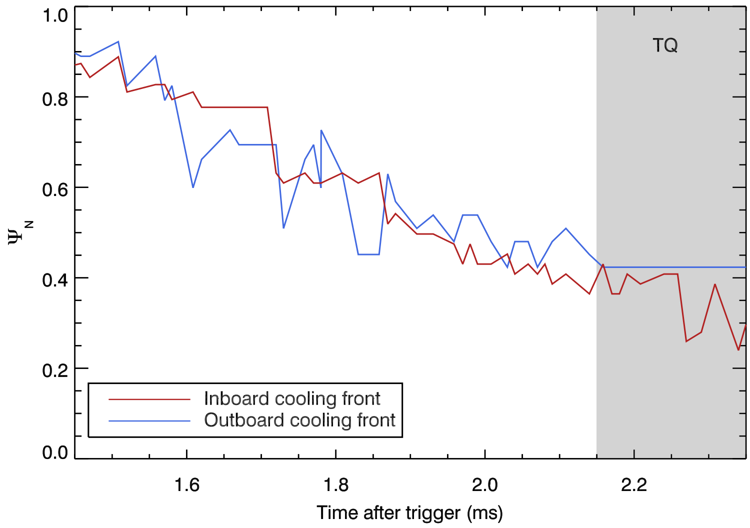

Figure 6.11: The figure shows the location of the cooling front in normalised flux space on the inboard (red) and outboard (blue) sides. The cooling front propagation speed is the same on both sides and the front penetrates to the same depth prior to the onset of the thermal quench (shaded grey).

6.5 Rational surface density build up

The TS data shown in figures 6.8 and 6.10 show that density build up occurs on rational surfaces as the cooling front crosses them, ultimately leading to the onset of the thermal quench. The present theory for the initiation of the thermal quench is the cooling of the plasma (via radiation), contraction of the current channel and the triggering of the growth of MHD activity, specifically the growth and overlap of m/n=2/1 and 1/1 modes. The overlapping of the modes gives rise to a stochastic region resulting in the thermal quench [65, 66].

The location at rational q surfaces and the radially localised nature of the density build suggests that magnetic islands have formed within the plasma as a result of the cooling. The growth of magnetic islands can be seen by using Mirnov coil data. The data from four toroidally displaced Mirnov coils can be combined such that the amplitude of odd and even toroidal mode numbers, n, can be identified. The traces for discharge 24034 are shown in figure 6.12 and show the amplitude of odd and even modes grow during the edge cooling phase. The growth in the amplitude of the mode is coincident with the growth of density on the q=2 surface, suggesting that the density build up occurs on a 2/1 island which supports the results from modelling [65, 66].

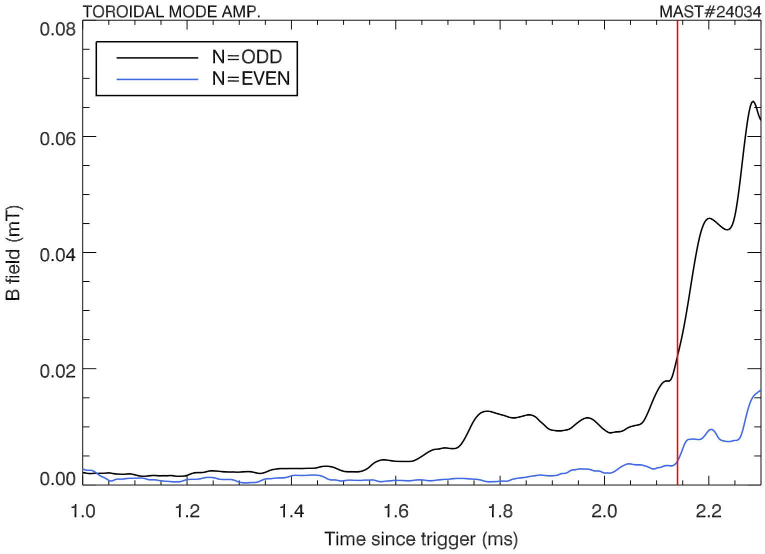

Figure 6.12: Toroidal mode amplitude during the density build up phase showing the growth in the n=odd and n=even modes prior to the thermal quench. The times shown correspond to the time after the DMV trigger and can be compared with figures 6.8 and 6.10. The onset of the thermal quench is shown by the vertical red line.

The Thomson scattering data in figure 6.8 does not shown oscillation in the density values, which would be expected if the density build up were located on a magnetic island which rotates with the plasma. The density build up is seen in all mitigated discharges, and is not observed to oscillate in amplitude between TS time slices, or repeats of the discharge. The lack of oscillation suggests that the mode has locked and that the locking of the mode always occurs at the same toroidal location. Typically, evidence for mode locking can be found using saddle coils attached to the MAST vessel wall. The current penetration time through the saddle coils limits the resolution of the saddle coils to frequencies of less than 10Hz, preventing use for disruptions where the time scales are 10 to 100 times faster. Mode locking can be observed by the splitting of divertor strike points as a result of the perturbation of the equilibrium field generated by a large mode [111]. Figure 6.13 shows a series of unfiltered camera frames covering the lower divertor during the density build up phase. It can be seen that there is evidence for strike point splitting at times consistent with the density build up phase, suggesting the presence of a locked mode. Indeed, it appears as though the onset of the split strike point (figure 6.13) coincides with the start of the density build up (T=1.5ms)(figure 6.8).

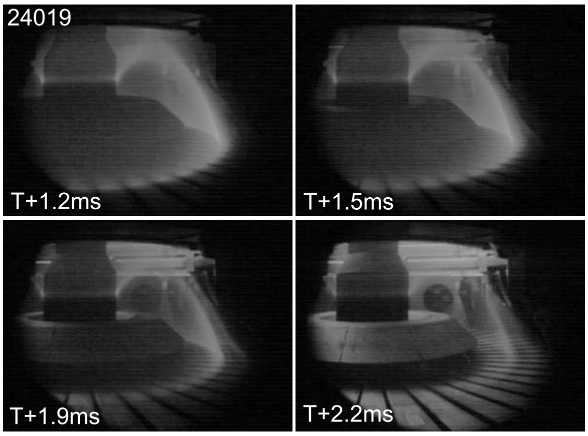

Figure 6.13: Imaging of divertor strike point showing splitting during the density build up phase which is indicates the presence of a locked mode. The times shown correspond to the time after the DMV trigger and can be compared with figures 6.8 and 6.10.

Additional evidence for the presence of a locked mode during injection can be seen in Langmuir probe (LP) measurements of the particle flux at the divertor (figure 6.14). The LP data shows evidence of splitting in agreement with the camera data. The presence of a split strike point on the LP data confirms that the splitting seen on the camera arises as a result of magnetic perturbation to the strike point rather than the formation of a radiating layer as a result of impurity injection.

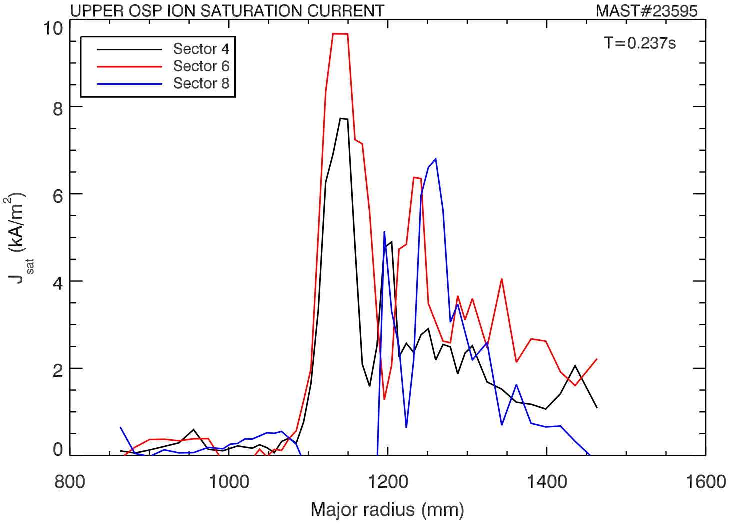

Figure 6.14: Langmuir probe data taken during the cooling phase showing evidence for strike point splitting. The data is taken one millisecond prior to the onset of the thermal quench in an ohmic discharge. The data shows Langmuir probe data from three different sectors, each spaces by 30 degrees. The splitting is seen across all sectors. The data from sector 8 (blue line) is affected by the failure of an amplifier, which prevents the data around the strike point (1100-1200mm) from being recorded.

The lack of discharge to discharge variation in the location of the density build up suggests that the mode locks in the same location toroidally each time the plasma is mitigated. One cause for the locking of the mode in the same location can be derived from angular momentum conservation between the rotating plasma and the injected impurities. The toroidal rotation velocity prior to injection can be obtained from charge exchange, and shows the plasma to rotate at 15 kms^{-1} at the q=2 surface. Assuming that rotation should be stopped outside the q=2 surface, then the angular momentum of the plasma from the q=2 surface outwards can be calculated. The injected quantity of gas from the DMV can be calculated based on the fill pressure, allowing the increase in mass of the system to be found. Applying conservation of momentum, then the rotation velocity is calculated to be 350ms^{-1} following injection, a decrease of 98% over the pre injection velocity, which suggests mitigation can halt the plasma rotation.

6.6 Modelling of density build up

The build up of density on magnetic islands has been reported elsewhere [112, 113, 114] and is most associated with the formation of a snake [6, 114]. These results present an explanation for the density build up during the cooling phase of the mitigation; magnetic islands form, upon which the density builds up. The lack of oscillation in the density, which would normally be observed with a snake [115] can be explained by the locking of the magnetic islands at a given toroidal location which is in the field of view of the Thomson scattering system.

6.6.1 Description of the model

In order to model the density build up a simple convection diffusion model can be used to follow the evolution of the electron density. The model is based on a model produced by Arends [116]. The equation to be solved is shown in equation 6.1, where n_e is the electron density, S is the source term and $\vec{\Gamma}$ is defined in equation 6.2 where D is the cross field diffusion and V is the convective velocity.

$$\frac{\partial n_e(r,t)}{\partial t} + \nabla \cdot \vec{\Gamma} = S(r,t) \tag{6.1}$$

$$\vec{\Gamma} = -D(x)\nabla n_e(r,t) + \vec{V(x)} n_e(r,t) \tag{6.2}$$

The model solves equation 6.1 in one dimension using cartesian coordinates. The normalised radial coordinate is used and defined as $x = r/a$. The initial conditions of the model are as follows;

- The initial electron density profile is taken have the form of equation 6.3 with a central density, n_0, of 1.7x10^{19}.

$$n_e = n_0 \left(1 - \left(\frac{r}{a}\right)^2\right) \tag{6.3}$$

- The initial convective velocity is given by equation 6.4, where D_0 is the diffusion coefficient at r=0 and $\lambda = 20$ to cause the convective velocity to fall to zero at the plasma edge.

$$V = -\frac{2D_0 r}{a^2}\left(1-\left(\frac{r}{a}\right)^2\right)^{\lambda}\hat{r} \tag{6.4}$$

- The source term is modelled as a gaussian located at $r/a = 0.9$ and of magnitude 3.5x10^{21} $\mathrm{m}^{-3}\mathrm{s}^{-1}$ with an additional term added to it to account for charge exchange processes which allow neutral particles to access the core of the plasma. The charge exchange term is defined as $S_{CX} = C10^{(r/a)}$ where $C = 5\text{x}10^{18}$. These values are chosen to produce a flat diffusion profile across the plasma minor radius with a central value of $D_0 = 0.4$.

The initial conditions, which are taken from [116] are used in conjunction with a forward difference method to determine the steady state diffusion profile. The diffusion and velocity profiles are then modified and the electron density evolved in time using the techniques set out in appendix A.

6.6.2 Density build up model

The presence of a magnetic island and the trapping of particles within the island suggest that the diffusion and convective velocity profiles have been modified in the vicinity of the island [113, 114]. It has been suggested that the diffusion coefficient within the island is lower than the surrounding plasma [113] and there exists a convective term which acts to transport particles to the centre from the island separatrix [114]. The source of the increased density arises from the mitigation.

The TS data from the inboard plasma side (figure 6.8) suggests that the cooling front penetrates into the plasma at a constant speed until the front reaches the q=2 surface, at which point the cooling front appears to slow, becoming stationary at the q=2 surface for 0.15ms prior to the thermal quench. The cooling front can be used to generate a source term as shown in figure 6.15 to model the front passing through the plasma. The source term increases in amplitude linearly to model the influx of particles from the DMV. The variation in the plasma density is not modelled as part of the source term as it is assumed to be insignificant compared to the number of particles injected.

The source term, combined with the modified diffusion and convective velocity profiles form the basis of the density build up model. The diffusion profile is modified around the islands such the coefficient is decreased to 10% of the value either side of the island. The velocity profile is modified either side of the island as shown in figure 6.16 by adding gaussian profiles to the island region. The amplitude of the gaussian is used as a free variable. The source term magnitude is adjusted such that the density on the q=2 surface at the thermal quench matches that seen

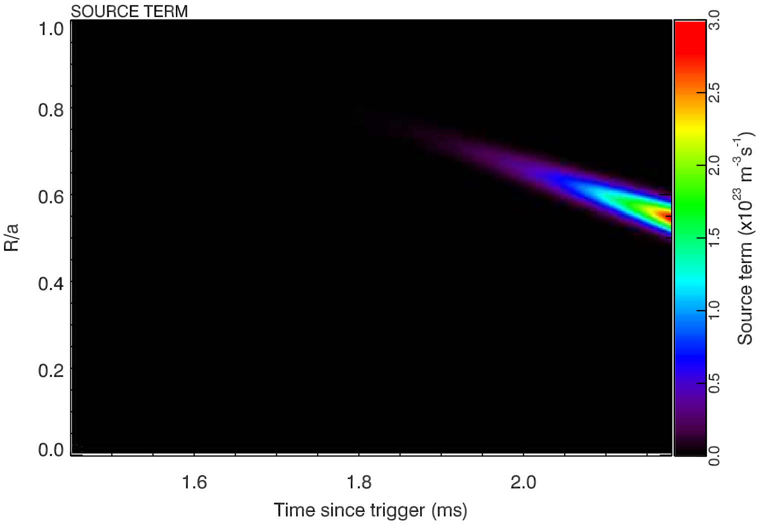

Figure 6.15: The source term used to modelled the density build up. The source term follows the contraction of the plasma during the edge cooling phase. The front is defined using the 20eV contour.

experimentally.

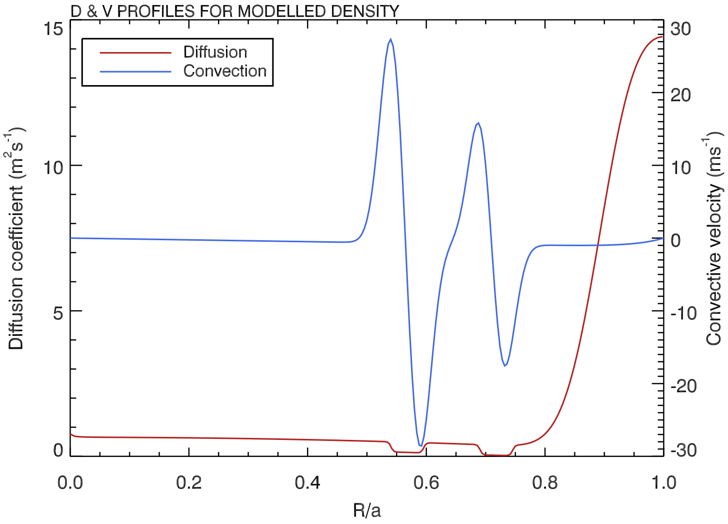

Figure 6.16: The diffusion and convective velocity profiles are adjusted in the regions around the q=2 and q=3 surfaces to model the presence of an island. The diffusion coefficient is reduced and a pinch term added which is directed to the island centre.

The result of modelling the density build up is shown in figure 6.17 and can be compared to the TS profiles shown in figure 6.18. The corresponding diffusion and convective velocity profiles used in the model are shown in figure 6.16.

The modelling shows that the density build up can be reproduced by applying a snake like model with the addition of an increased convective velocity term around

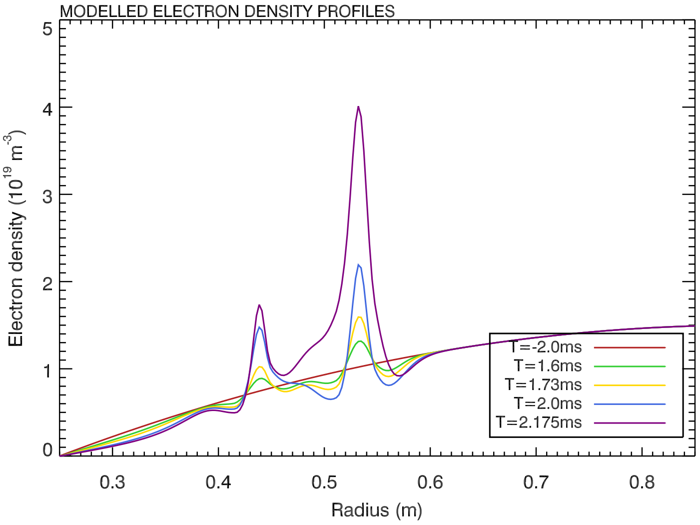

Figure 6.17: Density profiles modelled using the source term, diffusion and convective velocity profiles above.

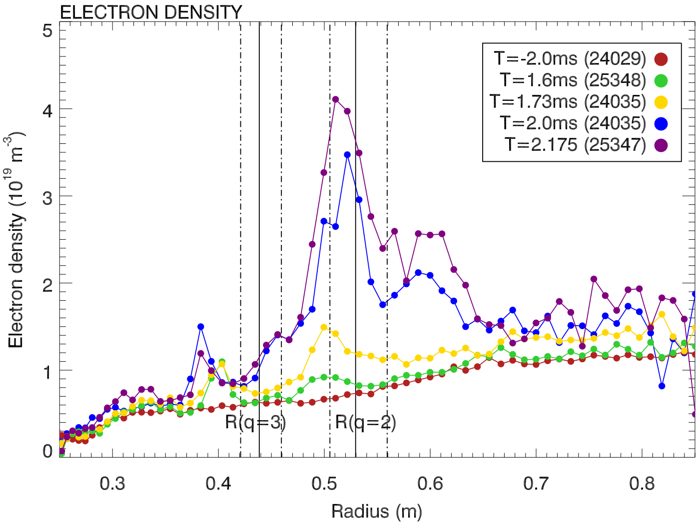

Figure 6.18: Thomson scattering profiles of the electron density for comparison with the modelled data in figure 6.17.

the islands. Snake modelling [113, 114] has shown that the diffusion term must be $\frac{1}{50}$ of the steady state diffusion coefficient to produce the required density build up in a snake. The snake modelling assumes that the convective term provides the fuelling and that steady state is reached. Although the modelled density profile for the density peaking does not show complete agreement with the experimental profiles, the increase of order twenty times in the convective velocity is consistent in magnitude with the changes made to the diffusion term in snake modelling previously performed. The results suggest that the density build up is consistent with island formation and subsequent build up of density on the islands, fuelled by the convective velocity. Further work to the model would be required, as a significant volume of physics is hidden within the diffusion and convective velocity terms, with the convetive term producing the largest impact on the profiles.

6.7 Dependence of mitigation timescales on q profile

The dependence of mitigation times on the position of the q=2 surface has previously been seen on DIII-D [60]. However, the results from MAST provide physical measurements of the densities on the q=2 surface in the stages leading to the disruption rather than measurements inferred from visible imaging [109, 110] or bolometry [71, 108]. The previous result on the q=2 surface dependence apply to conventional aspect ratio tokamaks. Spherical tokamaks (STs), such as MAST, have a q profile in which the central region is much flatter and the shear is localised in the plasma edge. To investigate the effect of the q profile dependence of an ST, an experiment similar to that performed in [60] was performed and the time required to initiate the thermal quench calculated.

The q profile can be varied either by changing the toroidal magnetic field or the poloidal magnetic field. On MAST the q profile was varied by ramping the plasma current during an ohmic discharge and thereby changing the poloidal field. The poloidal field was varied as the range over which the toroidal field can be varied is limited by hardware considerations and the aim of the experiment was to produce the largest possible range in q=2 position. The q profile scan was performed by mitigating the discharge at various points during the current ramp which correspond to different values of q_{95} (see figure 6.19).

The impact of the q profile on mitigation timescales can be assessed using the delay between the DMV trigger, $t(DMV)$, and the time at which the thermal quench occurs, $t(TQ)$. The delay time, $\Delta[t(TQ) - t(DMV)]$ is shown in figure 6.20 against the location of the outer q=2 surface and q_{95}. The delay time includes the vacuum transit time of the gas, which has been discussed previously. It must be noted that the vacuum transit time is a function of the integration time of the camera on MAST. As a result, it is not possible to separate the edge cooling time and the transit time for the traces in the q scan. However, analysis of the camera data has

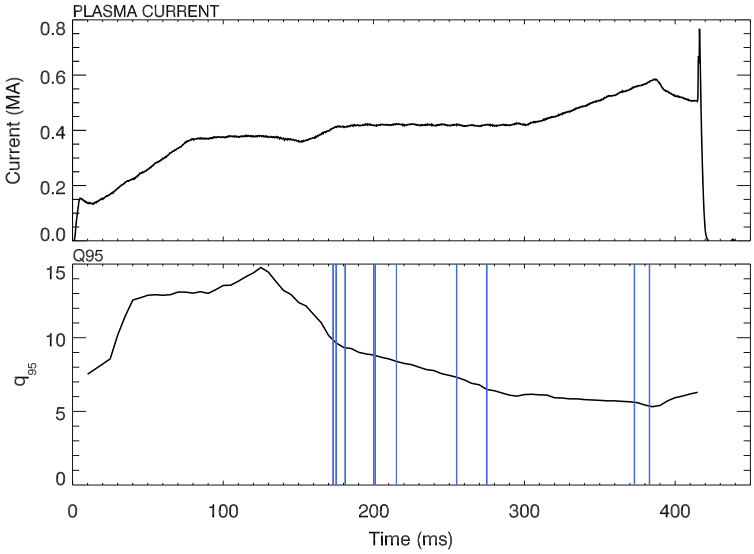

Figure 6.19: Discharge used for q profile dependence (MAST#23612). The figure shows the mitigation times used in the experiment (blue lines) and the values of q_{95} at which the DMV was triggered.

shown that the vacuum transit time is consistently 2.1ms for all of the q scan shots where the integration time of the camera was 1μs. Therefore, any variation in the delay time is not a consequence of a varying vacuum transit time.

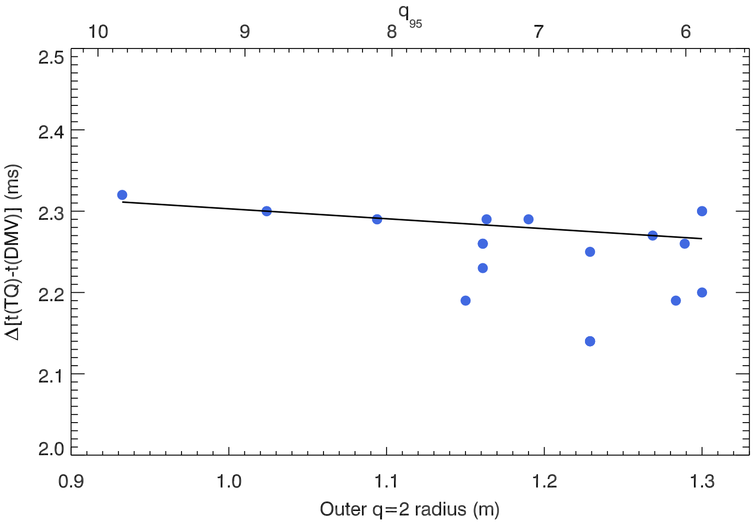

Figure 6.20: q profile dependence of the time between the onset of the thermal quench $(t(TQ))$ and the DMV trigger $(t(DMV))$

The trend of decreasing delay time with decreasing q_{95} is reproduced on MAST (figure 6.20). The dependence of delay time with q_{95} is expected as the deeper the q=2 surface is, the longer it will take for the cooling front to reach it. However, the trend is not as strong as for DIII-D and no saturation in the timescale is seen.

The q profile in an ST differs from a conventional tokamak in two main ways. Firstly, the lengths of the field lines on the inboard and outboard sides differ. The field lines are longer on the inboard compared to the outboard (see figure 6.21(a)) as a result of the strong variation of the toroidal magnetic field with radius which produces a higher average value of q [14]. In addition to the higher value of q_{95} the variation of q with minor radius (the magnetic shear) is concentrated in the outer part of the plasma (see q profile in figure 6.21(b)). The high shear at the edge produces a flat q profile across the central region with the shear located at the edge. Hence, a given rational q surface is located at a larger normalised radius than in conventional devices with a smoothly varying q profile [14].

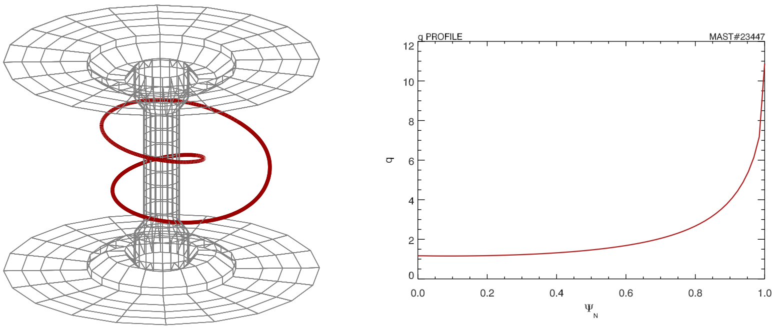

(a) q=2 field line, with outline of centre column and divertor in grey.

(b) Example of a MAST q profile (MAST#23447 333ms).

Figure 6.21: Illustration of a field line in MAST (figure (a)) and q profile in normalised flux space (figure (b)). The scatter seen in the data points at shallow q=2 surface depths results from the steep variation in the q profile at the plasma edge compared to the centre.

The delay time in MAST is approximately 2ms, which includes the vacuum transit time, by comparison, the time required to cool the edge in DIII-D is of the order of the MAST delay time (0.7ms). The increased speed of the quench in MAST over DIII-D could be due to the q profile. The thermal quench onset is thought to be caused by the overlap of island chains which grow on rational surfaces [66]. The high shear at the edge of the MAST plasma means that rational surfaces are located closer together at the plasma periphery than in a conventional tokamak. The density build up seen on Thomson scattering is evidence that more than one rational surface is involved in the mitigation sequence. If multiple island chains are involved in generating a stochastic region which gives rise to the thermal quench, then closely space rational surfaces are likely to lead to shorter delay times.

6.8 Fuelling efficiency

The fuelling efficiency is used to determine the fraction of the injected particles which are assimilated into the plasma. In order to suppress runaway electrons, it is necessary to raise the plasma density to a sufficiently high level (see section 2.6.4) to prevent the formation of a runaway electron beam by collisional suppression [61]. The fuelling efficiency, F_{eff}, is defined as shown in equation 6.5, where Δn_e is the increase in density as a result of the injection and n_{inj} is the number of particles injected [56].

$$F_{eff} = \frac{\Delta n_e}{n_{inj}} \tag{6.5}$$

The fuelling efficiency can be calculated in two ways, either averaged over the mitigation sequence [56] or expressed as a function of time [110, 117]. In both cases the increase in density is determined using line integrated measurements of the density and assuming that the impurities are singly ionised only. The impurities are seen to be singly ionised in other experiments [58, 62], it is thought that the rapid cooling of the plasma prevents higher charge states from being reached [62].

The number of particles injected in the averaged case is simply the total number injected as calculated from the plenum volume and pressure or measured by vacuum vessel pressure increase. In the time dependent case, then the number injected must be determined by modelling the flow rate through the disruption mitigation valve to determine the number injected as a function of time. The data from MAST allows the calculation of both the average and time dependent fuelling efficiency, which are detailed in the following two sections. The two methods of calculating the fuelling efficiency are employed on different machines, the average method is used on ASDEX [56] where the CO_2 interferometer (of 10.6 μm wavelength) is able to measure past the thermal quench. However, on JET [61] and TEXTOR [110] the He interferometer cannot measure past the thermal quench, hence a time dependent method is used. The calculation of the fuelling efficiency with both methods allows for comparison across a larger range of tokamaks.

6.8.1 Average fuelling efficiency

The determination of average fuelling efficiencies requires line integrated density measurements throughout the discharge to enable an average density rise to be determined. The CO_2 interferometer on MAST is able to measure the density throughout the mitigation sequence without experiencing fringe jumps. Figure 6.22 shows a typical density measurement during the mitigation sequence.

As can be seen in figure 6.22, the increase in density is defined as the region where the density rises above the level prior to injection (dashed line). The fuelling efficiency is then calculated using equation 6.6 which is used for ASDEX [56, 62]. The chosen method allows direct comparison between the ASDEX and MAST results. The symbols in equation 6.6 can be defined as follows, a is the plasma minor radius, Δt_{eff} is the time for which the density is above the pre-injection level, $\Delta \int n_e dl$ is the change line integrated density (where the path length is $8a$), V is the plasma

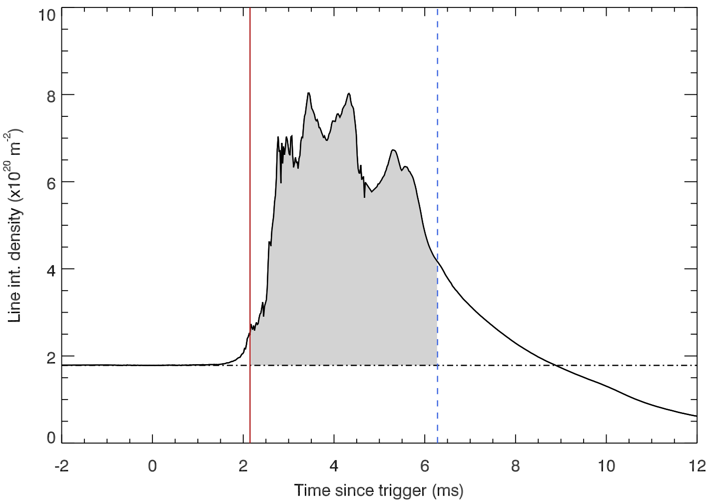

Figure 6.22: Line integrated density measurements during a mitigated discharge from the CO_2 interferometer as a function of time after the trigger. The thermal quench is shown by the solid vertical line and the offset of density is taken to be the density at the time of injection (dashed line) and the grey shaded region is integrated to give the increase in line integrated density as a result of mitigation.

volume as derived from EFIT reconstruction prior to injection, $t(TQ)$ is the time of the thermal quench, $t(CQ_{20})$ is the time at which the plasma current reaches 20% of the pre disruption value and n_{tot} is the total number of injected particles as determined from the calibration presented in chapter 5.

$$F_{eff} = \frac{V}{n_{tot}} \int_{t(TQ))}^{t(CQ_{20})} \frac{\Delta \int n_e dl}{8a} \frac{dt}{\Delta t_{eff}} \tag{6.6}$$

The use of the interferometer to determine the electron density increase requires that the interferometer produces results which are consistent with the measurements of the TS system for total particle inventory. The use of TS data to determine the density rise is not possible, as the TS system is unable to measure the density after the thermal quench accurately. The loss of accuracy is a result of the low plasma temperatures and due to the time resolution of the TS system in a single discharge compared to the interferometer. The calibration of the interferometer and the TS system can be performed by comparing the total number of particles at a given time using the TS density profile combined with the volume enclosed as a function of normalised flux (returned by EFIT) and the number calculated using the path length of the interferometer combined with the total plasma volume (from EFIT). The result of this analysis is that the interferometer overestimates the increase in the number of electrons by around 20% during steady state conditions, as shown in figure 6.23.

The averaged fuelling efficiency for a range of discharges with 10kJ $< W_{thermal} <$ 60kJ and $5 < q_{95} < 11$ produce average fuelling efficiencies of between 5 and 8%.

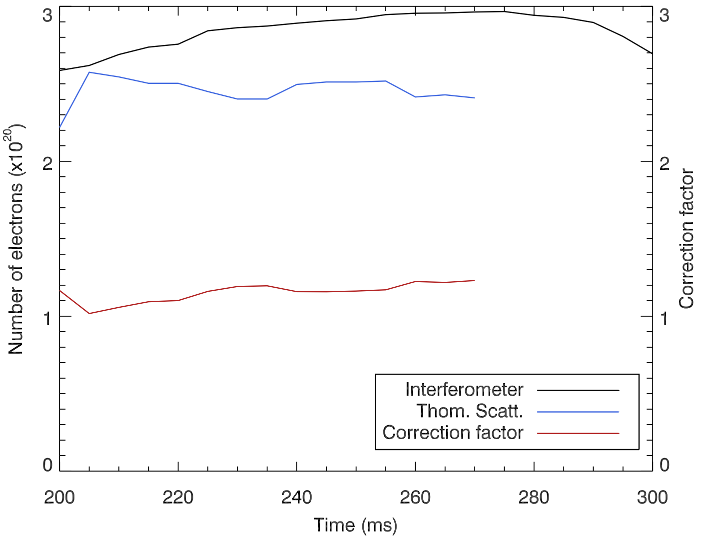

Figure 6.23: Calculation of the total number of electrons using Thomson scattering (TS) (blue line) and interferometry (black line) during discharge MAST#23598. The ratio of interferometer trace and the Thomson scattering trace is shown in red against the right hand axis. The interferometer returns a number around 20% higher than that calculated by the TS system in steady state.

There is no dependence of the average values on either q_{95} or stored thermal energy ($W_{thermal}$). It should be noted however, that the values of the fuelling efficiency obtained are lower than those seen on AUG [56] which range from 20 to 60% for discharges with thermal energies of 200-800 kJ and on DIII-D [62] where values range from 10 to 40% for helium, where the lower bound involves injection of a similar number of particles for both MAST and DIII-D.

One possible explanation for the low fuelling efficiency in MAST is the absence of a close fitting vessel wall. In conventional tokamaks, the volume occupied by the plasma and the vacuum vessel volume are comparable. As a result, when gas is injected into the vacuum vessel, the majority of that gas interacts with the plasma. The volume of plasma in MAST is of the order 10 m^3, compared to the vacuum vessel volume of 50 m^3. The extra space around the plasma provides a reservoir for the injected gas to occupy, without interaction with the plasma, thereby producing a lower fuelling efficiency. The wall also reflects neutrals back into the plasma, so for a close fitting wall the distance between leaving the plasma and re-entering it could be a few tens of centimetres, whereas on MAST it could be of the order metres.

The key factor in determining the energy deposited onto the divertor is the quantity of energy radiated prior to the thermal quench. The energy radiated will be determined by the amount of impurity mixing prior to the thermal quench, the assessment of which is not possible using an average fuelling efficiency.

6.8.2 Time dependent fuelling efficiency

The quantity injected prior to the thermal quench is important, as the thermal quench phase mixes the impurities with the core plasma. The mixing of the impurities with the core plasma raises the number of free and bound electrons, thereby providing runaway suppression [58, 62]. In addition, the larger amount of mixing prior to the thermal quench, then the more power will be dissipated via line radiation which will decrease the heat loads to the divertor targets when the thermal quench does occur [56, 62].

The determination of the fuelling efficiency at a given time requires the number of particles injected at that time to be estimated. Measurements performed using a DMV of a similar design to the MAST valve [104] have shown that the gas flow is self similar. The solution to the time dependence of a self similar flow has been derived in [107] and has been applied to model a MAST like valve in [118].

DMV flow model

The model from [118] gives the general expression (equation 6.7) for the fraction of particles delivered as a function of time $N_{frac}(t)$, where the symbols are defined as follows, A is the area of the pipe, x is the pipe length, $n = \frac{2}{\gamma-1}$, γ is the ratio of specific heats, V is the plenum volume, K is a correction factor and $\xi = \frac{x}{c_0 t}$ with c_0 the speed of sound and t the time since the triggering of the valve. The gases used for mitigation are noble gases and as such have $\gamma = 5/3$ and the total number of injected particles is N_0, this reduces equation 6.7 to equation 6.8 where N_inj is the number of particles injected as a function of time.

$$N_{frac}(t) = \frac{AKx}{V}\frac{n^n}{(n+1)^{n+1}}\sum_{k=0}^{n+1}\frac{(-1)^{k-1}(n+1)!}{(n-k+1)!k!}\left(1-\left(\frac{\xi}{n}\right)^{k-1}\right) \tag{6.7}$$

$$N_{inj}(t) = \frac{AKx}{V}\left(\frac{27}{256}\right)\left[\frac{3}{4\xi}+\frac{\xi}{2}-\frac{\xi^2}{9}+\frac{\xi^3}{12}-1\right] \tag{6.8}$$

The correction factor K was determined in [118] by comparison with experimentally measured flow rates from [104]. The model described above has also been used to analyse JET data [117] where a correction factor of 0.1 was used. The correction factor is used to estimate the amount of expansion of the gas from the plenum, through the orifice and into the pipe [118]. The model of the flow assumes that there is no such restriction on the flow, thereby requiring the use of a correction factor [107]. The determination of K by comparison to experimental data is not possible for MAST, as the orifice and pipe diameter are different from the JET and TEXTOR data. In order to estimate the appropriate correction factor, the ratio of the orifice and pipe diameters can be considered, which is around 0.07 on JET and 0.16 on MAST. Therefore, for MAST, K is taken to be double the JET value

($K = 0.2$).

The resulting flow rate into the vacuum vessel from equation 6.8 is shown in figure 6.24. The modelled flow rate shown in figure 6.24 shows that the injected gas reaches the edge of the plasma in approximately 0.75 to 1ms, which is consistent with observations of vacuum transit times. The number of injected particles (right hand axis in figure 6.24) is determined by multiplying equation 6.8 by the total number of particles in the plenum, N_0, which is determined by the pressure change in the injection plenum after injection and the volume of the plenum (65ml).

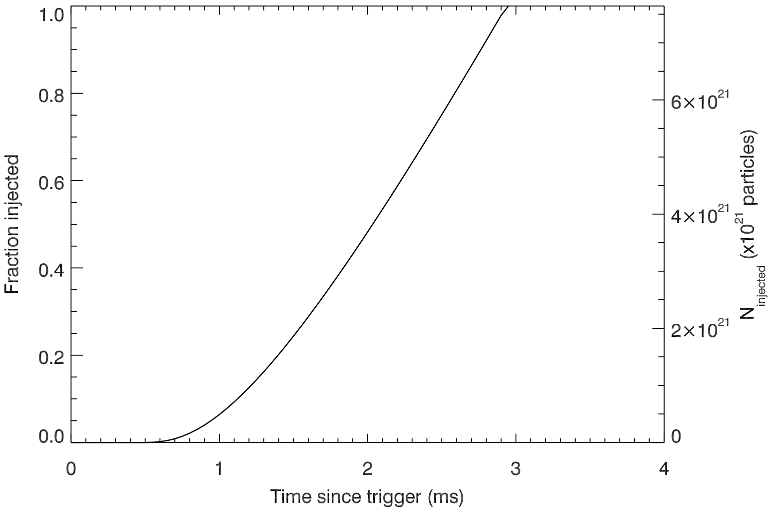

Figure 6.24: Modelled flow rate from the DMV using a pipe length of 1.8m, injection pressure of 5 bar(a), plenum volume of 65ml, helium injection and pipe diameter of 50mm. The left hand axis shows the rate as modelled by equation 6.8 and the right hand axis gives the number of particles injected assuming a fill pressure of 5 bar(g) (results in 4.9 bar(a) injected into the vessel due to valve efficiency).

The time dependent fuelling efficiency can be found using equation 6.6, with n_{tot} replaced with $N_0 N_{inj}(t)$ and the integral over the range $t(n >$ offset) to t as shown in figure 6.25 for a discharge with $W_{tot} = 240$kJ.

Figure 6.25 shows that the fuelling efficiency increases from the arrival of the gas at the edge of the plasma, through the thermal quench and reaches a maximum at the end of the thermal quench phase. The fuelling efficiency is 3% at the onset of the thermal quench for a discharge with $W_{tot} = 240kJ$ and q_{95} 5.5, with the majority of the impurity assimilation occurring during the thermal quench phase, which is consistent with the fast filtered imaging shown in figure 6.3 and reported in [62]. Recent results from Tore Supra [110] have shown that the pre-thermal quench fuelling efficiency can reach between 15 to 30% depending on the quantity of gas injected (after extrapolation to the thermal quench time) and significantly more gas is injected than in present MAST experiments.

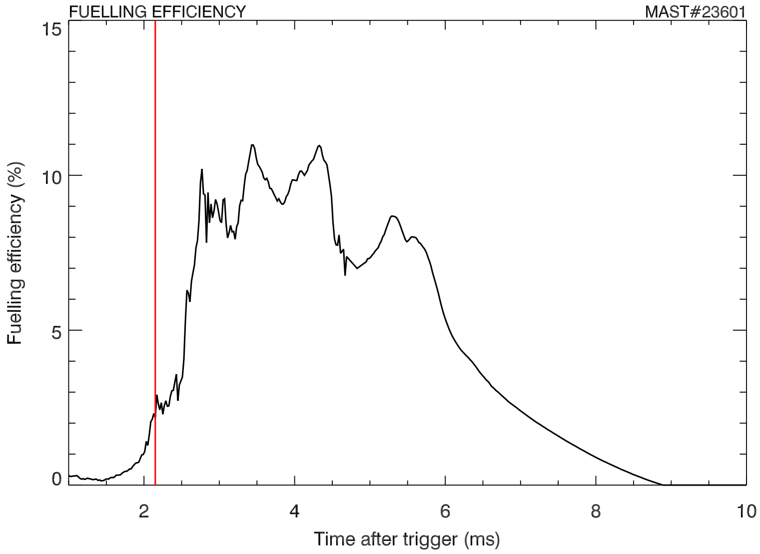

Figure 6.25: Calculated fuelling efficiency in discharge 23601. The vertical red line corresponds to the time of the thermal quench, as determined using SXR data.

6.8.3 Effect of q profile on fuelling efficiency

The discharges used to determine the dependency of mitigation timescales with q surface depth (section 6.7) can be used to determine the impact of the position of the q=2 surface on the fuelling efficiency. The delay between the thermal quench and the DMV trigger is seen to decrease for q surfaces which are located at larger radii. The thermal quench is triggered by the arrival of gas at the q=2 surfaces [60, 110], it would be expected that the longer the delay between injection and thermal quench then the more time there is for mixing and assimilation of the impurities with the bulk plasma. The increased time for assimilation should yield higher fuelling efficiencies for discharges where the q=2 surface is deeper in the plasma. The time dependent fuelling efficiency is shown in figure 6.26 with the location of the low field side q=2 radius shown in the key. The resolution of the interferometer data is of the order of the delay between surfaces at different locations, however, a general trend exists that shows the fuelling efficiency to increase with deeper q=2 surface depth. The fuelling efficiency at the end of the current quench for all the discharges (not shown in figure 6.26) reaches a peak value of between 6 to 8% regardless of q=2 location, which is consistent with the averaged fuelling efficiency (see section 6.8.1).

6.8.4 Effect of injected quantity on fuelling efficiency

The assimilation of impurities into the plasma as a function of injected quantity can be studied on MAST. The injected quantity on MAST can be varied between 5x10^{21} particles and 1.3x10^{22} particles, which are injected over a period of 8ms, as shown by the modelled flow rate in figure 6.27. The vertical lines on figure 6.27 indicate the delay between the triggering of the valve and the onset of the thermal quench for each

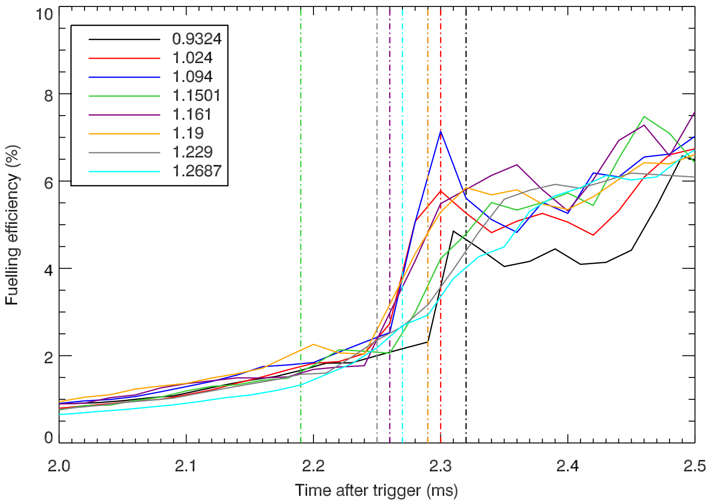

Figure 6.26: Time dependent fuelling efficiency as a function of q=2 depth prior to mitigation. The thermal quench onset is denoted by the dashed vertical line. The thermal quench time of the discharge with $r(q = 2) = 1.094$m overlaps with that at $r(q = 2) = 1.19$m.

discharge. It is clear from the onset of the thermal quench that a threshold appears to be present at which the thermal quench is triggered. Discharges where 5x10^{21} particles (3 bar injection fill pressure) are injected show that the time between the injection and the onset of the thermal quench is longer compared to higher injection levels. Once the injected quantity threshold has been reached, then the delay time becomes independent of the number of particles injected. Such a threshold is seen in JET MGI data, where the thermal quench onset is seen approximately 8.5ms after the trigger once the injection plenum pressure exceeds 17 bar in neon [117] and is also suggested by argon data in Tore Supra [110].

The threshold suggests that either, a certain quantity of gas must be assimilated into the plasma prior to the thermal quench or only a certain quantity of gas can interact with the plasma during injection. The interaction of a set quantity of gas can be ruled out as the data shown in figure 6.28, which shows that the fuelling efficiency at the thermal quench differs between discharges by approximately 0.1%. However, the noise present in the interferometer data (see figure 6.28 between 1.0 and 1.5ms) is of the order of 0.1% and the stored thermal energy in the discharges used is of the order 24kJ compared to 12kJ for the q scan discharges which have a higher fuelling efficiency which could obscure and dependence on the injected quantity . A limit on the quantity of gas which can interact with the plasma may arise from the large volume of the MAST vessel volume compared to the plasma volume which provides a reservoir for gas injected into the vessel. The initial pulse of gas arriving at the plasma will occupy the region between the end of the injection pipe and the plasma. The increased quantity of gas in this region will present an

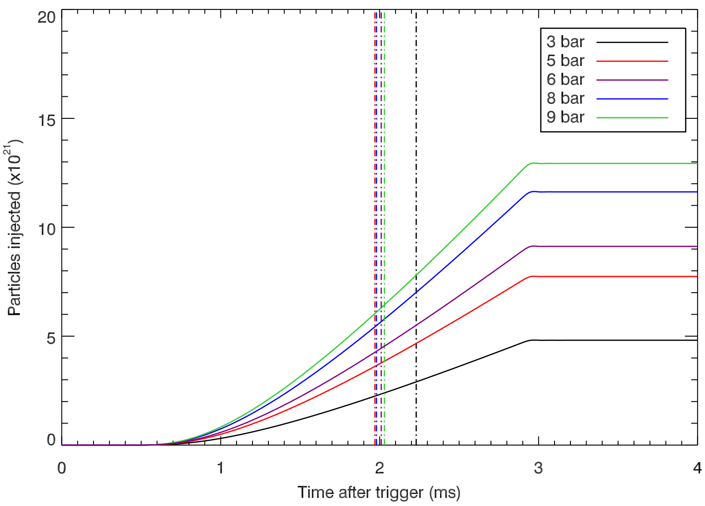

Figure 6.27: Modelled number of particles injected for various plenum pressures (in bar(g)). Thermal quench times for each injected quantity are shown by the dashed vertical lines.

obstacle to the later arriving gas, thereby preventing gas later in the injection pulse from propagating directly to the plasma edge from the pipe and causing it to fill the empty regions of the vacuum vessel.

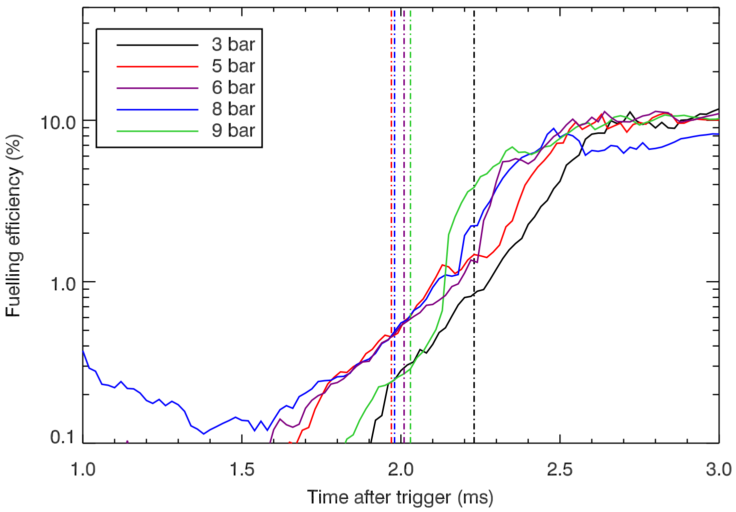

Figure 6.28: Fuelling efficiency as a function of time for various injected quantities. The dashed vertical lines correspond to the onset of thermal quench for each injection plenum pressure.

The constant fuelling efficiency as a function of injected quantity means the number of impurities ionised by the plasma must increase with injected quantity. The constant fuelling efficiency is a promising sign for ITER as the suppression of runaway electrons (REs) requires increased injection levels over the mitigation of heat loads. As the fuelling efficiency remains constant, then the injection level can be increased to supress the runaways without affecting the mitigation of the heat loads.

6.9 Summary

The mitigation of a discharge using MGI in MAST shows a sequence similar to that seen on other machines. The initial phases follow the recognised pattern of vacuum transit, followed by edge cooling which leads to the quenching of the thermal energy and finally the current. It has been shown that there is a role played by the q=2 surface in the mitigation sequence. The evidence for the involvement of the q=2 surfaces is seen through the use of fast camera data, in delay times for mitigation depending on the location of the q=2 surface. The strongest evidence for the involvement of the q=2 surface is seen in the increased density seen on the q=2 surface in the moments leading up to the thermal quench. It has also been seen on the Thomson scattering data that other rational surfaces are involved, in particular q=3 which also shows a density build up during the cooling phase of the mitigation.

The fuelling efficiency has been seen to depend on the location of the q=2 surface and the number of particles injected. Of critical importance to the concept of a Component Test Facility (CTF), an ST based future tokamak, it has been seen that thermal quenches occur on quicker timescales than in conventional tokamaks, likely as a result of the strong shear at the edge of the plasma. The rapid onset of the thermal quench after injection has important consequences for mitigation in a CTF. The rapid onset decreases the amount of time for mixing of impurities with the plasma, leading to low fuelling efficiencies. The observation of low fuelling efficiencies means that the mitigation of heat fluxes, current quench timescales and runaways may be less effective than in conventional machines.

Chapter 7

Effect of Massive Gas Injection

The purpose of this chapter is to make an assessment of the loads and stresses generated during a mitigated disruption and compare them to the loads and stresses produced during unmitigated disruptions (see chapter 4).

7.1 Defining a standard disruption

An unmitigated disruption reference has been chosen using the following criteria. Firstly, the disruption must occur at maximum performance as set out in chapter 4 and it must be repeatable. Secondly, a discharge with a high power loading is required to allow accurate assessment of the heat load reduction. To this end, a beam heated discharge is chosen over an ohmic discharge. The addition of beam power enhances the power load, but also increases the soft X ray signal over ohmic discharges. The increased soft X ray signal allows accurate determination of the thermal quench time.

A suitable discharge was chosen by searching a database of MAST disruptions which was compiled in chapter 4. The chosen discharge had been previously repeated and was found to disrupt reliably at around 300ms as a result of a large n=1, m=1 mode growing in the plasma. The basic plasma parameters of the chosen discharge are shown in figure 7.1.

The mitigated discharge was produced by repeating the chosen unmitigated disruption and injecting 0.4 bar litres of a 10% Argon 90% Helium mixture prior to the onset of the disruption in the unmitigated case. It can be seen from figure 7.1 that the unmitigated and mitigated disruption are well matched in terms of plasma current, electron density and, in part, stored thermal energy. The loss of the stored thermal energy in the discharge without mitigation is due to the decrease in external heating power as the neutral beams must be turned off 15ms prior to the DMV trigger (figure 7.1, panel d). Beam heating cannot be applied during mitigation to prevent damage to the NBI system, as discussed in chapter 5. The loss of stored thermal energy amounts to approximately 10-15% of the maximum stored thermal energy in the discharge. However, it is important to note that the stored

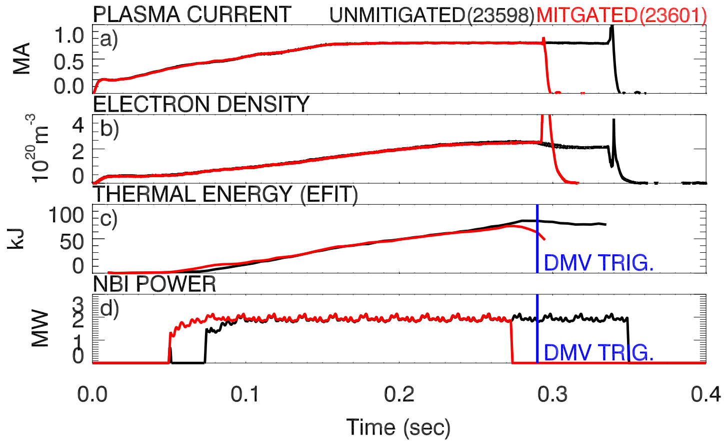

Figure 7.1: Basic plasma parameters of the unmitigated (black traces) and mitigated (red traces) chosen to perform an assessment of the efficacy of disruption mitigation.

magnetic energy in both discharges amounts to 175kJ, substantially more than the stored thermal energy. The loss in total stored energy ($W_{tot} = W_{thermal} + W_{magnetic}$) resulting from the early beam turn off is approximately 9% W_{tot}, this combined with the confinement time of MAST which is 20-30 ms and that there will still be fast particles slowing down after the beam is turned off [119] mean that this loss is likely insignificant.

7.2 Infra red data analysis

Assessment of the heat loads to the divertor and energy balance during a disruption forms a key part of this chapter. Measurements of these loads can be performed using infra red (IR) thermography. The key points of IR data analysis are detailed in this section.

7.2.1 Theory

Planck's law gives the power emitted from a black body, per steradian as a function of wavelength and body temperature. This is known as the spectral radiance, $I(\lambda, T)$, and is shown in equation 7.1.

$$I(\lambda, T) = \frac{2hc^2}{\lambda^5} \frac{1}{e^{\frac{hc}{\lambda kT}} - 1} d\lambda \tag{7.1}$$

The flux of photons from a black body in a given wavelength range, $\Phi_{photons}$, can be found by dividing equation 7.1 by the energy of one photon and integrating over the wavelength range of the camera (equation 7.2). The measurement of the photon flux from the material surface using an IR camera allows the surface temperature of the material to be determined using equation 7.2.

$$\Phi_{photons} = \epsilon \int_{\lambda_1}^{\lambda_2} \frac{2\pi c}{\lambda^4} \frac{1}{e^{\frac{hc}{\lambda kT}} - 1} d\lambda \tag{7.2}$$

The degree to which a particular object is a black body can be expressed using the objects emissivity, ϵ, with a perfect black body having $\epsilon = 1$ and a grey body possessing a constant emissivity over all wavelengths. MAST uses graphite as a divertor material, which is a grey body with $\epsilon \approx 0.7$ [120].

Changes in surface temperature are caused by a heat flux falling onto the surface. The heat flux to a surface, $\vec{q}$, can be obtained from Fourier's law of conduction (equation 7.3) which relates the temperature gradient in a material with a thermal conductivity, k, to the heat flux flowing through it.

$$\vec{q} = -k\nabla T \tag{7.3}$$

The heat transfer equation (7.4) relates the heat flux to the temporal evolution of the surface temperature. Infrared thermography measures the temporal evolution of the surface temperature, hence it provides the left hand side of equation 7.4, where ρ is the density of the material and C_p is the heat capacity of the material.

$$\rho C_p \frac{\partial T}{\partial t} = -\nabla \cdot \vec{q} \tag{7.4}$$

The substitution of Fourier's law into the heat flux transfer equation (equation 7.5) allows the temperature, $T(x,t)$, as a function of depth into the material to be calculated. The heat flux can then be obtained from the temperature profile using equation 7.3 [121].

$$\frac{\rho C_p}{k} \frac{\partial T}{\partial t} = \nabla^2 T \tag{7.5}$$

It is important to note that the conductivity, k, and the heat capacity, C_p, in equation 7.5 are not constant but are functions of the temperature [122]. Therefore the solution of equation 7.5 is performed using the introduction of a integral transform, known as the heat flux potential, $U(T)$, which is defined in equation 7.6 [122].

$$U(T) = \int_{T_e}^{T} k(T)\, dT' \tag{7.6}$$

The use of a heat flux potential simplifies the equations to be solved to those shown in equations 7.7 to 7.9. The heat transfer code THEODOR [122] is used to solve these equations using a finite difference approach. The boundary conditions are taken to be the temperature on the surface of the tile, as measured by IR thermography and the temperature at the back of the tile which is taken to be room temperature.

$$\frac{\partial U}{\partial t} = D\nabla^2 U \tag{7.7}$$

$$q = -\frac{\partial U}{\partial x} \tag{7.8}$$

$$D(T(U)) = \frac{k}{\rho C} \tag{7.9}$$

7.2.2 Limits of IR thermography

The accuracy of IR thermography in determining the temperature of a surface is fixed by the signal to noise ratio of the recorded data. In IR thermography, noise can be generated by three main sources, reflections from hot surfaces, bremsstrahlung from the plasma and radiation from recombination.

Reflections and recombination

The reflection of IR radiation from hot regions onto the monitored surface and the production of radiation from recombination both cause the overestimation of the heat flux, it is a particular problem for devices with closed divertors such as ITER [123]. The reflection of heat flux onto the divertor requires hot surfaces in proximity to the strike points. The open design of the MAST divertor and vessel prevents this from occuring, thereby minimising the error caused by reflection. The radiation from recombination is also minimised due to the open divertor design which provides effective pumping of neutral particles. As a result, reflection and recombination are not thought to greatly affect the IR measurements on MAST.

Bremstrahlung

Bremsstrahlung radiation emitted by the plasma can also affect IR measurements [124]. The effect of bremsstrahlung is a concern for massive gas injection for two main reasons; the injection of a large number of impurity particles increases the effective charge of the plasma which increases the amount of bremsstrahlung present and the closed nature of tokamak divertors prevents direct lines of sight to the strike points. In other tokamaks (e.g. JET, Tore Supra and TEXTOR) the strike points are generally viewed by looking down through the plasma at the divertor, which increases the likelihood of bremsstrahlung affecting the measurements.

The open nature of the MAST divertor allows direct imaging of the strike points, and as such the effect of bremsstrahlung should be limited. The impact of bremsstrahlung, or other background emission, such as recombination, on IR measurements can be analysed by studying areas of the divertor where the power load is not expected to reach. The MAST divertor is built of individual tiles, which are inclined at 4 degrees to horizontal (see chapter 3). The tiles are arranged in such a way that there is a gap between each tile and a region of the tile shadowed from plasma impact. A section of a raw IR camera image is shown in figure 7.2, which shows a point in the tile gap (red circle) and a point in the shadowed region (blue triangle).

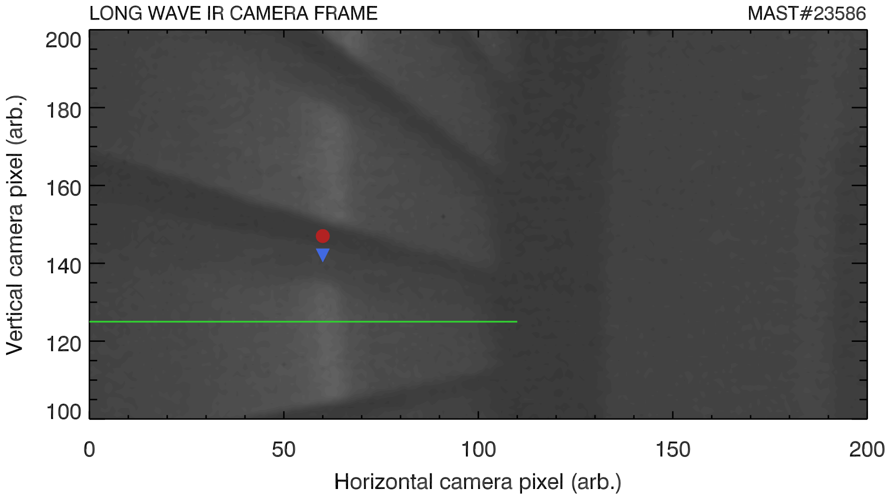

Figure 7.2: Raw data from the long wave infra red camera. The view shows a section of the upper divertor. The camera is oriented in such a way that the image is rotated by 90 degree anticlockwise. The red circle is a point in the tile gap and the blue triangle is a point in the shadowed region of the divertor tile. The green line denotes the analysis path used to generate the heat flux to the divertor target.

The intensity of the recorded IR images in the tile gap indicates the level of background emission present, as no power should fall into the tile gap. The intensity of the two points on the divertor and the peak intensity along the IR analysis line is shown in figure 7.3.

The analysis shows that background emission is not a significant problem during disruption mitigation in MAST. The peak signal in the tile gap amounts to only 3.5% of the peak signal along the analysis path. The reason for this is the direct view of the strike points made possible by the open divertor design which minimises the effect of bremsstrahlung. There is an increase in intensity in the shadowed region during the disrupting phase, this is due to the loss of equilibrium during the disruption, which causes the magnetic geometry of the plasma to change.

Surface layers

A major problem which affects all IR measurements is the production of negative heat fluxes (figure 7.4). The negative heat fluxes are generated during transient events when there is rapid heating of the surfaces. The negative heat fluxes are seen as the surface cools after being exposed to a sudden heat flux. The surface appears to cool more rapidly than would be expected from the thermal properties of the material, it is this effect which makes it look as though heat is being extracted from

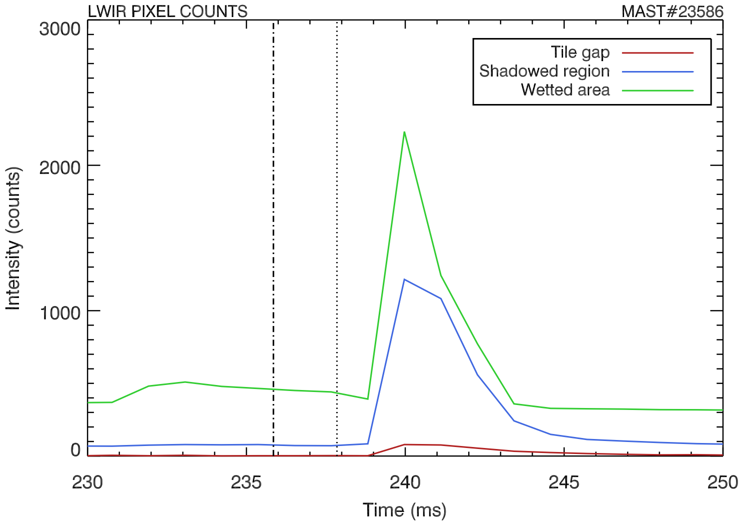

Figure 7.3: Infra red image intensity as a function of time for the point shown on figure 7.2. The intensity has been background subtracted using the pixel intensity at t=0 from the tile gap. The dot dashed line marks the DMV trigger time and the dotted line marks the thermal quench time.

the surface (hence negative heat flux) [88, 120, 125]. The phenomenon was first detailed in [125] where the cause was suggested to be the presence of a thin layer on the surface of the material which is in poor thermal contact with the bulk material. It has also been suggested that the surface layer is formed by the deposition of carbon onto the divertor surfaces [126] or alternatively the presence of dust and surface inhomogeneities [127, 128].

A surface layer parameter, α, can be introduced into the heat flux calculation by adding a correction to the measured temperature. The surface layer reaches a temperature which is above the bulk temperature by q/α, where α describes the change in the surface layer temperature due to a heat flux. The bulk temperature is given by equation 7.10.

$$T_{measured} = T_{bulk} + \frac{q}{\alpha} \tag{7.10}$$

The elevated temperatures reached by the surface layers means that they emit at shorter wavelengths than the bulk material, as a result the effect of surface layers can be minimised by using long wave (7-9 μm) imaging [127, 129]. The LWIR camera on MAST is less affected by the surface effects and therefore gives a means of estimating the impact of the surface layers [127, 128]. On MAST the effect of surface layers has been determined by observing the same region with the two cameras and deriving the heat flux. The alpha value on the cameras can then be adjusted to eliminate the negative heat fluxes whilst maintaining parity between the MWIR and LWIR cameras. The alpha values obtained are 60-70 kWm^{-2}K^{-1} for the LWIR camera and 30 kWm^{-2}K^{-1} for the MWIR camera [128].

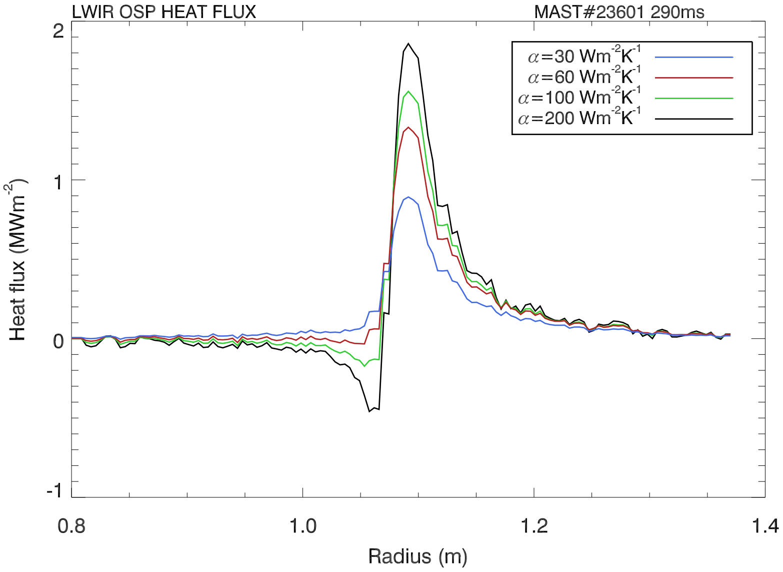

Figure 7.4: Divertor heat load radial profile during steady state operation at 0.290s in MAST#23601. The negative heat fluxes can be seen for large values of α. The optimum value of α (red trace) produces no regions of negative heat flux. The optimum α gives a heat flux of zero after the thermal quench occurs (not shown).

Field of view

The final source of error on IR measurements is the heat flux falling outside the field of view of the camera. The strike point width broadens significantly during a disruption (see chapter 4) which can cause the heat flux to extend beyond the imaged region. The heat flux may also fall on unmonitored vessel components, especially during vertical displacement events. The effect will be the underestimation of the energy deposited onto the divertor.

7.3 Power loads during mitigation

Measurements of the divertor temperature have been performed using IR thermography for the discharges shown in figure 7.1. The data collected allows a direct assessment of disruption mitigation on divertor power loadings. A comparison of the power load to each of the four strike points is shown in figure 7.5, panels c) to f). The power load is calculated by integrating the heat flux onto the divertor surface, assuming the heat flux is toroidally symmetric.

Soft X ray data during the unmitigated disruption (figure 7.5 panel b)) shows a sudden thermal quench of duration 0.3ms. The short timescale of the thermal quench gives rise to a rapid increase in divertor power load at a rate of 200 MW/ms. The sudden rise is then followed by a drop in power, once the thermal energy has been exhausted from the plasma.

The secondary rise in divertor loading occurs during the current quench, at a time consistent with the loss of vertical control within the plasma. The presence of the second peak on the lower divertor suggests that the plasma remains in a double null configuration up to this point. During the VDE event, the discharge transitions to single null, as evidenced by the decreased power loadings to the lower divertor (panels d) and f) from T=2ms). Vertical motion into the upper divertor continues during the remaining part of the current quench, producing the slowly decaying power load onto the upper targets (panels c) and e) from T=2ms). Peak power loadings occur on the outer strike points of 30MW, which are approximately ten times that of the inner strike points at 4MW. The total duration of the power load is 8ms.

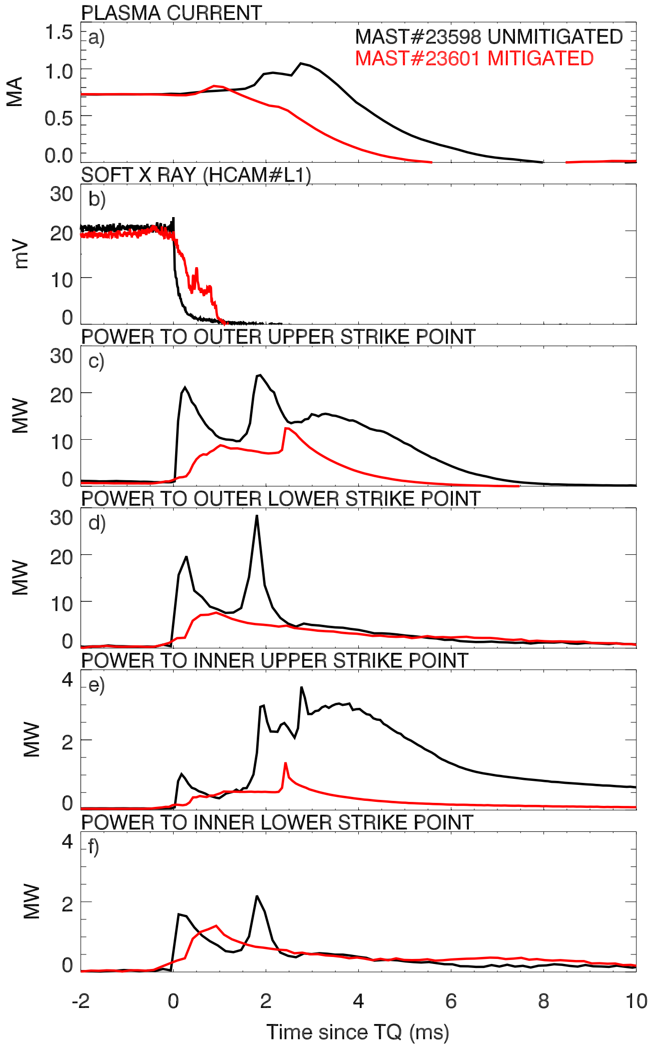

Figure 7.5: Divertor power loads during unmitigated (black) and mitigated (red) disruptions. The soft X ray trace for both discharges is shown (panel b)) to identify the onset of the thermal quench. The time is shown normalised to the onset of the thermal quench (TQ). The power to each target (panels c) to f)) is calculated by integrating the heat flux over the target area and assuming the heat flux to be toroidally symmetric. The sample rate of the upper divertor data is 13.5kHz and 6kHz for the lower divertor data.

In the mitigated case the duration of the thermal quench is increased over the unmitigated case. The slower thermal quench in the mitigated case leads to a slower rise in the power to the divertor, with the thermal energy being deposited in approximately 1ms from the start of the thermal quench.

The mitigated plasma remains vertically stable for approximately 1ms longer than the unmitigated case. The loss of vertical control occurs at T=2.5ms, giving rise to a second peak in the power load on the upper divertor surfaces only (figure 7.5, panels c) and e)). The absence of a peak in the power load at T=2.5ms on the lower divertor suggests that the VDE event occurs when the plasma is in a single null configuration.

The overall duration of the power load onto the divertor is 6ms and the peak power loads are reduced to 10MW on the outer divertor and 1.5 to 2MW on the inner divertor.

7.3.1 Radiated power

The radiated power during the disruption is shown in figure 7.6. The time resolution of the bolometry data prevents the separation of the thermal quench and current quench stages. The time resolution is limited by the smoothing required to analyse the data. The effect of the smoothing can be seen in the mitigated data which shows an increase in radiation prior to the triggering of the DMV at T=−3ms.

Mitigated discharges radiate more of the stored energy prior to the thermal quench. The energy radiated prior to the thermal quench in the unmitigated case is 2.4 kJ, which amounts to 1% of the total stored energy. The mitigated disruption dissipates 10% of the total stored energy prior to the thermal quench. The duration of the radiating phase is comparable in both mitigated and unmitigated discharges, lasting approximately 10ms. However, the mitigated case generates five times the radiated power of the unmitigated case.

7.4 Energy balance

The balance of energy during the disruption can be followed during the disruption. The initial stored energy ($W_{thermal} + W_{magnetic}$) in the plasma can be found using EFIT reconstruction. The energy delivered to the divertor and radiated can then be found using the divertor and radiated power.

The disruption of energy before and after the disruption can be seen in figure 7.7 for an unmitigated disruption and figure 7.8 for a mitigated disruption. The unmitigated case was repeated twice and the mitigated case six times. The stored, radiated and divertor power for the mitigated and unmitigated cases can be seen in table 7.1. There is minimal variation in the radiated and divertor energy load in the mitigated discharges which suggest that the process of mitigation is reproducible.

Overall, approximately 80% of the energy before the disruption is accounted for

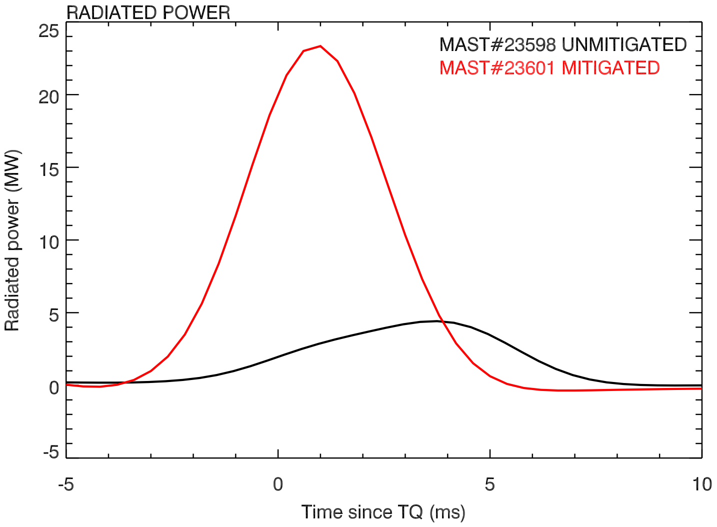

Figure 7.6: Radiated power loads during unmitigated (black) and mitigated (red) disruptions. The time is shown normalised to the onset of the thermal quench (TQ). The sample rate of the bolometer system is 2.5kHz.

by the radiated and divertor energy load. The level of accountancy is in agreement with the 91% ±6% seen in chapter 4. The unaccounted energy could be included in the error associated with the divertor power load measurements, or it could be dissipated in the vacuum vessel and poloidal field coil s.

The mitigated disruption sees a rise in radiated power to 40% W_{tot} compared to the 10% W_{tot} in the unmitigated case. The rise in radiated power is reflected by a corresponding fall in divertor energy loading in the mitigated case to 43% W_{tot} from 70% W_{tot} in the unmitigated case. The 30% reduction in energy loading has not been optimised by tailoring the type and quantity of gas injected.

	Unmitigated	Mitigated
W_{total}	260kJ	240kJ
$W_{thermal}$	70kJ	60kJ
$W_{magnetic}$	190kJ	180kJ
$W_{divertor}$	180kJ	100kJ
$W_{radiated}$	25kJ	90kJ

Table 7.1: Indicative values for the energy balance between the energy stored in the plasma prior to disruption and the energy removed from the plasma. The data is compiled from repeated discharges. The standard error in the radiated and divertor energy is ±25% and ±10% for the total, thermal and magnetic energy.

The radiated fraction and divertor energy loading in all the mitigated discharges exhibits the same trend as the comparison discharges above, where 40% of the total stored energy is deposited to the divertor and the same fraction is radiated (figure 7.9). The plot below can be directly compared with figure 4.12 which shows the energy balance in full performance disruptions derived from the disruption database in chapter 4. The radiated fraction of the total stored energy is consistent with

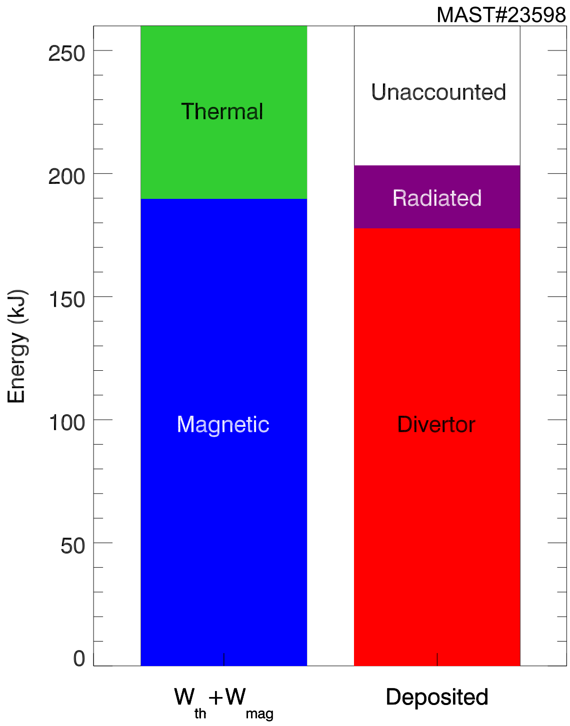

Figure 7.7: Energy balance before and after an unmitigated disruption. The left hand bar shows the total EFIT stored energy prior to disruption and the right hand bar shows the energy balance after disruption. Data is calculated from discharge MAST#23598.

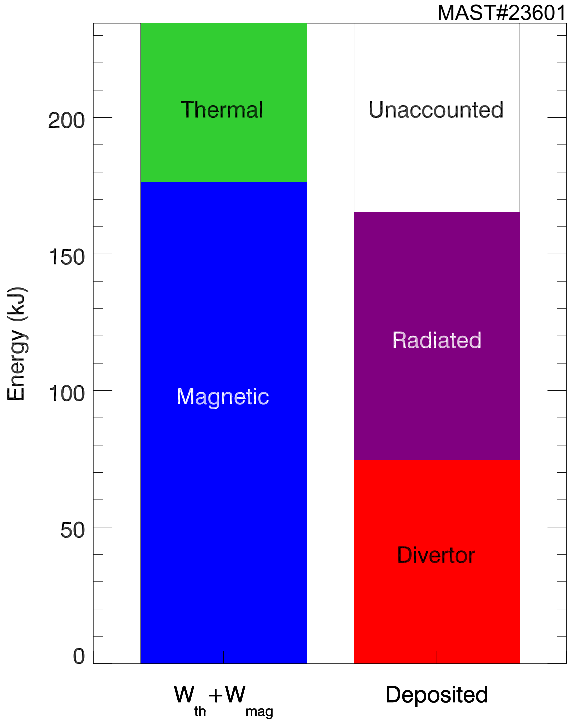

Figure 7.8: Energy balance before and after a mitigated disruption. The left hand bar shows the total EFIT stored energy prior to disruption and the right hand bar shows the energy balance after mitigation. Data is calculated from discharge MAST#23601.

results from C-Mod [58], where increased energy loss via radiation has been achieved using pure neon and argon injection (figure 2.11).

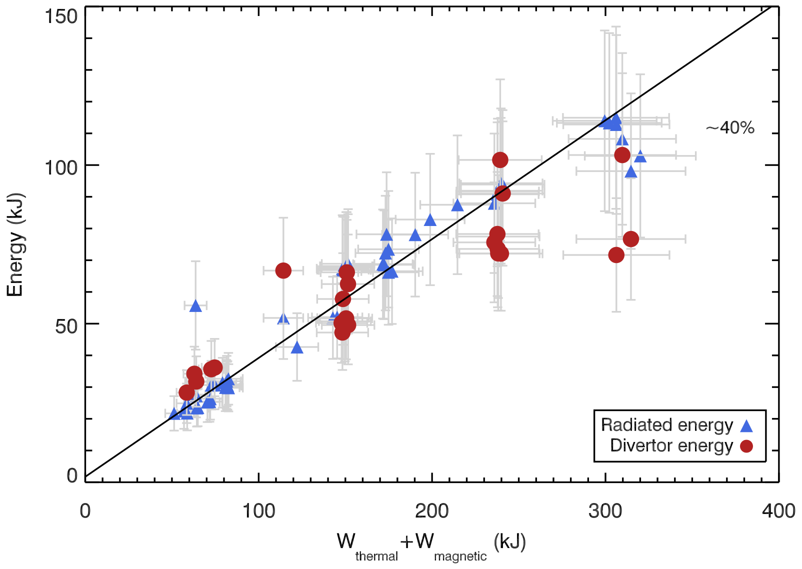

Figure 7.9: The amount of energy radiated and delivered to the divertor during mitigated disruptions. The fit to the data shows that the radiated energy and divertor energy amount to 40% of the total stored plasma energy during mitigated disruptions (solid line). The figure can be compared to figure 4.12 which shows the same data for unmitigated disruptions in MAST.

The power accounting available in MAST, where all of the four strike points are observed, makes possible an extrapolation to ITER which would otherwise be difficult to obtain from data published by other machines. The stored thermal energy in ITER is 350MJ [23] of which it is assumed that 100% is deposited onto the divertor during a disruption. The area over which the energy is deposited is 25m^2, which assumes a seven fold broadening in the plasma wetted area during disruption (table 6, [23]). The thermal quench time in MAST during a mitigated disruption is seen to take approximately 1ms (see figure 6.1 and panel b), figure 7.5), compared to 0.3ms in the case of an unmitigated disruption (figure 4.7). ITER assumes a linear scaling in thermal quench timescale with minor radius. If this scaling is used to determine the mitigated thermal quench time in ITER from MAST data, then the lower limit on the thermal quench timescale, τ_2, is 3.3ms. The projected energy load, assuming 40% of $W_{thermal}$ is deposited in 3.3ms, is 97 MJ m^{-2}s$^{-0.5}$. Whilst this load exceeds the tolerable limit for tungsten and carbon by 60%, it is significantly lower than the upper limit during an unmitigated disruption of 446 MJ m^{-2}s$^{-0.5}$, which uses the lower limit on τ_2 and there is scope for improvement by varying the mitigation species as seen on other tokamaks [41, 58, 130]

7.5 Heat load asymmetry

Infra red camera data and Langmuir probe (LP) data can be used to assess the toroidal symmetry of the heat loads during mitigated disruptions. The IR cameras can be adjusted to give a wide field of view at a decreased frame rate. The expanded field of view allows five divertor tiles to be viewed simultaneously which cover a toroidal angle of 30 degrees (see figure 7.10) at a time resolution of 1.2ms.

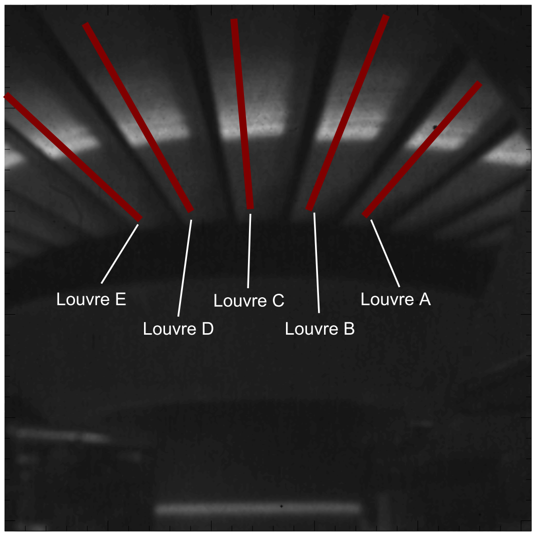

Figure 7.10: IR camera view showing the louvres used to analyse the heat load asymmetry. The view is of the upper divertor, with louvres A,B and C in sector 1 and louvres D and E in sector 2. The red lines represent the analysis region for each louvre. The each louvre has a toroidal displacement of 7.5 degrees.

Langmuir probe data is available from three sectors, covering a toroidal displacement of 120 degrees. Measurement of the ion saturation current only for each probe allows a set of profiles from each sector to be collected every 0.7ms. The ion saturation current density is related to the heat flux, q, onto the divertor by the equation $q = \gamma T_e J_{sat}$, where J_{sat} is the ion saturation current divided by the probe area, T_e is the electron temperature in eV and γ is the sheath heat transmission coefficient (typically 7-8).

The time resolution of the LP and the IR cameras is insufficient to allow analysis of the heat load asymmetry during the thermal quench of an unmitigated disruption which occurs on a timescale of 0.3ms (see chapter 4). The timescale of the thermal quench in a mitigated disruption is of the order 1ms (figure 6.1), which is the approximate temporal resolution of the IR and LP diagnostics.

Langmuir probe data during an ohmic discharge is shown in figures 7.11 to 7.13. The data is derived from a repeat of the ohmic discharge shown in figure 6.1. The thermal quench time in this discharge occurs at 0.238ms, which corresponds to T=2ms in figure 6.1. The current quench is initiated at 0.239ms with the current decaying away by 0.242ms. The LP data from one sector is composed of data from three amplifiers with each amplifier covering a specific range of radii. The resolution of the LP data varies across the sector, with the highest resolution between 1100mm and 1200mm. The data from the LP is affected by electromagnetic interference during the disruption, which occasionally prevents the signal being recorded. The interference can be seen in figures 7.11 to 7.13 when the J_{sat} values exhibit a sudden drop. The centre amplifier on sector 8 is faulty throughout the data set.

The data before the thermal quench (figure 7.11) shows strike point splitting on all sectors, of between 5 and 10cm which suggests the presence of a locked mode in the phase leading up to the disruption, as previously discussed (see section 6.5). The onset of the thermal quench is marked by a rise in the ion saturation current and a broadening of the profile (figure 7.12). The ion saturation shows a high degree of toroidal symmetry outside the private plasma region (see figure 1.3 for details) during this phase of the disruption. The strike point inside the private plasma region shows variation in the current of approximately 50%.

The LP data at the end of the thermal quench (figure 7.13) shows that the heat flux has increased over the onset of the thermal quench, but remains largely toroidally symmetric. The heat flux now falls outside the range observed by the LP. The peak heat flux measurements are obtained at 0.240ms (not shown), which is the point at which the plasma becomes vertically unstable and interacts with the upper divertor. The motion of the plasma into the divertor generates heat loads which are toroidally symmetric and subside over the next four milliseconds.

The heat flux to the divertor does not rise on the IR data until 0.240ms and then decays in time, suggesting that the time resolution of the IR data is insufficient to resolve the thermal quench phase. The IR data supports the LP data in the toroidal symmetry of the heat load during the mitigated disruption (figure 7.14). The IR data is from discharge 23586 from which 23595 is a repeat.

7.6 Power loading dependence on N_{inj} and q_{95}

Figure 7.15 shows the radiated energy and divertor energy load as a function of increased injection quantity. The energy load to the divertor is derived from lower IR camera measurements only due to the upper measurements being unavailable. The discharges are double null in character, it has been shown that there is even balance between the energy delivered to the upper divertor and lower divertor in L mode discharges [128]. It can be assumed that the total energy load to the upper and lower divertor is twice the amount shown in the figure. The divertor and radiated energy loads are consistent with the data obtained from other discharges which show 40% of the total energy is lost via radiation and deposition onto the divertor. Increased injection quantity appears to have no effect on the energy deposited or radiated. Due to technical reasons, the explored range of injected quantity is only 25% of the maximum capacity of the DMV system and further experiments should be performed to investigate if this trend persists.

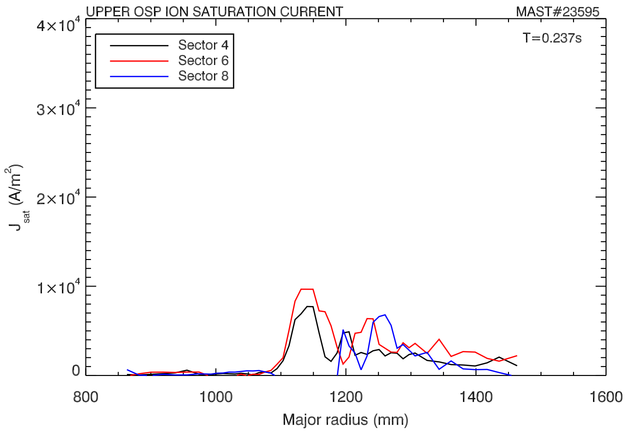

Figure 7.11: Langmuir probe data during MAST#23595 at 0.237ms, one millisecond prior to the onset of the thermal quench and two milliseconds after the DMV trigger.

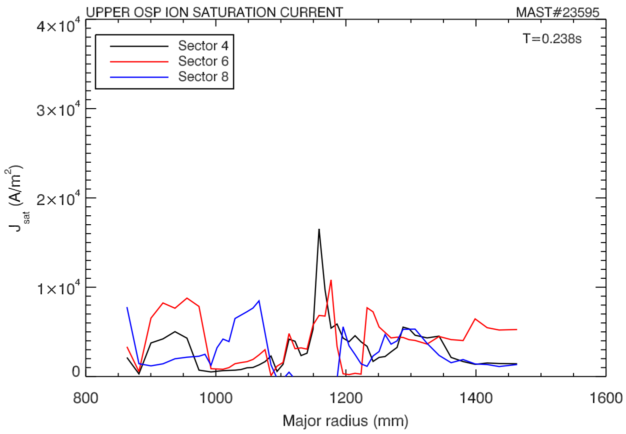

Figure 7.12: Langmuir probe data during MAST#23595 at 0.238ms, at the onset of the thermal quench and three milliseconds after the DMV trigger.

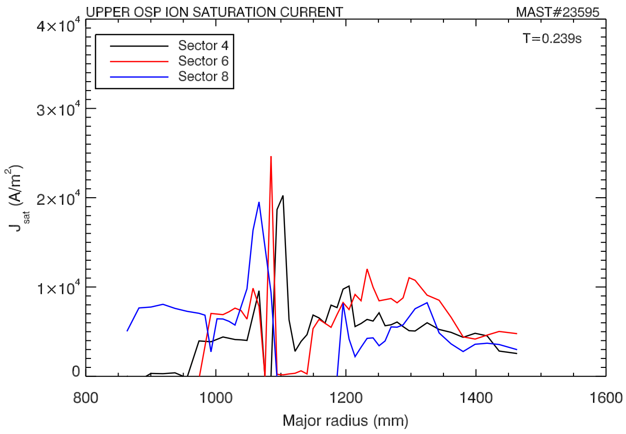

Figure 7.13: Langmuir probe data during MAST#23595 at 0.239ms, one millisecond after the onset of the thermal quench and four milliseconds after the DMV trigger.

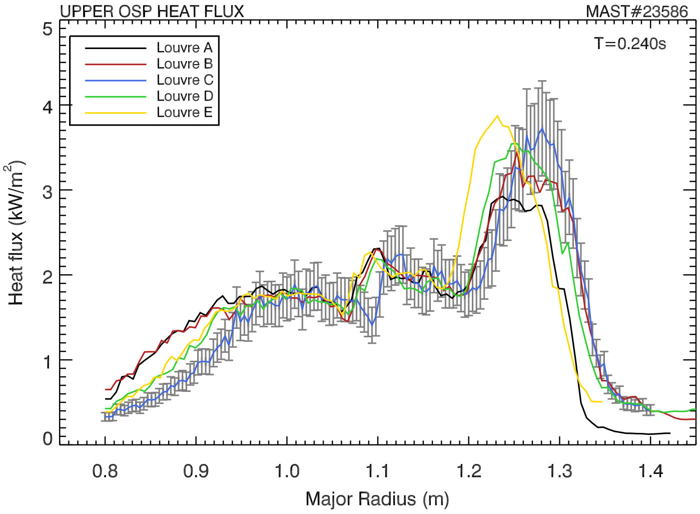

Figure 7.14: Divertor heat load during MAST#23586 at 0.240ms derived from infra red camera data at various toroidal locations (see figure 7.10). The variation in toroidal angle between louvre A and louvre E is 30 degrees.

The power load to the lower divertor is also unaffected by variation in q_{95}. It may have been expected that the deeper the region between the LCFS and the q=2 surface, the larger the fraction of energy which could be radiated prior to the onset of the thermal quench [60], however this is not seen in figure 7.16. The energy deposited onto the lower divertor surface amounts to between 20 to 40% of the total stored energy and the radiated fraction is 40% independent of q_{95}.

The reference discharge is the same for all of the q scan data. The reference discharge is further toward an upper single null (USN) geometry than the other discharges shown, with a separation between primary and secondary X point of approximately 2cm, compared to 0-1cm for the other discharges. The higher separation would suggest that the majority (>75%) of power is delivered to the upper divertor [128] which should give rise to lower divertor power loadings of approximately 10-15% assuming 40% of W_{tot} is radiated. The data in figure 7.16 is significantly higher than this.

The discrepancy between the expected power load and the recorded level to the lower divertor arises for two reasons. The USN geometry acts to lower the power delivered to the lower divertor, which increases the signal to noise ratio; the MWIR data is affected by noise significantly more than the LWIR. As a result, the identification of the end of the heat pulse is more challenging when performed using an algorithm which gives rise to the overestimation. The second factor is the low stored thermal energy of the discharges which decreases the heat load further when compared to other reference discharges. The error bars shown go some way to reconcile the overestimation.

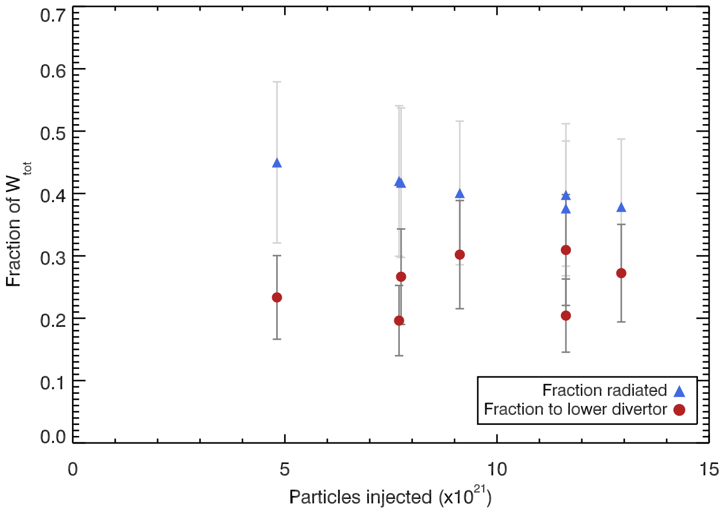

Figure 7.15: The fraction of the total stored energy radiated and deposited onto the divertor as a function of the number of particles injected.

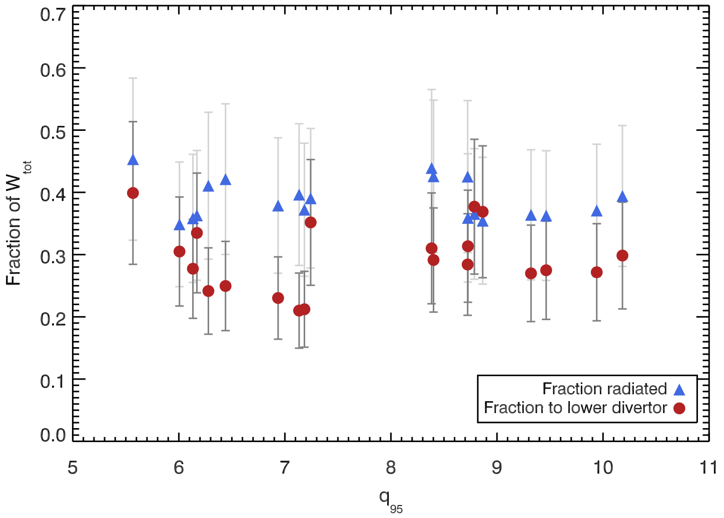

Figure 7.16: The fraction of the total stored energy radiated and deposited onto the divertor as a function of q_{95}.

7.7 Current quench

The current quench time can be determined using the definition used in chapter 4. The data shown in figure 7.17 shows the area normalised current quench time as a function of plasma current density. The black dots represent the data presented in chapter 4, which show the splitting of the current quench time as a result of the modifications made to MAST in 2004. It is clear from the mitigated points (red circles) that mitigation decreases the current quench timescales. The decrease in current quench time is expected as the impurities will act to increase the plasma resistance, as $\tau = L/R$ this explains the decrease in the current quench timescales. It has previously been shown [100] that spherical tokamaks, due to the lower inductance, exhibit current quench times which are faster than the allowable threshold for ITER of 1.67 ms m^{-2}.

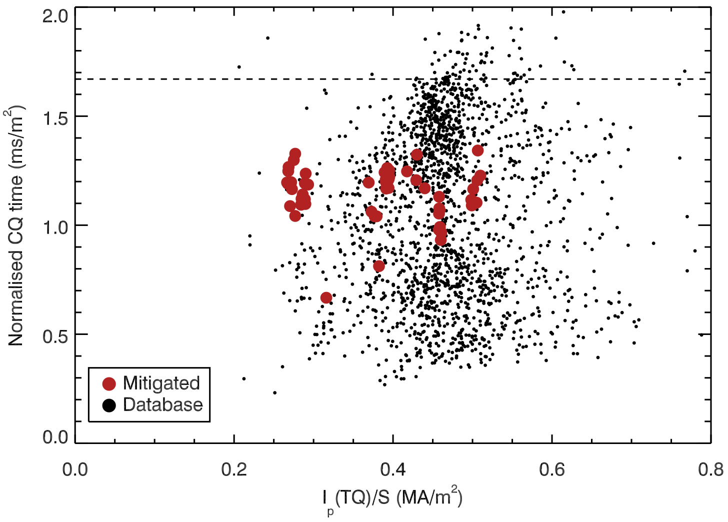

Figure 7.17: Current quench (CQ) time normalised to the plasma area plotted as a function of plasma current density. Normalising the CQ time to the area of the plasma prior to disruption allows comparison with other machines where the cross section differs. The plot shows the CQ time for mitigated discharges (red circles) and full performance disruptions from the MAST archive (black dots) determined in chapter 4. The black dashed line represents the ITER CQ timescale limit of 1.67 ms/m^2.

A key issue for ITER is the suppression of runaway electrons (REs) which are suppressed by raising the density above the critical level set by the Rosenbluth density limit [49]. Present day injection on JET has been seen to be fifty times beneath the critical limit required on JET [68]. MGI has been seen to decrease the current quench time, and increasing injection quantity is seen to accelerate the current quench as shown in figure 7.18 and from AUG data [56]. It should be noted that the MAST data shows a weak increase in current quench rate, with the quench rate proportional to 1.36 (±1.39) times the injected quantity. The data from AUG [56] show the current quench time beginning to saturate as the injected quantity is increased. The data from MAST is consistent with the AUG data when the quantity injected is considered, for example at 1.5x10^{21} particles of injection in AUG the current quench time continues to decrease. Further studies using increased injection quantities will be required to determine if saturation occurs.

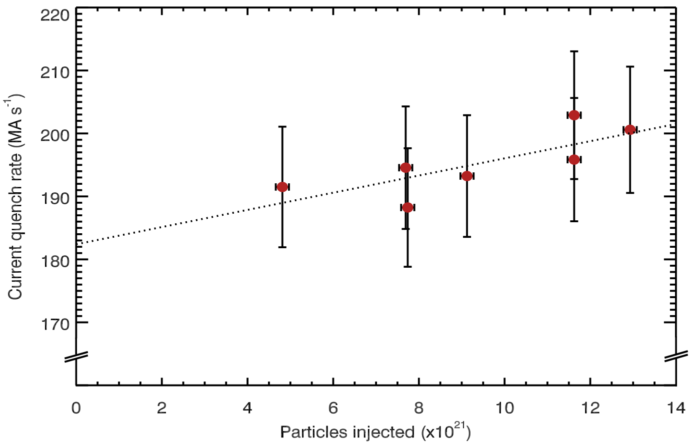

Figure 7.18: The current quench rate as a function of the number of particles injected. There is a trend of increased current quench rate for increased injection quantity. Note the suppressed y axis to highlight the dependence.

7.7.1 Halo currents

Halo currents generated during disruptions are monitored using Rogowski coils located on major vessel components, as described in chapter 3. The total halo current during the disruption can be found by summing the absolute current in each of the major components. The total halo current for a mitigated and unmitigated disruption is shown in figure 7.19. The data has been smoothed over five points to remove noise introduced by the acquisition system [131].

The halo current measurements for both the mitigated and unmitigated disruption show similar characteristics. The thermal quench prompts the loss of vertical plasma control. The plasma begins to move vertically upwards toward the upper divertor, leading to halo current production. The peak in halo current 1.5ms after the thermal quench in the unmitigated case originates from the vertical control system reaching the maximum current to the poloidal field coils. The vertical motion of the plasma increases in speed once the vertical control is lost, producing the rapid increase in halo current two milliseconds after the thermal quench in the unmitigated case and 2.5ms in the mitigated case.

Mitigation produces a significant reduction in halo current magnitude and duration, with the peak halo current falling from 160kA to 90kA and a reduction in halo current duration of between 1 and 1.5 milliseconds. The limit of the vertical control system is reached later in the mitigated case, at which point the plasma current has fallen to 0.6 MA compared to 0.9 MA in the unmitigated case, lowering the halo current size. The halo current flows along the field lines, as a result the halo

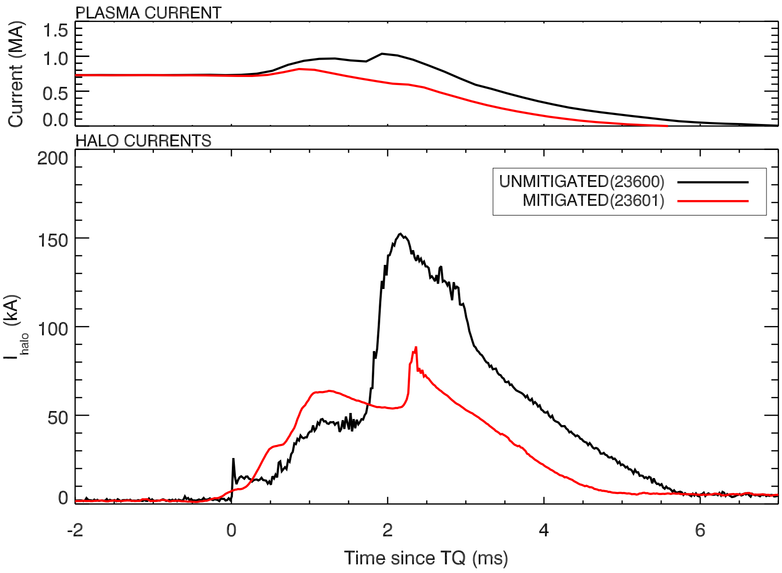

Figure 7.19: Total absolute magnitude of halo currents in all monitored components during an unmitigated disruption (black) and a mitigated disruption (red). There is a clear reduction in the duration and magnitude of the halo current as a result of mitigation

current has a component in the poloidal and toroidal direction [47]. The toroidal component generates the increase in the plasma current during the current quench at a time consistent with the peak halo current, as observed in DIII-D [40].

The halo current in each of the monitored components for each discharge are shown in figure 7.20 and 7.21. Figure 7.20 shows that the halo currents flow in the upper divertor, upper P2 coil and upper P3 coil. It has been previously shown that the sum of current sinks from the plasma and sources into the plasma are in balance [132] when all current paths are considered. For discharges 23600 and 23601 the centre column halo current detectors are unavailable, therefore preventing this balance from being calculated.

The mitigated discharge (figure 7.21) shows similar characteristics to the unmitigated case in terms of current direction. However, the upper and lower divertor (DIVU and DIVL) are equal up to the VDE. The positive halo currents suggest that the flow is towards the top of the vessel in each case. The currents could be generated via induction, the flattop region matches the region in which there is a constant gradient in the plasma current. However, the currents could be also be generated by current flow from the plasma via the upper divertor, returning via the lower divertor.

Halo current asymmetries

The asymmetries in halo currents can be measured using the toroidal peaking factor (TPF). The TPF uses toroidally displaced measurements of the halo currents flowing in a particular component to provide an estimate of the asymmetry. The TPF is

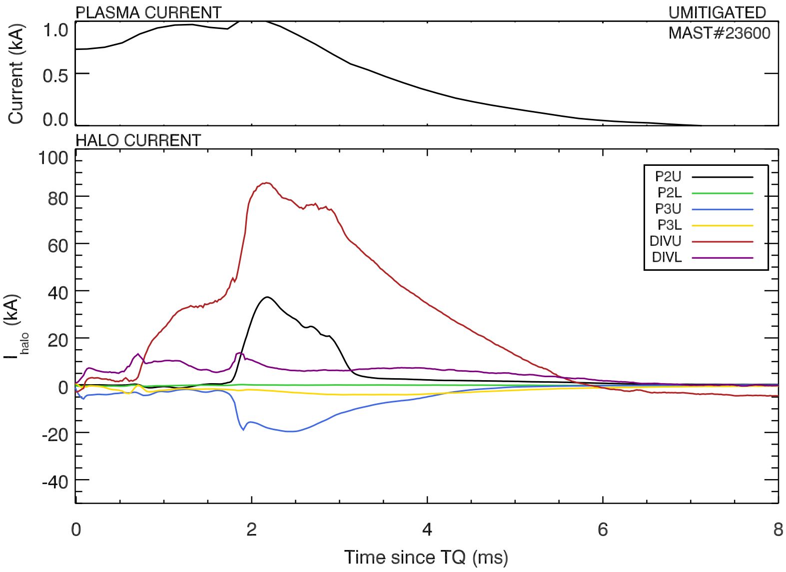

Figure 7.20: Halo currents in each of the monitored components in an unmitigated MAST discharge (23600). The legend refers to the coil in which the current is detected, P coils are poloidal field coils and DIV are the divertor surfaces. The upper and lower coils are denoted by the U and the L.

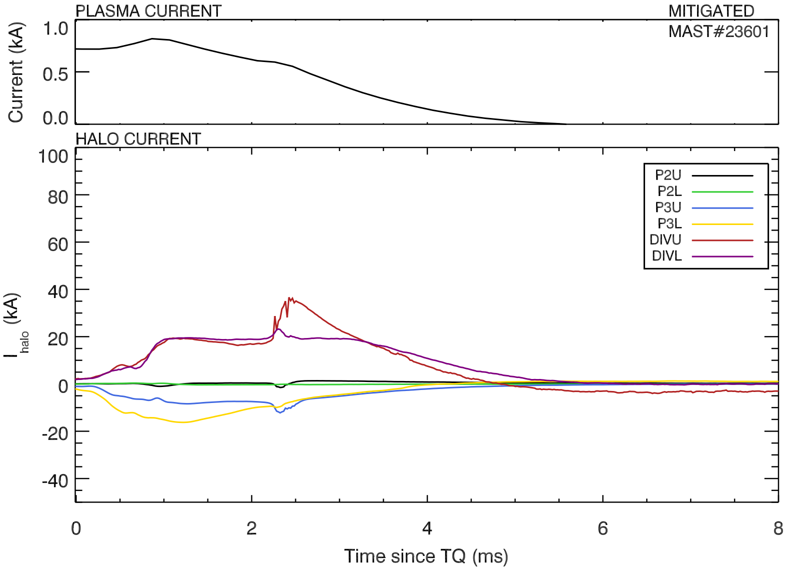

Figure 7.21: Halo currents in each of the monitored components in a mitigated MAST discharge (23601). The legend refers to the coil in which the current is detected, P coils are poloidal field coils and DIV are the divertor surfaces. The upper and lower coils are denoted by U and the L.

defined as shown in equation 7.11 as used in [132], where I_{halo} is the halo current in a given coil at time t, the sum is over the n coils on the given component.

$$\mathrm{TPF} = 1 + \frac{\max\left[I_{halo} - \frac{1}{n}\sum\limits_{i=1}^{i=n} I^{i}_{halo}\right]}{\frac{1}{n}\sum\limits_{i=0}^{i=n} I^{i}_{halo}} \tag{7.11}$$

The magnitude of the halo currents can be expressed using f_{halo} which is the maximum halo current in any component divided by the plasma current. The plasma current at the onset of the thermal quench is used in unmitigated discharges and the plasma current at the DMV trigger is used in mitigated discharges.

The interaction of halo currents with the toroidal magnetic field generate forces on the vacuum vessel. The effect of asymmetries in the halo current is to cause the halo forces generated to vary in the toroidal direction. The variation of the forces lead to shear stresses on the vacuum vessel. The important factor when considering halo current asymmetries is the product of the TPF and the size of the halo current, which is expressed as a fraction of the plasma current, f_{halo} [23, 132]. Analysis of halo forces during disruptions on several devices provides the design limit for ITER of TPF*$f_{halo} = 0.7$.

Figure 7.22 shows the TPF and f_{halo} values for discharges which disruption at full performance (black dots) and those which are are mitigated (red circles). The majority of points lie within the TPF*f_{halo} limit, with 8% of full performance disruptions lying on or outside this limit. The mean TPF*f_{halo} for the full performance discharges is 0.44(±0.19).

The unmitigated reference discharges have a mean TPF*f_{halo} of 0.51(±0.18), compared to the mitigated discharge average of 0.12(±0.09). The largest reduction in TPF*f_{halo} is seen during the H mode mitigation, where the product falls from values of the order 0.6 to 0.06. The overall, mitigated discharges exhibit lower halo fractions with similar asymmetry similar to full performance disruptions. Referring to the H mode comparison, the fall in halo current fraction in these discharges is of the order 80%, compared to a fall in TPF value of approximately 45-50%.

The decreases seen in the TPF and halo fraction have also been seen in DIII-D where a 50% reduction is seen in both the TPF and the halo fraction [40] and a four fold decrease in TPF*f_{halo}, both consistent with MAST data.

7.7.2 Runaway electrons

The presence of runaway electrons (REs) during a disruption is typically indicated by a plateau or deviation from exponential decay in the plasma current during the current quench. The plateau is then followed by hard X ray and neutron production from the interaction with material surfaces [50]. Analysis of the time delay between the thermal quench and the plasma current decaying has shown that RE plateau are

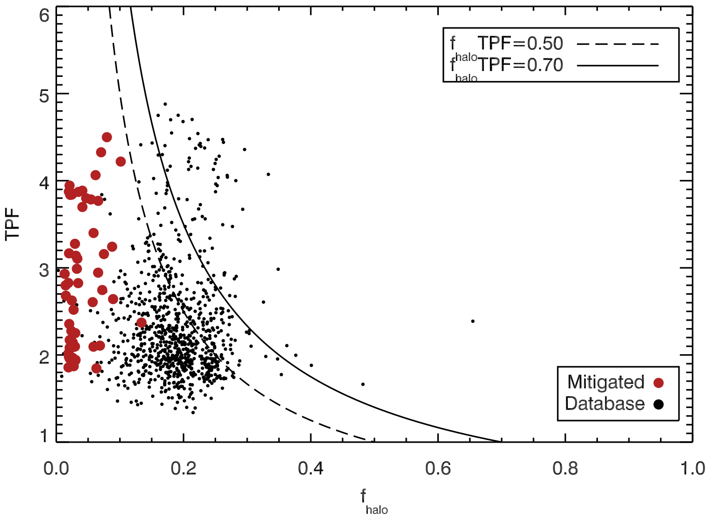

Figure 7.22: The fraction of the plasma current converted into halo current, f_{halo} can be plotted against the toroidal peaking factor (TPF) to assess the effect of toroidal halo current asymmetry. The plot shows mitigated discharges (red circles) and full performance disruptions from the MAST archive (black dots) determined in chapter 4. The solid line represents the maximum product of f_{halo} and TPF permitted in ITER which is 0.7. The dashed line corresponds to $f_{halo} * \text{TPF} = 0.5$.

not seen on MAST. It is also the case that there are no RE seen during mitigated discharges. The deviation in exponential decay seen in certain discharges (figure 7.23) is thought to be associated with the toroidal halo current generated during the VDE.

It can be seen from figure 7.23 that the deviation in the plasma current is reduced, and eliminated with increased injected quantity. This behaviour could suggest that the deviation is the start of RE formation which is then terminated by the vertical motion of the plasma. However, the RE should be detectable via the production of X rays and neutrons via the interaction with material surfaces. MAST is equipped with hard X ray cameras with limited coverage and a neutron detector, neither of which show any evidence for REs, therefore the cause of the deviation is the vertical displacement event.

In recent experiments [68, 109, 110] RE production has been seen using high Z mitigation gases, with no RE production for light Z or mixtures. Results have shown that the formation of RE is linked to the toroidal magnetic field [59, 133] where is is observed that the formation of RE occurs only when $B_t > 2.0$T both during unmitigated disruptions [133] and mitigated disruptions [67]. It is suggested [134] that this limit is generated by the excitation of whistler waves by the runaway electrons. These waves are unstable at low toroidal field and act to destabilise the runaway electrons preventing the formation of a beam. The absence of RE on MAST is likely due to the low toroidal field present (0.5T) combined with the lack of vertical stability. Although, investigations could be performed using pure argon

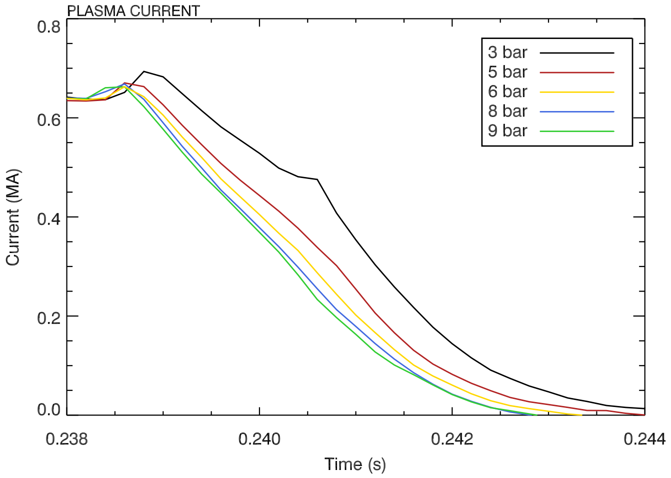

Figure 7.23: The effect of increased injection quantity on the plasma current decay. The legend shows the pressure prior to injection in the injection plenum of the valve. To convert the figure to an approximate number of particles, multiply by 1.6x10^{21}. The presence of a deviation from exponential decay in the case of 3 bar injection is likely caused by the vertical displacement event rather than RE production.

mitigation to ensure RE are still absent.

7.8 Summary

Massive gas injection is an effective means of decreasing disruption heat loads and halo currents. Mitigation reduces the divertor energy load to 40% of the total stored plasma energy in both L mode and H mode discharges. The radiated energy load increases from 10% to 40% for mitigated disruptions, showing that the main source of energy loss from the plasma is impurity radiation. Further work is required to optimise the injected mixture to increase the radiated fraction. The heat flux to the divertor shows minimal toroidal asymmetry, and appears unaffected by increased injection quantity.

Mitigation decreases the halo currents during disruptions by up to 80% over unmitigated discharges. The reduction in the halo current is likely caused by the increased speed of the current quench minimising the plasma/wall contact. The resulting TPF*F_{halo} product is well within the ITER design limit, despite the modest increase in TPF during mitigation.

Chapter 8

Conclusion

Disruptions pose a significant challenge to future devices due to the large transient heat loads and vessel forces that they generate. The key to ameliorating disruptions in ITER and DEMO is to develop an understanding of the physics and timescales in present machines.

Disruption analysis performed on previous MAST discharges has illustrated that the operational space of MAST is constrained by the three major limits in tokamaks. The density limit is seen to be raised above the Greenwald limit, likely due to the application of additional heating power. The low q limit on MAST appears to be lower than the $1/q_a = 0.5$ seen on other tokamaks. MAST exhibits a beta limit which is consistent with the scaling based on the internal inductance and plasma current, with discharges disrupting when $\beta_T \approx 4L_i I_p/aB_{phi}$.

The production of a disruption database using high performance discharges has permitted the analysis of several disruption characteristics. The thermal quench timescale has been seen to be consistent with the ITER scaling which is based on conventional aspect ratio devices. The agreement between conventional and ST devices allows the present ITER scaling to be used for the design of a component test facility (CTF) based on the ST concept.

The pre thermal quench energy loss has been seen to amount to 50% of the total stored plasma energy. The assumption in the ITER design is that there is no energy loss prior to the thermal quench. Observations of ASDEX and JET show reductions in stored energy prior to the thermal quench of between 50 and 80%, supporting the MAST data. The implication of this is that the projected disruption heat loads on ITER could be lower than currently thought, by between 50 and 80%.

The energy flow during unmitigated disruptions can be followed using bolometry and infra red thermography. MAST is unique in the coverage of all four divertor strike points, which allows accurate accounting of energy deposited onto the divertor. The energy balance between energy stored in the plasma prior to disruption (as derived from EFIT) and the total energy radiated and transported to the divertor is 91(±6)%, based on the assumption of toroidally symmetric power load to the divertor. The energy lost from the plasma is mainly delivered to the divertor, with 82% of the total energy arriving at the target compared to 8% exhausted via radiation. The majority of the energy is delivered to the divertor due to the open design of MAST and the absence of a close fitting wall upon which energy can be deposited.

Current quench times on MAST are below the ITER lower limit of 1.67 ms/m^2, being between 0.5 and 1.5 ms/m^2, consistent with NSTX results [100]. The current quench time has been increased in speed since modifications made in April 2004. The suggested cause of the increase in speed is a decrease in the impurity level in the plasma or increased temperatures as a result of the installation of a new low Z divertor.

Massive gas injection is a method of mitigating disruptions by generating a radiative collapse of the plasma. The installation of a disruption mitigation system and subsequent experiments, a first on an ST, have proved highly successful. High speed imaging of the plasma during mitigation has allowed the penetration of impurities to be monitored. The images show that the neutral impurities are confined to the plasma edge and entrained along the field lines by the ion flow. There is limited mixing of the neutral impurities with the bulk plasma during the thermal quench phase. Impurity ions, by contrast, show penetration to the q=2 surface prior to the thermal quench, with significant mixing with the bulk plasma during the thermal quench phase. The evolution of the density profiles using Thomson scattering (TS) supports these observations. The TS data shows density build up on rational surfaces during the edge cooling phase, after which the thermal quench follows. The role of the q=2 surface identified by others [60, 110], is confirmed with the largest density build up occurring on this surface.

The density build up phenomena shows several characteristics in common with a locked mode, for example, strike point splitting, Mirnov coil signals and localised filaments on high speed imaging. Following these observations, preliminary modelling of the density build up as a snake like phenomena has shown that build up can be produced with a sufficiently large convective velocity and decreased diffusion coefficient. However, these results are mainly phenomenological and further work would be required to make a firm conclusion.

Disruption mitigation via massive gas injection reduces the peak divertor power loads by 60% compared to an unmitigated disruption. The toroidal asymmetry of the heat flux can be studied using Langmuir probes and wide angle infra red thermography. The analysis of the data from these diagnostics show that the heat flux is toroidally symmetric over the outer upper and lower strike points. The resulting energy load on the divertor decreases to 40% of the total stored energy with the radiated energy rising to 40% of the total. These radiated energy deposited fractions occur for all discharges investigated, including L and H mode. Extrapolation of these heat loads to the worst case ITER disruption show that energy loadings would decrease from 440 MJ m^{-2} s$^{-0.5}$ to approximately 100 MJ

m^{-2} $s^{-0.5}$. Although this is a significant decrease, the load remains 60% above the melting/vapourisation threshold for carbon and tungsten. Optimisation of the injected impurity species should act to improve this situation.

The mitigation is seen to decrease normalised current quench times by 30% over unmitigated disruptions. The duration of the halo current phase is decreased in mitigated cases, with the product $f_{halo} *$ TPF decreasing from 0.44 to 0.12 due to mitigation. The reduction is brought about by a decrease in the size of the halo currents, f_{halo}, of up to 80%. The toroidal peaking factor (TPF) is seen to increase, with a range of 1.8 to 4.5 for mitigated disruptions compared to 0.3 to 3 for unmitigated disruptions. However, both the mitigated and unmitigated disruptions are within the ITER $f_{halo} *$ TPF limit of 0.7.

8.1 Future work

The work presented here forms a comprehensive study of disruption mitigation via massive gas injection on MAST. However, a number of areas require further exploration.

The first area which warrants future work is the propagation time of the injected gas into the vessel. In the present experiments, the time arrival of gas at the plasma edge is determined using first light from the plasma edge. The neutral density filters present in the cameras prevent the arrival from being determined accurately. Future studies should involve the imaging of the mitigation without the neutral density filters to determine the propagation time accurately.

The characteristic of the gas pulse delivered by the DMV is also unknown. Laboratory based testing should be performed to enable accurate modelling of the DMV injection and density build up on rational surfaces. The analysis of the gas pulse can be performed by injecting into a test volume and monitoring the pressure rise. In addition, interferometry can be used to characterise the gas pulse, as used in [104].

The studies performed in this thesis have concentrated on the physics of disruption mitigation. Extrapolation of the MAST data to ITER heat fluxes shows that, although a significant reduction has been achieved, the heat flux exceeds the level required for ITER. Further studies should be performed in optimising the injected species or mixture, and the quantity of material injected. Present studies have been limited to injection of 1.4×10^{22} particles, improvements made after the experimental campaign now allow injection of up to five times this quantity. Experiments investigating the effect of increased injection quantity on heat loads and current quench time, over the larger injection range, would allow for improved machine to machine comparison and extrapolation to ITER. The fuelling efficiency can be calculated on these discharges. However, the temporal resolution of the interferometer should be increased to better diagnose the fuelling efficiency at the thermal quench.

The effect of mitigation on H mode discharges has been studied in this thesis and is seen to be similar to the effect in L mode. However, further H mode studies should be performed. Specifically, studies should be performed where resonant magnetic perturbations (RMPs) are applied to mitigate ELMs [21]. The effect of RMPs is thought to be to ergodise the flux surfaces in the tokamak. The involvement of the q=2 surface suggests that disruption mitigation is dependent on the magnetic geometry of the plasma, and as such should be affected by the application of RMPs.

Finally, MAST is equipped with a motional stark effect (MSE) diagnostic which can be used to determine the q profile and current density of the plasma. Charge exchange spectroscopy (CXRS) can also be used to determine the rotation profile of the plasma. The MSE and CXRS diagnostics require the application of neutral beam heating to operate. Investigations should be performed into extending beam operation into the mitigation sequence. The availability of the current profile and rotation could shed light on the physical process at work during the mitigation sequence.

Appendix A

Convection diffusion model

The solution to the convection diffusion model used in this thesis can be found using a finite difference method as first detailed in [116]. Following the approach presented in [116], the inital conditions are used to solve the time independent convective diffusion equation to determine the diffusion profile in the plasma.

A.1 Time independent solution

Assuming time independence, the convective diffusion equation simplifies to that shown in equation A.3. Taking the coordinate system to be one dimensional and cartesian, the equation to be solved is that shown in A.4.

$$\nabla \cdot \Gamma = S \tag{A.1}$$

$$\Gamma = -D \nabla n_e + V n_e \tag{A.2}$$

$$\nabla \cdot (D \nabla n_e) - \nabla \cdot (V n_e) + S = 0 \tag{A.3}$$

$$\frac{d}{dx}\left(D\frac{n_e}{dx}\right) - \frac{d}{dx}\left(V n_e\right) + S = 0 \tag{A.4}$$

To obtain a solution for the diffusion coefficient from equation A.4 the equation is integrated and then solved using the forward difference method [135] on a grid which is shown in figure A.1. The resulting equation A.5 can be iterated to find the diffusion profile as a function of radius. The initial boundary condition used is $D_{\frac{1}{2}} = 0.4$, as used in [116]. The density profile, convective velocity term and source term are as described in section 6.6.

$$D_{i+\frac{1}{2}} = D_{i-\frac{1}{2}}\left(\frac{n_{e_i} - n_{e_{i-1}}}{n_{e_{i+1}} - n_{e_i}}\right) + \left(\frac{\Delta x \left(V_{i+\frac{1}{2}} n_{e_{i+\frac{1}{2}}} - V_{i-\frac{1}{2}} n_{e_{i-\frac{1}{2}}}\right)}{n_{e_{i+1}} - n_{e_i}}\right) + \left(\frac{S_i \left(\Delta x\right)^2}{n_{e_{i+1}} - n_{e_i}}\right) \tag{A.5}$$

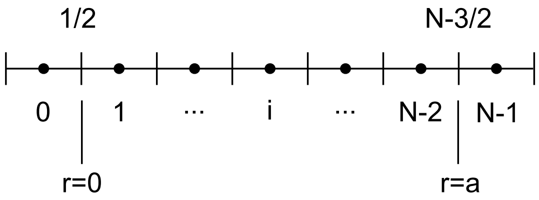

Figure A.1: Grid for convective diffusion model. The boundary conditions are used at r=0 and r=0. The cell boundaries are located is a half integer and the cell centre is where i is an integer.

Once the steady state diffusion profile is found, then the diffusion and convective velocity profiles can be modified as set out in section 6.6. The time dependence of the electron density can then be found as set out in section A.2

A.2 Time dependent solution

The time dependent equation A.6 is solved using the same finite difference techniques as used for the time independent equation. A forward difference explicit scheme is used [135] as density does not approach a steady state.

$$\frac{\partial n_e}{\partial dt} - \nabla \cdot (D \nabla n_e) + \nabla \cdot (V n_e) = S \tag{A.6}$$

Applying the finite difference method to equation A.6 produces equation A.7, where the superscript indicates time.

$$\begin{aligned} \frac{n^j_{e_i} - n^{j-1}_{e_i}}{\Delta t} &= D_{i+\frac{1}{2}} \left(\frac{n^j_{e_{i+1}} - n^j_{e_i}}{\Delta x} \right) - D_{i-\frac{1}{2}} \left(\frac{n^j_{e_i} - n^j_{e_{i-1}}}{\Delta x} \right) \\ &+ \left(V_{i+\frac{1}{2}} n^j_{e_{i+\frac{1}{2}}} - V_{i-\frac{1}{2}} n_{e^j_{i-\frac{1}{2}}} \right) + S^j_i \Delta x \end{aligned} \tag{A.7}$$

Rearrangement and substitution yields equation A.8 which allows the evolution of the j-1$^{\mathrm{th}}$ time to the j$^{\mathrm{th}}$. The time dependence is included in the constant term (γ in equation A.8, where the source evolves in time and the electron density from the previous time slice is included.

$$\alpha n^j_{e_{i-1}} + n^j_{e_i} + \beta n^j_{ei+1} = \gamma \tag{A.8}$$

Where the coefficients, α, β and γ are defined as follows;

$$\alpha = \frac{-\frac{1}{\Delta x}\left(\frac{\Delta t}{\Delta x} D_{i-\frac{1}{2}} + \frac{\Delta t}{2} V_{i-\frac{1}{2}} \right)}{1 + \frac{\Delta t}{(\Delta x)^2} D_{i+\frac{1}{2}} + \frac{\Delta t}{(\Delta x)^2} D_{i-\frac{1}{2}} + \frac{\Delta t}{2\Delta x} V_{i+\frac{1}{2}} - \frac{\Delta t}{2\Delta x} V_{i-\frac{1}{2}}} \tag{A.9}$$

$$\beta = \frac{-\frac{1}{\Delta x}\left(\frac{\Delta t}{\Delta x} D_{i+\frac{1}{2}} - \frac{\Delta t}{2} V_{i+\frac{1}{2}} \right)}{1 + \frac{\Delta t}{(\Delta x)^2} D_{i+\frac{1}{2}} + \frac{\Delta t}{(\Delta x)^2} D_{i-\frac{1}{2}} + \frac{\Delta t}{2\Delta x} V_{i+\frac{1}{2}} - \frac{\Delta t}{2\Delta x} V_{i-\frac{1}{2}}} \tag{A.10}$$

$$\gamma = \frac{\Delta t S_i^j + n_{e_i}^{j-1}}{1 + \frac{\Delta t}{(\Delta x)^2} D_{i+\frac{1}{2}} + \frac{\Delta t}{(\Delta x)^2} D_{i-\frac{1}{2}} + \frac{\Delta t}{2\Delta x} V_{i+\frac{1}{2}} - \frac{\Delta t}{2\Delta x} V_{i-\frac{1}{2}}} \tag{A.11}$$

The equation A.8 represents an array of linear equations which form a tridiagonal matrix. The matrix can be solved using the tridiagonal matrix alogrithm to produce the density profile at a given time [136].

The boundary conditions are applied the the N-1 element of the matrix, where the edge density is set to 1x10^{17} m^{-3}.

Bibliography

[1] K. Krane, *Introductory Nuclear Physics.* Wiley, 1988.

[2] "Image courtesy EFDA-JET."

[3] C. M. Braams and P. E. Stott, *Half a Century of Magnetic Confinement Fusion Research.* Institute of Physics, 2002.

[4] F. Chen, *Introduction to Plasma Physics and Controlled Fusion: Volume 1*, 2nd ed. New York: Plenum Press, 1984.

[5] K. Miyamoto, *Controlled Fusion and Plasma Physics.* London: Taylor and Francis, 2007.

[6] J. Wesson, *Tokamaks.* Oxford: Oxford University Press, 2004.

[7] W. Stacey, *Fusion Plasma Physics.* Wiley-VCH, 2005.

[8] J. P. Freidberg, *Plasma Physics and Fusion Energy.* Cambridge Unicversity Press, 2007.

[9] P. C. Stangeby, *The Plasma Boundary of Magnetic Fusion Devices*, P. Stott and H. Wilhelmsson, Eds. Taylor and Francis, 2000.

[10] C. Pitcher and P. Stangeby, "Experimental divertor physics," *Plasma Phys. and Control. Fusion*, vol. 39, pp. 779–930, 1997.

[11] F. Wagner *et al.*, "Regime of improved confinement and high beta in neutral-beam-heated divertor discharges of the ASDEX tokamak," *Phys. Rev. Lett.*, vol. 49, no. 19, pp. 1408–1412, Nov 1982.

[12] A. Sykes, M. Turner, and S. Patel, "Beta limits in tokamaks due to high-n ballooning modes," *Proc. 11th European Conference on Controlled Fusion and Plasma Physics, Aachen*, vol. II, p. 363, 1983.

[13] F. Troyon *et al.*, "MHD limits to plasma confinement," *Plasma Phys. and Control. Fusion*, vol. 26, no. 1, pp. 209–215, 1984.

[14] V. Gusev, F. Alladio, and A. Morris, "The basis of spherical tokamaks and progress in European research," *Plasma Phys. and Control. Fusion*, vol. 45, pp. A59–A82, 2003.

[15] Y.-K. Peng and D. Strickler, "Features of spherical torus plasmas," *Nuclear Fusion*, vol. 26, pp. 769–777, 1986.

[16] Y.-K. Peng, "The physics of the spherical torus," *Physics of Plasmas*, vol. 7, pp. 1681–1692, 2000.

[17] A. Sykes *et al.*, "The spherical tokamak programme at Culham," *Nuclear Fusion*, vol. 39, pp. 1271–1282, 1999.

[18] M. Shimada *et al.*, "Progress in the ITER Physics Basis: Chapter 1 - overview and summary," *Nuclear Fusion*, vol. 47, pp. S1–S17, 2007.

[19] H. Zohm, "Edge localised modes (ELMs)," *Plasma Phys. and Control. Fusion*, vol. 38, pp. 105–128, 1996.

[20] T. E. Evans *et al.*, "Suppression of large edge-localized modes in high-confinement DIII-D plasmas with a stochastic magnetic boundary," *Phys. Rev. Lett.*, vol. 92, p. 235003, 2004.

[21] T. Evans *et al.*, "Edge stability and transport control with RMP in collisionless tokamak plasmas," *Nature Physics*, vol. 2, pp. 419–423, 2006.

[22] P. L. Taylor *et al.*, "Disruption mitigation studies in DIII-D," *Physics Of Plasmas*, vol. 6, no. 5, pp. 1872–1879, 1999.

[23] T. Hender *et al.*, "Progress on the ITER Physics Basis: Chapter 3," *Nuclear Fusion*, vol. 47, pp. S128–S202, 2007.

[24] G. Matthews *et al.*, "Steady-state and transient power handling in JET," *Nucl. Fusion*, vol. 43, pp. 999–1005, 2003.

[25] D. J. Griffiths, *Introduction to Electrodynamics.* Pearson, 2008.

[26] M. Greenwald *et al.*, "A new look at density limits in tokamaks," *Nuclear Fusion*, vol. 28, pp. 2199–2207, 1988.

[27] F. Troyon *et al.*, "Beta limits in tokamaks," *Plasma Phys. and Control. Fusion*, vol. 30, p. 1597, 1988.

[28] M. Murakami, J. Callen, and L. Berry, "Some observations on the maximum densities in tokamak experiments," *Nuclear Fusion*, vol. 16, p. 347, 1976.

[29] M. Greenwald, "Density limits in toroidal plasmas," *Plasma Phys. and Control. Fusion*, vol. 44, pp. R27–R80, 2002.

[30] J. Wesson *et al.*, "Disruptions in JET," *Nuclear Fusion*, vol. 29, pp. 641–666, 1989.

[31] F. C. Schuller, "Disruptions in tokamaks," *Plasma Phys. and Control. Fusion*, vol. 37, pp. A135–A162, 1995.

[32] S. Mirnov *et al.*, “Chapter 3: MHD stability, operational limits and disruptions,” *Nuclear Fusion*, vol. 39, pp. 2251–2389, 1999.

[33] A. Bondeson *et al.*, “MHD modelling of density limit disruptions in tokamaks,” *Nuclear Fusion*, vol. 31, pp. 1695–1716, 1991.

[34] T. Hender *et al.*, “Magnetohydrodynamic limits in spherical tokamaks,” *Physics Of Plasmas*, vol. 6, pp. 1958–1968, 1999.

[35] H. Zohm *et al.*, “MHD stability and disruption physics in ASDEX-Upgrade,” *Plasma Phys. and Control. Fusion*, vol. 37, pp. A313–A324, 1995.

[36] S. Mirnov *et al.*, “Phenomenology of major and minor disruptions in high beta deuterium and tritium tokamak fusion test reactor plasma,” *Physics Of Plasmas*, vol. 5, pp. 3950–3960, 1998.

[37] R. Kleva and P. Guzdar, “Fast disruptions by ballooning mode ridges and fingers in high temperature, low resistivity toroidal plasmas,” *Physics Of Plasmas*, vol. 8, pp. 103–109, 2001.

[38] S. E. Kruger, “Dynamics of the major disruption of a DIII-D plasma,” *Physics of Plasmas*, vol. 12, p. 056113, 2005.

[39] G. Pautasso *et al.*, “Details of the power deposition in the thermal quench of ASDEX-Upgrade disruptions,” in *31st EPS Conference, London. P-4.132*, 2004.

[40] D. G. Whyte *et al.*, “Disruption mitigation with high-pressure noble gas injection,” *Journal Of Nuclear Materials*, vol. 313-316, pp. 1239–1246, 2003.

[41] E. M. Hollmann *et al.*, “Measurements of impurity and heat dynamics during noble gas jet-initiated fast plasma shutdown for disruption mitigation in DIII-D,” *Nuclear Fusion*, vol. 45, pp. 1046–1055, 2005.

[42] A. Herrmann, “Overview on stationary and transient divertor heat loads,” *Nuclear Fusion*, vol. 44, pp. 883–903, 2002.

[43] E. Delchambre *et al.*, “Power load during disruptions in MAST,” *Journal of Nuclear Materials*, vol. 363-365, pp. 1409–1413, 2007.

[44] G. Arnoux *et al.*, “Heat loads on plasma facing componets during disruptions on JET,” *Nuclear Fusion*, vol. 49, p. 085038, 2009.

[45] A. Hassanein and I. Konkashbaev, “An assessment of disruption erosion in the ITER environment,” *Fusion Engineering and Design*, vol. 28, pp. 27–33, 1995.

[46] Y. Nakamura *et al.*, “Mechanism of vertical displacement events in JT-60U disruptive discharges,” *Nucl. Fusion*, vol. 36, pp. 643–656, 1996.

[47] D. Humphreys and A. Kellmann, "Analytic modelling of axisymmetric disruption halo currents," *Physics of Plasmas*, vol. 6, pp. 2742–2756, 1999.

[48] P. Helander, L.-G. Eriksson, and F. Andersson, "Runaway acceleration during magnetic reconnection in tokamaks," *Plasma Phys. and Control. Fusion*, vol. 44, pp. B247–B262, 2002.

[49] M. Rosenbluth and S. Putvinski, "Theory for avalanche of runaway electrons in tokamaks," *Nuclear Fusion*, vol. 37, pp. 1355–1362, 1997.

[50] R. Gill *et al.*, "Behaviour of disruption generated runaways in JET," *Nuclear Fusion*, vol. 42, pp. 1039–1044, 2002.

[51] R. Yoshino *et al.*, "Fast plasma shutdown by killer pellet injection in JT-60U with reduced heat flux on the divertor plate and avoiding runaway electron generation," *Plasma Phys. and Control. Fusion*, vol. 39, pp. 313–332, 1997.

[52] D. Whyte *et al.*, "Energy balance, radiation and stability during rapid plasma termination via impurity pellet injections in DIII-D," in *24th European Conf. on Contr. Fusion and Plasma Physics, Berchtesgaden, Germany, Vol. 21A, Part III, p1137*, 1997.

[53] S. Bozhenkov *et al.*, "Main characteristics of the fast disruption mitigation valve," *Rev. Sci. Inst*, vol. 78, p. 033503, 2007.

[54] D. Whyte *et al.*, "Mitigation of tokamak disruptions using high pressure gas injection," *Phys. Rev. Lett.*, vol. 89, p. 055001, 2002.

[55] D. G. Whyte *et al.*, "Disruption mitigation on Alcator C-Mod using high-pressure gas injection: Experiments and modelling toward ITER," *Journal Of Nuclear Materials*, vol. 363, pp. 1160–1167, 2007.

[56] G. Pautasso *et al.*, "Disruption studies in ASDEX Upgrade in view of ITER," *Nuclear Fusion*, vol. 51, p. 124056, 2009.

[57] U. Kruezi *et al.*, "Massive gas injection experiments at JET: Performance and characterisation of the disruption mitigation valve," in *36th EPS conference on Plasma Physics, Sofia, Bulgaria*, 2009.

[58] R. Granetz *et al.*, "Gas jet disruption mitigation studies on Alcator C-Mod and DIII-D," *Nuclear Fusion*, vol. 47, pp. 1086–1091, 2007.

[59] G. Pautasso *et al.*, "Plasma shut-down with fast impurity puff on ASDEX upgrade," *Nuclear Fusion*, vol. 47, no. 8, pp. 900–913, 2007.

[60] E. M. Hollmann *et al.*, "Observation of q-profile dependence in noble gas injection radiative shutdown times in DIII-D," *Physics Of Plasmas*, vol. 14, no. 1, p. 012502, 2007.

[61] M. Lehnen *et al.*, “Runaway generation during disruptions in JET and TEXTOR,” *Journal Of Nuclear Materials*, vol. 390-391, pp. 740–746, 2009.

[62] E. Hollmann *et al.*, “Measurements of injected impurity assimilation during massive gas injection experiements in DIII-D,” *Nuclear Fusion*, vol. 48, p. 115007, 2008.

[63] V. Rozhansky *et al.*, “Penetration of supersonic gas jets into a tokamak,” *Nuclear Fusion*, vol. 46, pp. 367–382, 2006.

[64] D. Morozov *et al.*, “Mechanisms of disruptions caused by noble gas injection into tokamak plasmas,” *Nuclear Fusion*, vol. 45, pp. 882–887, 2005.

[65] V. Izzo, “A numerical investigation of the effects of impurity penetration depth on disruption mitigation by massive high-pressure gas jet,” *Nuclear Fusion*, vol. 46, pp. 541–547, 2006.

[66] V. A. Izzo *et al.*, “Magnetohydrodynamic simulations of massive gas injection into Alcator C-Mod and DIII-D plasmas,” *Physics Of Plasmas*, vol. 15, p. 056109, 2008.

[67] M. Lehnen *et al.*, “First experiments on massive gas injection at JET - Consequences for disruption mitigation on JET and ITER,” in *36th EPS Conference on Plasma Physics, Sofia, Bulgaria, Vol 33E, O-2.001*, 2009.

[68] M. Lehnen, “Massive gas injection experiments at JET,” in *IEA Workshop W70 on Key ITER Disruption Issues, Culham*, 2009.

[69] M. Sugihara, “Key ITER Issues in Disruptions and their Mitiation,” in *IEA Workshop W70 on Key ITER Disruption Issues, Culham*, 2009.

[70] S. Maruyama *et al.*, “Fuelling and disruption mitigation in ITER,” in *SOFE 2009. 23rd IEEE/NPSS Symposium on Fusion engineering*, 2009.

[71] M. Reinke *et al.*, “Toroidally resolved radiation dynamics during a gas jet mitigated disruption on Alcator C-Mod,” *Nuclear Fusion*, vol. 48, p. 125004, 2008.

[72] G. Pautasso, “Disruption mitigation in AUG and implications for ITER,” in *IEA Workshop W70 on Key ITER Disruption Issues, Culham*, 2009.

[73] R. Yoshino and S. Tokuda, “Runaway electrons in magnetic turbulence and runaway current termination in tokamak discharges,” *Nuclear Fusion*, vol. 40, pp. 1293–1309, 2000.

[74] L. Baylor *et al.*, “Disruption mitigation technology concepts and implications for ITER,” *IEEE Transactions on Plasma Science*, vol. 38, pp. 419–424, 2010.

[75] D. Whyte *et al.*, "Studies of requirements for ITER disruption mitigation systems," in *22nd IAEA Fusion Energy Conference, Geneva, IT/P6-18*, 2008.

[76] M. Sugihara *et al.*, "Disruption and runaway electron mitigation in ITER," in *36th EPS Conference on Plasma Physics, Sofia, Bulgaria. Vol 33E, P-4.165*, 2009.

[77] A. Darke *et al.*, "MAST: a Mega Amp Spherical Tokamak," in *Proc. 18th Symp. on Fusion Technology (Karlsruhe,Germany), vol 1, pg 799-802*, 1994.

[78] H. Meyer *et al.*, "Overview of physics results from MAST," *Nuclear Fusion*, vol. 49, p. 104017, 2009.

[79] A. Darke *et al.*, "The MAST improved divertor," *Fusion Engineering and Design*, vol. 75-79, pp. 285–289, 2005.

[80] I. H. Hutchinson, *Principles of Plasma Diagnostics.* Cambridge University Press, 2004.

[81] N. J. Peacock *et al.*, "Measurements of the electron temperature by Thomson scattering in tokamak T3," *Nature*, vol. 224, pp. 488–490, 1969.

[82] A. W. DeSilva, "The evolution of light scattering as a plasma diagnostic," *Contrib. Plasma Phys.*, vol. 40, pp. 23–35, 2000.

[83] R. Scannell *et al.*, "Design of a new Nd:YAG Thomson scattering system for MAST," *Rev. Sci. Inst*, vol. 79, p. 10E730, 2008.

[84] NRL, *NRL Plasma Formulary.* Navel Reasearch Laboratory, 2009.

[85] L. Garzotti, "MAST SXR arrays," private communication.

[86] A. R. Field, "MAST bolometry," private communication.

[87] G. de Temmerman, "MAST IR system," private communication.

[88] F. C. Lott, "Thermographic power accounting on MAST," Ph.D. dissertation, Imperial College London, 2006.

[89] L. Lao, H. S. J. nad R.D. Stambaugh, and W. Pfeiffer, "EFIT," *Nuclear Fusion*, vol. 25, p. 1421, 1985.

[90] B. Lloyd *et al.*, "Overview of physics results from MAST," *Nuclear Fusion*, vol. 47, no. 10, pp. S658–S667, 2007.

[91] P. de Vries *et al.*, "Statisical analysis of disruptions on JET," *Nuclear Fusion*, vol. 49, p. 055011, 2009.

[92] A. Sykes, "First results from MAST," in *IAEA FEC OV4-1*, 2000.

[93] G. Federici, “Plasma wall interactions in ITER,” *Physica Scripta*, vol. T124, pp. 1–8, 2006.

[94] V. Mukhovatov *et al.*, “ITER Physics Basis: Chapter 9 - ITER contributions for DEMO plasma development,” *Nuclear Fusion*, vol. 47, pp. S404–S413, 2007.

[95] V. Riccardo *et al.*, “Timescale and magnitude of plasma thermal energy loss before and during disruptions on JET,” *Nuclear Fusion*, vol. 45, pp. 1427–1438, 2005.

[96] A. Loarter, “Expected energy fluxes onto ITER plasma facing components during disruption thermal quenches from multi-machine data comparisons,” *20st IAEA Fusion Energy Conference*, vol. Villamoura, Portugal, pp. IT/P3–34, 2004.

[97] A. Loarte, “ELMs and disruptions in ITER,” *21st IAEA Fusion Energy Conference*, vol. Chengdu, China, pp. IT/P1–14, 2006.

[98] I. Chapman *et al.*, “Saturated ideal modes in advanced tokamak regimes in MAST,” *Nuclear Fusion*, vol. 50, p. 045007, 2010.

[99] G. F. Counsell *et al.*, “Overview of MAST results,” *Nuclear Fusion*, vol. 45, pp. S157–S167, 2005.

[100] S. P. Gerhardt *et al.*, “Characterisation of the plasma current quench during disruptions in the national spherical torus experiment,” *Nuclear Fusion*, vol. 49, p. 025005, 2009.

[101] M. Sugihara *et al.*, “Waveform of current quench during disruptions in tokamaks,” *Journal of Plasma and Fusion Research*, vol. 79, pp. 706–712, 2003.

[102] R. Granetz *et al.*, “Gas jet disruption mitigation studies on Alcator C-Mod,” *Nuclear Fusion*, vol. 46, pp. 1001–1008, 2006.

[103] A. Savtchkov, K. Finken, and G. Mank, “Development of a fast valve for mitigating disruptions in a tokamak,” *Rev. Sci. Inst*, vol. 73, pp. 3490–3493, 2002.

[104] K. Finken, M. Lehnen, and S. Bozhenkov, “Gas flow analysis of a disruption mitigation valve (DMV),” *Nuclear Fusion*, vol. 48, p. 115001, 2008.

[105] K. Jousten, “On the gas species dependence of Pirani gauges,” *Journal of Vac. Science and Tech. A*, vol. 26(3), pp. 352–359, 2008.

[106] A. J. Thornton *et al.*, “Disruption mitigation studies on the Mega Ampere Spherical Tokamak MAST,” in *Plasma Surface Interaction conference,*

San Diego. Article in Press. http://dx.doi.org/10.1016/j.jnucmat.2010.10.029, 2010.

[107] L. D. Landau and E. M. Lifshitz, *Fluid Mechanics.* Pergamon Press, 1987.

[108] A. Huber *et al.*, "Radiation loads on plasma facing components of JET during transient events," in *Proc. 19th Plasma Surface Interatactions Conference, San Diego, May 2010*, 2010.

[109] S. Bozhenkov *et al.*, "Generation and suppression of runaway electrons in disruption mitigation experiments in TEXTOR," *Plasma Phys. and Control. Fusion*, vol. 50, p. 105007, 2008.

[110] C. Reux *et al.*, "Experimental study of disruption mitigation using massive injection of noble gases on Tore Supra," *Nuclear Fusion*, vol. 50, p. 095006, 2010.

[111] R. J. Buttery *et al.*, "Effects of resonant magnetic perturbations on divertor target power loads in COMPASS-D," *Nuclear Fusion*, vol. 36, pp. 1369–1388, 1996.

[112] P. deVries *et al.*, "Temperature profile perturbations due to magnetic islands in TEXTOR," *Plasma Phys. Control. Fusion*, vol. 39, pp. 439–451, 1997.

[113] P. de Vries *et al.*, "Density profile preaking inside m/n=2/1 magnetic islands in TEXTOR-94," *Nucl. Fusion*, vol. 37, pp. 1641–1646, 1997.

[114] J. Wesson, "Snakes," *Plasma Phys. Control. Fusion*, vol. 37, pp. A337–A346, 1995.

[115] R. Gill *et al.*, "Snake-like density perturbations in JET," *Nucl. Fusion*, vol. 32, pp. 723–735, 1992.

[116] E. Arends, "Density gradients in Spherical Tokamak plasmas," Ph.D. dissertation, FOM, 2003.

[117] M. Lehnen *et al.*, "Massive gas injection experiments at JET," in *SEWG meeting on Transient Loads, Juelich, September*, 2010.

[118] S. A. Bozhenkov *et al.*, "Efficiency of massive gas injection for increase of plasma density in TEXTOR experiments on disruption mitigation," in *36th EPS Conference on Plasma Phys. Sofia, ECA Vol.33E, P-1.180*, 2009.

[119] M. Tournianski *et al.*, "Anisotropic fast neutral particle spectra in the MAST spherical tokamak," *Plasma Phys. and Control. Fusion*, vol. 47, pp. 671–684, 2005.

[120] J. I. Paley, "Energy flow during disruptions," Ph.D. dissertation, Imperial College, 2005.

[121] L. Jiji, *Heat Conduction.* Springer, 2009.

[122] A. Herrmann *et al.*, "Energy flux to ASDEX-Upgrade divertor plates determined by thermography and calorimetry," *Plasma Phys. and Control. Fusion*, vol. 37, pp. 17–29, 1995.

[123] R. Reichle *et al.*, "Concept and development of ITER divertor thermography diagnostic," *Journal Of Nuclear Materials*, vol. 390-391, pp. 1081–1085, 2009.

[124] T. Loarer *et al.*, "Surface temperature measurements by means of pulsed photothermal effect is fusion devices," *J. Nuc. Matt.*, vol. 363-365, pp. 1450–1456, 2007.

[125] A. Herrmann, "Limitations for divertor heat flux calculations of fast events in tokamaks," in *28th EPS conference on Controlled Fusion and Plasma Physics, Funcal, ECA Vol. 25A 2109-2112*, 2001.

[126] P. Andrew *et al.*, "Thermal effects of surface layers on divertor target plates," *J. Nuc. Mat.*, vol. 313-316, pp. 135–139, 2003.

[127] E. Delchambre, G. Counsell, and A. Kirk, "Effect of micrometric hot spots on surface temperature measurement and flux calculation in the middle and long infrared," *Plasma Phys. and Control. Fusion*, vol. 51, p. 055012, 2009.

[128] G. de Temmerman *et al.*, "Thermographic study of heat load asymmetries during MAST L-mode discharges," *Plasma Phys. and Control. Fusion*, vol. 52, p. 095005, 2010.

[129] R. Reichle *et al.*, "Thermography of target plates with near-infrared optical fibres at Tore Supra," *Journal Of Nuclear Materials*, vol. 290-293, pp. 701–705, 2001.

[130] E. M. Hollmann *et al.*, "Plasma surface interactions during tokamak disruptions and rapid shutdowns," in *Plasma Surface Interaction conference, San Diego. Article in Press. http://dx.doi.org/10.1016/j.jnucmat.2010.10.009*, 2010.

[131] R. Martin, "Halo current monitors," private Communication.

[132] G. Counsell *et al.*, "On the magnitude and distribution of halo currents during disruptions on MAST," *Plasma Phys. and Control. Fusion*, vol. 49, pp. 435–446, 2007.

[133] V. Riccardo and J. E. contributors, "Disruptions and disruption mitigation," *Plasma Phys. Control. Fusion*, vol. 45, pp. A269–A284, 2003.

[134] T. Fulop, H. Smith, and G. Pokol, "Magnetic field threshold for runaway generation in tokamak disruptions," *Phys. Plasmas*, vol. 16, p. 022502, 2009.

[135] H. Versteeg and W. Malalasekera, *An Introduction to Computational Fluid Dynamics.* England: Longman Scientific and Technical, 1995.

[136] K. Riley, M. Hobson, and S. Bence, *Mathematical Methods for Physics and Engineering.* Cambridge University Press, 2002.